

國立交通大學
電子物理研究所
博士論文

III 族氮化物奈米粒成長與光學特
性研究



The growth and optical studies of group
III-nitride nanodots

研究生：柯文政

指導教授：陳衛國

中華民國九十五年七月

III 族氮化物奈米粒成長與光學特性研究
The growth and optical studies of group III-nitride
nanodots

研 究 生：柯文政

Student：Wen-Cheng Ke

指 導 教 授：陳衛國

Advisor：Wei-Kuo Chen



Submitted to Institute of Electrophysics
College of Science
National Chiao Tung University
in partial Fulfillment of the Requirements
for the Degree of
Doctor of Philosophy
in
Electrophysics
July 2006
Hsinchu, Taiwan, Republic of China

中華民國九十五年七月

國立交通大學

研究所博士班

論文口試委員會審定書

本校電子物理系博士班 柯文政 君
所提論文 III 族氮化物奈米粒成長與光學特性研究

合於博士資格水準，業經本委員會評審認可。

口試委員：



周紹斌

林文仁

李明如

黃柏弘

張文豪

周凱清

指導教授：

陳衛國

系主任：

朱仲夏

教授

中華民國 95 年 7 月 17 日

**Institute of Electrophysics
National Chiao Tung University**

Taiwan, Republic of China
MM DD, YY(ex: June 30, 2004)

We have carefully read the dissertation entitled

The growth and optical studies of group III-nitride nanodots

submitted by Wen-Cheng Ke in partial fulfillment of the requirements of
the degree of **DOCTOR OF PHILOSOPHY** and recommend its acceptance.

 Wen-Jen Lin

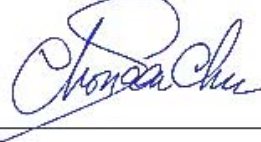
 Ming-Chih Lee  Huey-Bolun

Wen-Dao Chang Wu-chung chon

Thesis Advisor



Director of Institute of Electorphysics :



III 族氮化物奈米粒成長與光學特性研究

研究生：柯文政

指導教授：陳衛國

國立交通大學電子物理所

摘要

本論文初期我們透過微螢光激發光譜(μ -PL)分析氮化鋁鎵薄膜表面直徑約 6 μm 的 hillock 微結構光學特性。實驗結果顯示相對於 hillock 的發光譜峰為 351 nm (I_H)，而在其周圍之氮化鋁鎵薄膜發光譜峰約為 341 nm (I_{matrix})； I_H 的強度隨著量測位置由邊緣往 hillock 中心移動時其強度明顯增強，半高寬由 76 meV 降低至 53 meV，此量測結果顯示 hillock 為一種高發光強度之微結構。從變溫 μ -PL 的量測顯示 I_H 譜峰與溫度關係呈現 S 型之變化，其轉換溫度約為 120 K，此外紅位移亦較 I_{matrix} 來的小，這些結果均顯示出 hillock 相較於周圍之氮化鋁鎵薄膜而言，具有較低之鋁組成含量；另一方面，我們亦發現 hillock 之尺寸變大時(從 6 μm 增加到 11 μm)，其鋁組成約降低~2%。

本論文提出一種特別的「流量調制磊晶法」製程技術用以成長 III 族氮化物奈米粒結構。首先，我們利用此技術成功地成長 GaN 奈米粒在低晶格不匹配度之 $\text{Al}_{0.15}\text{Ga}_{0.85}\text{N}$ 緩衝層上，由奈米粒密度與成長溫度關係圖中，我們發現使用該方法成長之奈米粒在較低與較高成長溫度區間主要分別由反應物於薄膜表面之擴散機制與吸附機制主導；因為該方法在通入 TMGa 反應氣體時，是先形成 Ga 金屬，而 Ga 金屬與 $\text{Al}_{0.15}\text{Ga}_{0.85}\text{N}$ 緩衝層晶格長數分別為 4.51 與 3.18Å，晶格不匹配度高達 41.8%，故此方法成長 GaN 奈米粒應為 Volmer-Weber 成長模式。另一方面，我們進一步深入研究 GaN 奈米粒之光學特性，針對平均高度分別為 6.5, 7, 8.5 nm 之奈米粒進行變溫螢光光譜研究，在 PL 峰點能量與溫度倒數關係圖中，使用 Varshini 方程式模擬實驗資料，我們得到低溫區之侷限能量隨著奈米粒尺寸縮小而減小；此結果與使用 Arrhenius 方程式模擬 PL 積分強度與溫度倒數關係圖所獲得之低溫區活化能結果一致；而高溫區之活化能亦隨著奈米粒尺寸縮小而減小，此高溫區活化能代表著奈米粒內之載子因溫度升高躍遷至氮化鋁鎵能障層氮空缺能階所需之能量。

另一方面，我們亦成功地在 GaN 緩衝層上成長 InN 奈米粒，在覆蓋 GaN 披覆

層後進行 PL 光學分析，當 InN 奈米粒高度降低至 6.5 nm 時，其 PL 峰點能量藍位移至 1.07 eV；在溫度相依之 PL 光譜量測中，我們發現到 PL 譜峰位置與量測溫度之關係似乎不依循 Varshni 方程式之預測曲線，相較於 InN 塊材而言，其發光波長具有較高的溫度穩定性。而在 PL 積分強度與溫度倒數關係圖得知，InN 奈米粒之高溫區活化能為 73 meV 明顯高於 InN 塊材之 43 meV，顯示奈米粒之 thermal quench 程度相較於塊材而言較弱，意即 InN 奈米粒具有更佳之光學特性。最後，我們分別比較使用流率調制磊晶(FME)與 MOCVD 兩種成長方法成長之 InN 奈米粒結構與光學特性，實驗結果顯示在 FME 成長方法中，In adatom 之擴散活化能明顯低於 MOCVD 成長方法；另外我們發現到使用 FME 成長 InN 奈米粒時，在 In-rich 的條件下成長之 InN 奈米粒擁有較佳的光學特性，當 NH₃ 流率調低至 500 sccm 時，在未覆蓋 GaN 披覆層下，已可以獲得 PL 光譜半高寬達 63 meV 之 InN 奈米粒。



The growth and optical studies of group III-nitride nanodots

Student : Wen-Cheng Ke

Advisor : Wei-Kuo Chen

Institute of Electrophysics National Chiao Tung University

Abstract

In this thesis, the spatial variation of the optical properties of hillocks in $\text{Al}_{0.11}\text{Ga}_{0.89}\text{N}$ films has been studied by using microphotoluminescences (μ -PL) microscopy. The μ -PL spectrum revealed a strong emission peak (I_H) at 351 nm from the hillock, besides the near-band-edge peak emission (I_{matrix}) at 341 nm. Moreover, the I_H intensity increases significantly and its full width at half maximum (FWHM) decreases from 76 to 53 meV by probing across the hillock center. These indicated that the hillock is a strong emission structure. The temperature-dependent μ -PL measurements showed that the I_H also has the S-shape behavior with a transition temperature of ~ 120 K which is lower than that of I_{matrix} . The redshift of I_H is also smaller than I_{matrix} . Both indicated that the Al composition in hillocks is lower than the surrounding area. Moreover, we also observed that the Al composition decreased $\sim 2\%$ as the diameter of hillock increased from $6 \mu\text{m}$ to $11 \mu\text{m}$.

Otherwise, we proposed a new technique for fabrication III-nitride nanoparticles in flow rate modulation epitaxy (FME). Firstly, the self-organized GaN dot structure is successfully grown on a slightly lattice-mismatched $\text{Al}_{0.11}\text{Ga}_{0.89}\text{N}$ epilayer using FME growth technique. From the variation of dot density with growth temperature, we can observe that the GaN dot growth is controlled predominately by the surface diffusion of Ga adatoms at substrate temperatures below 915°C and by re-evaporation at higher temperatures. Because of the special alternating gas supply feature in FME, during the Ga source step, it is the Ga metal that is deposited on the underlying $\text{Al}_{0.11}\text{Ga}_{0.89}\text{N}$ layer. This is because of the large lattice mismatch of 41.8% between the Ga metal (4.51 \AA) and $\text{Al}_{0.11}\text{Ga}_{0.89}\text{N}$ (3.18 \AA). We consider that the GaN dot growth in this study is mainly through the Volmer-Weber growth mode. Moreover, the temperature dependent PL studies showed that at low temperature the localization energy, which accounts for de-trapping of excitons, decreases with the

reducing dot size. The decrease in emission efficiency at high temperature is attributed to the activation of carriers from the GaN dot to the nitrogen vacancy (V_N) state of the $Al_{0.11}Ga_{0.89}N$ barrier layer. The activation energy decreases with reducing dot size.

Secondly, the self-organized InN dots successfully grown on GaN epilayer using pulsed-growth mode growth technique. The PL properties of InN dots embedded in GaN were also investigated. We observed a systematic blueshift in the emission energy as the average dot height was reduced. The widely size-tunable emission energy can be ascribed to the size quantization effect. Temperature-dependent PL measurements show that the emission peak energies of the dots are insensitive to temperature, as compared with that of bulk film, indicating the localization of carriers in the dots. A reduced quenching of the PL from the InN dots was also observed, implying superior emission properties for the embedded InN dot structures. Finally, FME was also employed to synthesize self-assembly InN dots on GaN/sapphire substrate. Experimental results clearly indicate the adatom diffusion activation energy in FME is greatly reduced as compared to that in conventional growth method. We also demonstrate that InN dots prepared by FME under In-rich growth conditions possess much better optical quality than under N-rich growth conditions. Consequently, relatively high PL intensity with linewidth as narrow as 63 meV was realized for InN dots grown by FME at a NH_3 background flow rate of 500 sccm, without any encapsulating layer.

誌 謝 (Acknowledgements)

漫長的博士研究生涯終於劃下了句點，回首這六年的點滴，首先最要感謝的人是我的指導教授陳衛國老師，在他的諄諄教誨下，讓我學會處理事情所需要的企圖心、嚴謹態度與永不放棄的毅力；更感謝他在我面臨放棄博士學位時，適時給予我鼓勵與協助，讓我有繼續完成學業的勇氣與信心。也要感謝他在實驗研究與論文寫作上長期耐心的指導，不斷地啟發我深入發掘問題與解決問題，才使得本論文得以順利完成。

另外，也要感謝陳文雄老師、李明知老師、周武清老師及張文豪老師在每一次的博士班會議中不厭其煩地提供各種不同的意見，啟發我對問題思考的全面性。也要感謝我的啟蒙老師黃柏仁教授在碩士班期間的提攜與指導。更要感謝晶元光電公司周銘俊副總於口試時提供許多寶貴意見。亦感謝已畢業學長歐震、潘永中、徐宸科、黃懷瑩、李文雄.. 等人，由於您們的關心與協助，才能讓我順利走完博士生涯。也要感謝博士班古慶順、李寧、陳京玉、蔡儀哲、傅振邦.. 等人及所有畢業與在學的碩士班學弟妹們，有您們的幫忙與討論，所有的實驗研究才得以順利完成。

而我也要特別感謝中科院五所副組長林文仁博士，提供完善的 MOCVD 磊晶設備，在他身上我學到待人處事的包容心。也感謝小組長程一誠博士及劉書史、張國仁及李大青.. 等大哥們在院內的協助幫忙。特別要感謝藍文厚老師、姜崇義博士在我博士班期間的鼓勵與幫助。也要感謝林科均(林大哥)、林家慶對於 MOCVD 系統的維護與實驗上的協助，也感謝翁仁斌先生協助 SEM 拍攝。亦要感謝柯誌欣學長、陳文瑞學長、陳一塵與官大明在中科院內的幫忙與討論，能夠認識您們讓我在中科院的生活更加豐富。

最後，我要感謝我的父母與家人這幾年來的關懷、包容與支持，讓我可以無後顧之憂的環境下完成博士學位，特別要感謝妻子碧芳對我的鼓勵與諒解，這幾年來跟著我吃了許多苦，也要感謝已故的張榮富老師，教導我很多的生命觀念，謝謝您們大家!!

CONTENTS

Abstract (Chinese)	i
Abstract (English)	iii
Acknowledgments	v
Contents	vi
List of Tables	viii
List of Figures	ix
Chapter 1 Introduction	1
1-1 Recent Researches of III-Nitride Micro-Structure	1
1-2 Low Dimensional Structures	4
Chapter 2 Theoretical Backgrounds	11
2-1 Quantum Dots Growth Mechanisms	12
2-2 Photoluminescence (PL), Temperature Dependent of PL Spectra	16
Chapter 3 Hillocks in $\text{Al}_{0.11}\text{Ga}_{0.89}\text{N}$ Films	25
3-1 Experimental Details	26
3-2 Microstructure in AlGaN Films	27
3-3 Micro-Photoluminescence (μ -PL) Spectra of AlGaN Hillock	28
3-4 Temperature Dependent of μ -PL Spectra of AlGaN Hillock	29
3-5 Size Dependent of μ -PL Spectra of AlGaN Hillock	31
3-6 Conclusions of AlGaN Hillock	32
Chapter 4 GaN Nanodots Growth	44
4-1 Experimental Details	46
4-2 Growth Temperature Effect	49
4-3 Size Control	51
4-4 Growth Mode	52
4-5 Conclusions of GaN Nanodots Growth	54
Chapter 5 Optical Properties of GaN Nanodots	63
5-1 Experimental Details	65

5-2	GaN QDs growth mechanism	68
5-3	Micro-Photoluminescence (μ -PL) Spectra of GaN Nanodots	72
5-4	Temperature Dependent of μ -PL Spectra of GaN Nanodots	74
5-5	Conclusions of Optical Properties of GaN Nonodots	77
Chapter 6	Optical Properties of InN Nanodots	93
6-1	Experimental Details	95
6-2	Growth temperature of InN dots	97
6-3	Photoluminescence (PL) Spectra of InN Nanodots	101
6-4	Temperature Dependent of PL Spectra of InN Nanodots	103
6-5	Conclusions of Optical Properties of InN Nonodots	105
Chapter 7	Enhanced photoluminescence of InN Nanodots by FME	119
7-1	Experimental Details	121
7-2	Growth temperature	122
7-3	NH ₃ flow rate in TMIn flow period	127
7-4	Conclusions of InN Nanodots growth by FME	131
Chapter 8	Conclusions	141

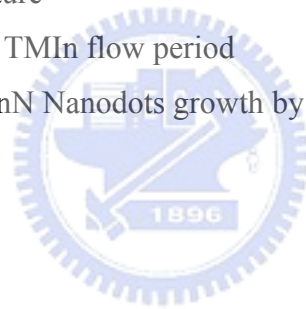


Table List

<i>Tab. 1-1</i>	Summary of three major techniques to form nitride quantum dots.	8
Tab. 2-1	Surface energy conditions of VW and SK growth modes.	12
Tab. 2-2	Values of the parameters in Varshini's equation.	18
Tab. 3-1	The detail growth conditions of AlGa _N films.	26
Tab. 4-1	The growth conditions of GaN dots on AlGa _N films.	48
Tab. 5-1	The growth condition of GaN QDs on AlGa _N films.	67
Tab. 5-2.	Sample list of GaN QDs on AlGa _N films.	69
Tab. 5-3	The calculated surface energy and wetting layer thickness of GaN QDs on different Al composition of AlGa _N films.	70
Tab. 6-1.	The detail growth conditions of InN dots on GaN films.	96
Tab. 6-2	The quantitative structural properties and emission energies of InN QDs and bulk samples.	114
Tab. 7-1	The detail growth conditions of InN dots grown by FME technique.	122
Tab. 7-2	The average height and diameter of InN dots grown at different growth temperatures from 550 to 730°C.	135

Figure List

Fig. 1-1	Carrier density at transparent condition plotted as a function of the ratio of effective mass of holes and that of electrons for quantum well (QW) lasers and quantum dot (QD) lasers. Upper curve: $m_e = 0.22 m_0$, lower curve: $m_e = 0.067 m_0$.	10
Fig. 2-1	Schematic diagram of typical films growth Frank-van-der Merwe (FvdM) mode, Volmer-Weber (VW) mode and Stranski-Krastanow (SK) mode.	20
Fig. 2-2	(a) schematic geometries of a InGaN strained film on GaN substrate for FvdM and SK mode (b) schematic geometries of a InGaN strained film on GaN substrate for FvdM and VW mode.	21
Fig. 2-3	Model of the interface energy.	22
Fig. 3-1	The optical microscope (OM) image of hillock in AlGaN films. The inset shows the 3D AFM images of hillock.	34
Fig. 3-2	The room temperature μ -PL spectra taken at different locations on OM image.	35
Fig. 3-3	The spatial μ -PL intensity distribution of I_{nbe} and I_H .	36
Fig. 3-4	The spatial μ -PL full-width-half-maximum (FWHM) distribution of I_{nbe} and I_H .	37
Fig. 3-5	Temperature dependent μ -PL measurements of AlGaN hillock from 10 to 300K.	38
Fig. 3-6	Integrated PL intensity as a function of temperature for I_{nbe} and I_H .	39
Fig. 3-7	Temperature dependence of the emission peak of I_{nbe} and I_H . Arrows indicate the transition temperature T_C .	40
Fig. 3-8	The optical microscope (OM) image of the different size hillock in AlGaN films.	41
Fig. 3-9	The room temperature μ -PL spectra taken from different size of hillock.	42
Fig. 3-10	The relation between Al composition and hillock size.	43
Fig. 4-1	A scheme showing the principle of the periodic flow-rate modulation epitaxy growth GaN dots on AlGaN films.	57

Fig. 4-2	A time chart showing the modulation of reactant molar flow rate in the periodic flow-rate modulation epitaxy.	58
Fig. 4-3	AFM images of GaN dots grown at (a) 840, (b) 870, (c) 900, (d) 930, (e) 940 and (f) 960 °C.	59
Fig. 4-4	Dependence of average diameter and height of GaN dots on growth temperature. The inset shows island density as a function of reciprocal temperature.	60
Fig. 4-5	AFM images of GaN dots grown by FME technique. The exposure times of TMGa are (a) 20, (b), 15 (c), 10 (d), 7 (e), 5 and (f) 0 s per cycle.	61
Fig. 4-6	Dependence of average diameter and height of GaN dots on exposure time of TMGa.	62
Fig. 5-1	Plane view image of a 5µm × 5µm AFM scan on (a) the Al _{0.11} Ga _{0.89} N buffer layer, the GaN QD samples grown on Al _{0.11} Ga _{0.89} N buffer layers with different FME cycles (b) 10, (c) 20 and (d) 30 cycles.	80
Fig. 5-2	Room temperature µ-PL spectra of (a) Al _{0.11} Ga _{0.89} N epilayer, the GaN QD samples grown on Al _{0.11} Ga _{0.89} N buffer layers with different FME cycles (b) 10, (c) 20 and (d) 30 cycles.	81
Fig. 5-3	The cross-section SEM images of (a) Al _{0.11} Ga _{0.89} N epilayer, the GaN with 100 FME cycles grown on Al _{0.11} Ga _{0.89} N buffer layers.	82
Fig. 5-4	Plane view image of a 2µm × 2µm AFM scan on (a) the Al _{0.11} Ga _{0.89} N buffer layer, the GaN QD samples grown on Al _{0.11} Ga _{0.89} N buffer layers with different FME cycles (b) 10, (c) 7 and (d) 3 cycles.	83
Fig. 5-5	Plane view image of a 5µm × 5µm AFM scan on (a) the Al _{0.11} Ga _{0.89} N buffer layer, the GaN QD samples grown on Al _{0.11} Ga _{0.89} N buffer layers with different NH ₃ flow rate during NH ₃ flow period of (b) 2.68×10 ⁻² , (c) 1.34×10 ⁻² , and (d) 4.46×10 ⁻³ mol/min. The TMGa flow rate was 1.99×10 ⁻⁵ mol/min.	84
Fig.5-6	Plane view image of a 5µm × 5µm AFM scan on (a) the Al _{0.11} Ga _{0.89} N buffer layer, the GaN QD samples grown on Al _{0.11} Ga _{0.89} N buffer layers with different GaN coverage of (a) 2, (b)	85

	5.5, (c) 7.3, (d) 8.2, (e) 9.1, (f) 10.9, and (g) 13.6 MLs.	
Fig. 5-7	Dot density versus average coverage plot of the GaN QDs. The solid curve is a fit using equation (5-1).	86
Fig. 5-8	3D image of a $5\mu\text{m} \times 5\mu\text{m}$ AFM scan of the GaN QD samples grown on $\text{Al}_{0.11}\text{Ga}_{0.89}\text{N}$ buffer layers with different height (a) 6.5 nm, (b) 7 nm and (c) 8.5 nm.	87
Fig. 5-9	Normalized μ -PL spectra at 10 K of (a) $\text{Al}_{0.11}\text{Ga}_{0.89}\text{N}$ epilayer, and the GaN QD samples grown on $\text{Al}_{0.11}\text{Ga}_{0.89}\text{N}$ buffer layers with different GaN coverage of (b) 9.1 MLs, (c) 10.9 MLs, and (d) 13.6 MLs.	88
Fig.5-10	Comparison with the PL experimental data and calculation derived from the disk-like rectangular box model.	89
Fig.5-11	PL peak energy as a function of temperature for the 6.5 nm (triangles), 7.0 nm (circles), 8.5 nm (squares) GaN dot and the GaN epilayer (rhombus). The dashed lines are theoretical fits using Vashini's equation.	90
Fig.5-12	PL integrated intensity as a function of temperature for the dot height of 6.5 nm, 7.0 nm, 8.5 nm and the GaN epilayer. The dashed lines represent the fitting by using the Arrhenius equation.	91
Fig. 5-13	Schematic band diagrams of GaN QDs with height of 8.5 nm (a) 10 K and (b) >100 K.	92
Fig. 6-1	AFM images of InN dots grown at (a)600, (b)625, (c)650, (d)700, (e) 720 and (f) 750 $^{\circ}\text{C}$.	107
Fig. 6-2	AFM images of InN dots grown by conventional MOCVD at (a)600, (b)650, (c)700, (d)715, (e) 730 and (f) 750 $^{\circ}\text{C}$.	108
Fig. 6-3	The QDs density depicted as a function of reciprocal temperature.	109
Fig. 6-4	Dependence of (a)average height and (b)average diameter of InN dots on growth temperature (by pulsed growth mode).	110
Fig. 6-5	Dependence of (a)average height and (b)average diameter of InN dots on growth temperature (by conventional MOCVD).	111
Fig. 6-6	The 17 K PL spectra of 600, 625, 650 and 700 $^{\circ}\text{C}$ growth temperature of InN QDs. Top insert shows the relation between FWHM and growth temperature, and down insert shows the relation between PL peak energy and dots height.	112
Fig. 6-7	Dependence of average diameter and height of InN dots on exposure time of TMIn.	113

Fig. 6-8	AFM images of InN dots with height of (a) 32.4 nm (b) 24.2 nm (c) 18.5 nm (d) 12.4 nm (e) 6.5 nm.	115
Fig. 6-9	17 K PL spectra of InN bulk and InN dots with height of (a) 32.4 nm (b) 24.2 nm (c) 18.5 nm (d) 12.4 nm (e) 6.5 nm. The insert shows the relation of peak energy and dots height. The electron effective mass of $0.042m_0$ (solid line) and $0.07m_0$ (dotted line) were assumed in this calculation.	116
Fig. 6-10	Temperature dependence of the PL peak energy of InN dots and bulk samples.	117
Fig. 6-11	Temperature dependence of the PL integrated intensity of InN dots and bulk samples.	118
Fig. 7-1	The typical gas flow sequence of the formation of InN dots for FME and conventional MOCVD.	134
Fig. 7-2	The InN dots density depicted as a function of reciprocal temperature.	136
Fig. 7-3	The 10 K PL spectra of InN dots grown by (a) conventional MOCVD and (b) FME growth technique at growth temperature of 550 to 730°C, respectively.	137
Fig. 7-4	The relations between density and aspect ratio of InN dots and NH_3 flow rate (r_0) during TMIn period.	138
Fig. 7-5	The 10 K PL spectra of InN dots grown by conventional MOCVD and FME technique with different NH_3 flow-rate (r_0) during TMIn flow period.	139
Fig. 7-6	(a)-(f) show typical surfaces of InN dots grown under the r_0 values of 0, 500, 1000, 5000 and 10000 sccm and conventional MOCVD growth technique, respectively.	140

Chapter 1 Introduction

1-1 III-nitride micro-structures

GaN and its alloys with Al and In recently became the fundamentally important materials for optoelectronics. This is due mainly to their direct bandgap feature which not only covers the whole visible spectrum, but also extends into both UV and infrared regions. At present, high brightness blue and green light-emitting diodes (LEDs) and low-power blue laser diodes (LDs) are commercially available. Nevertheless, the development of GaN-based technology was and still is, suffering from the lack of high quality, lattice-matched substrates, such as GaN, AlN or InN etc.

Apparently, GaN and its alloy are much more 'tolerant' of the presence of structural defects than the conventional III-V systems, stemming from low minority carriers' diffusion length and immobility of structural defects in these strongly bonded crystals. Despite the remarkable progress being made in the last decade in growing morphologically good hetero-epitaxial GaN layers, the as grown nitride film still shows a very high density of diverse defects, in particular, dislocations, inversion domains (IDs), nano-pipes, stacking faults and V-shaped pits are of continued concern to crystal growers [1-6]. For high-power optoelectronic and elevated- temperature device applications, the present structural characteristics of hetero-epitaxial GaN seem to be insufficient. It has been shown that dislocations in GaN epitaxial layers do indeed have nonradiative and recombinative properties [7-10]. For example, there are three different types of threading dislocations, edge, mixed, and screw types. It is reported that threading dislocations having a screw-component burgers vector act as strong nonradiative centers in GaN epitaxial layers, whereas edge dislocations, which are the majority, do not act as nonradiative centers.

For the V-shaped defects, it was found that the mechanism of V-defects

formation strongly depends on the In and Al compositions in $\text{In}_x\text{Ga}_{1-x}\text{N}$ and $\text{Al}_x\text{Ga}_{1-x}\text{N}$ layers, respectively [11]. By increasing the In composition, the origin of V-defects is changed from the vertex of threading dislocations to the stacking mismatch boundaries induced by stacking faults and the three-dimensional island growth at the initial stage due to the large lattice mismatch. By increasing the Al composition, the origin of the V-defects also varied from the surface undulation due to the elastic misfit strain to the vertex of threading dislocations. Further study reveals that the V-defect is correlated with the localized excitonic recombination centers which giving rise to a long-wavelength shoulder in photoluminescence (PL) and CL spectra.

Beside the dislocations and V-shaped defects studies, one of the structural features often reported in microscopic observations of the surface of GaN epitaxial films is the presence of growth hillocks with a wide range of sizes, typically several microns, with a hexagonal shape. Qian *et al.* [12] have reported observations relating the hexagonal hillocks to the presence of nanopipes emerging at their centers and concluded that nanopipes are the open cores of screw dislocations. Middleton *et al.* [13] in a CL study of pyramidal hillocks found that in the center only the yellow emission is present and suggested that it originates from defects associated with inversion domain boundaries.

It must be pointed that most of the recent studies of hillocks were focused on GaN material, very few results on AlGaN material. It is known that due to its wide, direct bandgap and other superior characteristics, an AlGaN system is regarded as one of the most promising materials for application in UV opto-electronics and high-temperature, high power electronics. Thus, studies of AlGaN hillocks were important for getting better understanding of AlGaN based UV opto-electronic devices. Because the spatial resolution of CL was better than PL, the optical

properties of III-nitride microstructures were usually studied by CL system. However, the temperature dependent of CL spectra can't achieved by CL equipment. In order to obtain temperature dependent optical equipment for observed III-nitride microstructures. We needed to improve the spatial resolution of PL system. Therefore, our laboratory has developed a UV to visible micro-photoluminescence (μ -PL) system. By using UV lens, the laser spot could be focused in diameter of $1.5 \mu\text{m}$. We are able to study the spatial dependent photoluminescence of AlGaIn hillocks using μ -PL system.

For AlGaIn hillocks, μ -PL spectra indicted there is a strong emission peak (I_H) at 351 nm for hillock itself, in addition to peak emission at 341 nm from the matrix. The hillock-associated μ -PL intensity increases significantly as the probing spot scan from peripheral to the center, accompanied with the reduction of FWHM from 76 to 53 meV. The temperature-dependent μ -PL measurements showed that the I_H also has the S-shape behavior with a transition temperature of $\sim 120\text{ K}$ is lower than that of $I_{matrix}(\sim 150\text{K})$. Despite of concurrent growth of AlGaIn hillocks and matrix during sample preparation, further study by EDX clearly indicates the discrepancy in emission wavelength between AlGaIn hillocks and surrounding matrix is mainly due to composition different in Al component. That is the composition of Al in hillocks is 6%, 6% lower than that in matrix which is beyond our expectations at the beginning. Moreover, we also observed that the Al composition decreased $\sim 2\%$ as the diameter of AlGaIn hillock increased from $6 \mu\text{m}$ to $11 \mu\text{m}$.

1-2 Low-dimensional structures

For the past few decades, low-dimensional quantum structures, such as quantum wells (QWs), quantum wires (QWRs), and quantum dots (QDs) have been attracting lots of interests due to their potential advantages compared with bulk materials. Among these, QDs are expected to be the most promising due to their unique electronic states, such as δ -function-like density of states, three-dimensional (3D) carrier confinement, etc. Due to their unique properties, the semiconductor laser with a QD active layer is expected to have ultra-low threshold current, reduced temperature sensitivity, narrower spectral linewidth, and high-modulation bandwidth, etc [14]. Furthermore, the semiconductor photodetector with QDs are also expected to have the sensitivity for the normally incident light, enhanced photoexcited carrier lifetime, reduced dark current, and higher electric gain.

It was in 1982 that the concept of QDs was proposed by Arakawa and Sasaki for the first time as artificial atoms for semiconductor laser application [15]. Since then, there has been lots of research devoted to the realization of predicted potential advantages of QDs. However, it took about 10 years to realize the fabrication of the practical QD structures. In the 1990s, both selective growth and self-assembled growth technique without the formation of nonradiative defects were well developed. Particularly, the Stranski-Krastanow (SK) growth mode was very successful for InGaAs/GaAs systems [16]. As a result, lasers, detectors for both inter-band transitions have been successfully demonstrated using the InGaAs/GaAs QDs [17]. From the late 1990s this material system has been extended to other material system.

Among those material systems, nitride semiconductors have recently received the most attention for applications to blue and ultraviolet (UV) light emitting devices, especially, due to the great impact of QDs in GaN-based LDs [18]. The improvement

of threshold current due to the QDs can be more enhanced in wider bandgap semiconductors owing to the following reasons. Generally, threshold current of the QW lasers is increased if the effective mass of electrons m_e or the effective mass of holes m_h to that of electrons m_e is larger. Unfortunately, in GaN-based semiconductors these are larger compared to GaAs-based semiconductors. To see this, we calculated the carrier transparent density n_{tr} at conditions under which the material becomes transparent. The threshold current is described by the following equation:

$$I_{th} = \gamma e V n_{tr}^{\tau} \quad (1-1)$$

where γ is a constant, the value of which is in the range of 1.2-1.5, V is the total volume of the active region, n_{tr} is the carrier density at transparent condition, and τ is the carrier lifetime. Fig. 1-1 shows the calculated n_{tr} as a function of m_h/m_e for two effective masses of electrons ($m_e=0.22m_0$ for GaN and $0.067m_0$ for GaAs) [19]. As indicated in this figure, n_{tr} increases monotonically with the increase of m_h/m_e . Moreover, n_{tr} is also larger when m_e becomes larger. This difference in n_{tr} leads to a difference in the minimum threshold current density J_{th} ; J_{th} of GaN-based QW lasers is $\sim 1\text{kA/cm}^2$, while that of GaAs-based QW lasers is $\sim 100\text{ A/cm}^2$.

On the other hand, it was suggested that, if QDs are used in the active region and the size of the QDs is small enough that the population of carriers in the higher subband can be ignored, the achievable threshold current I_{th} in both GaAs-based and GaN-based LDs is almost the same, about $100\text{nA}-1\ \mu\text{A}$. Therefore, with the use of QDs, the threshold current density is reduced by a factor of 100 in GaN-based LDs, which value can compare to that in GaAs-based LDs, suggesting that the impact of QDs is much bigger in GaN-based LDs than in GaAs-LDs.

The promising aspect in the applications of the nitride QDs is also confirmed in the emission mechanism of the InGaN active layer. InGaN active layers for blue and

green LEDs are known to have excellent optical properties despite the presence of high-density defects. It is widely accepted that their high-luminescence efficiency is due to the carrier localization induced by the presence of compositional fluctuation and/or QD-like features usually in high In-content InGaN layers [20].

Achieving confinement in all three dimensions requires lateral control on the same 1-100 nm length scale, and is much more difficult. For example, standard UV photolithography cannot yet produce such small features. While more exotic lithographic techniques, such as x-ray lithography or electron beam writing, do have adequate resolution to pattern QDs, they are comparatively expensive and not yet commonly used. Since the late 1990s, several methods to form QDs using nitride semiconductors were suggested. They can be categorized mainly into three methods: (1) using SK growth method, (2) using “anti-surfactant”, (3) using selective epitaxy.

One of the most attractive method for defect-free QD formation is the SK growth in lattice-mismatched semiconductor systems, widely used in the QD fabrication of many material systems, such as InGaAs/GaAs, InAs/InP, InP/GaAs, GaSb/GaAs, InSb/InP, SiGe/Si, ZnCdSe/ZnSe, etc. In the SK growth mode, the mismatched epitaxy is initially accommodated by biaxial compression in a layer-by-layer (2D) growth region, traditionally called as “wetting layer”. After the deposition of a few monolayer, the strain energy builds up. Then, the evolution to 3D islands becomes more favorable than the continued, strained planar growth. Such islands are referred to as self-assembled QDs.

Nitride semiconductors can be epitaxially grown to form a strained heterostructure, which is indispensable for the SK growth mode. The lattice mismatch between AlGaN and GaN ranges from 0 to 2.4%, which is only to have two growth modes (the strained layer-by-layer 2D growth mode, the SK growth mode). However,

the lattice mismatch between InGaN and GaN ranges from 0 to 11.1%, which is sufficiently large to have all growth modes (the strained layer-by-layer 2D growth mode, the SK growth mode, and the relaxed 3D growth mode). By the proper combination of QD and substrate materials, the extent of strain in the film and subsequent QD growth behavior can be controlled.

The nitride QDs were also demonstrated by using “anti-surfactant” [21]. The pretreatment of the growth surface by anti-surfactant, such as tetraethylsilane (TESi), were found to result in the 3D growth mode of the subsequent layer, even in the case with little lattice-mismatched. The presence of the wetting layer was not confirmed in the QDs grown by this method. Since this growth mode does not require lattice mismatch, the restriction in the choice of film/substrate combination can be somewhat relaxed.

Finally, selective epitaxy is also employed to fabricate QDs in nitride materials [22]. Selective epitaxy attempted in growing nitride QDs is quite similar to the method of patterning QWs, that generally used in other III-V compound semiconductors. In this case, at first, pyramidal structures are grown on a patterned substrate using selective epitaxy. QDs are then grown on top of those pyramidal structures. The use of selective epitaxy in growing GaN QDs has several advantages overwhelming the method of patterning QWs, such as (1) the possibility of arbitrary lateral shape, size, and position realization, (2) general compatibility with the modern ULSI technologies in the patterning process of this method. However, there are some drawbacks, such as defects or damages induced by etching process.

Besides the techniques described above, other novel techniques were also attempted to fabricate the nitride QDs, such as the nitridation of metallic droplets [23], the surface passivation and/or pretreatment [24], the laser ablation [25], the ion

implantation [26], the colloidal synthesis [27], etc. Table 1-1 summarizes the three major techniques for nitride QD formation and material systems explored.

Table 1-1: *Summary of three major techniques to form nitride quantum dots.*

Technique	Research Group	Author	Growth system	Material system
SK mode	CEA-Grenoble	Daudin et al.	MBE	GaN/AlN, InGaN/GaN
	CNRS	Damilano et al.	MBE	GaN/AlN/Si; InGaN/GaN
	Tokyo Univ.	Tachibana et al.	MOCVD	GaN/AlN/6H-SiC; InGaN/GaN
	Seoul National Univ.	Kim et al.	MOCVD	In-rich InGaN/GaN
	Montpellier II Univ.	Briot et al.	MOCVD	InN/GaN
Anti-surfactant	RIKEN	Tanaka et al.	MOCVD	GaN/AlGaIn/6H-SiC
Selective growth	Tokyo Univ.	Tachibana et al.	MOCVD	InGaN/GaN; GaN/AlGaIn
	Tokushima Univ.	Wang et al.	MOCVD	InGaN/GaN

In this thesis, we used a growth technique, namely “flow-rate modulation epitaxy growth (FME)” to synthesize self-assembled QDs. In this process, nanodots can be grown on buffer layers of almost any materials, giving a great versatility in material selectivity. In other words, by using the FME method, we are able to prepare self-assembled nanodots on any degree of lattice mismatched substrate, even on slightly mismatched or completely matched substrate. Consequently, due to the maskless feature of FME method, the fabrication cost of self-assembled nanodots can be effectively reduced.

The FME included following procedures: at the first process where turned on the purge gas and modulated the first precursor to the lower first flow rate. Then the second precursor is supplied to the buffer layer to form a metal and metal-rich island on the buffer layer for the second process. A third process, where turn on purge gas again and modulated the first precursor to the higher second flow rate onto the buffer layer on which the metal-rich island is formed in the second process. The metal-rich island is formed in the III-nitride nanodots.

In chapter 4, for the GaN nanodots, we have demonstrated that the GaN dots can be grown on a slightly lattice-mismatched $\text{Al}_{0.11}\text{Ga}_{0.89}\text{N}$ epilayer using FME. Because of the alternating gas supply nature in FME, we consider that the dot growth studied here is mainly via the Volmer-Weber growth mode, not through the Stranski-Kranstanow growth mode. Our results indicate that the FME growth technique is a very promising tool for preparing self-organized quantum dot structures for most practical devices due to the release of requirement of large lattice mismatch between the grown dot structure and substrate. In addition, in chapter 6, FME technique was also used for growth of self-assembled InN dots on GaN films. The aspect ratio (i.e. height/diameter) of InN dots is found to be decreased greatly by the use of FME technique, as compared with conventional MOCVD deposition due to enhanced migration of In species and hence reduced defects in the dots structure. Photoluminescence measurement also supports that the quality of InN dots grown by the FME method is superior to that of layers grown by continuous growth mode.

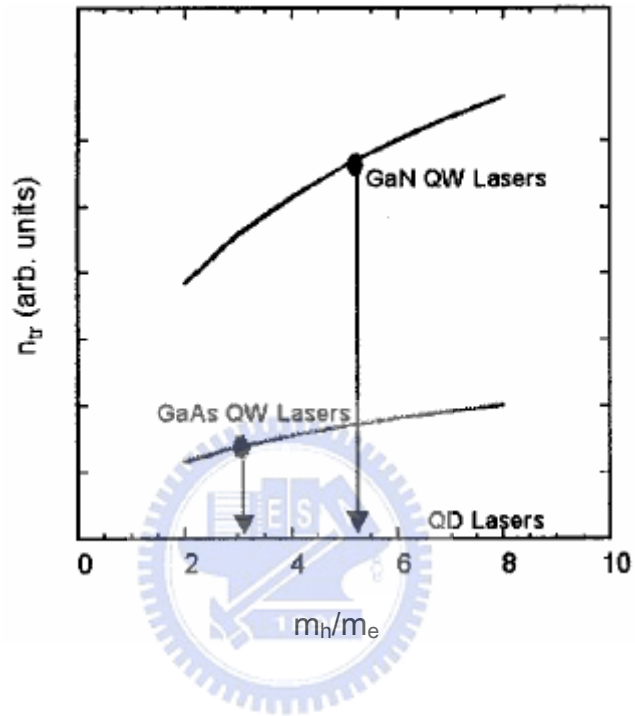


Fig. 1.1 Carrier density at transparent condition plotted as a function of the ratio of effective mass of holes and that of electrons for quantum well (QW) lasers and quantum dot (QD) lasers. Upper curve: $m_e = 0.22 m_0$, lower curve: $m_e = 0.067 m_0$.

Chapter 2 Theoretical Backgrounds

Historically, the growth of thin films has been categorized into three types : (1) Frank-Van der Merwe (FM) (2D layer-by-layer), (ii) Volmer-Weber (VW) (3D islands), and (3) Stranski-Krastanow (SK) (2D layer followed by 3D islands). In Fig. 2-1, we show three fundamental growth features in growing thin films materials. These modes are deduced from equilibrium considerations of the surface and interface energies of lattice matched systems. In most practical applications the epitaxy of semiconductors profits from the existence of conditions where the layer-by-layer deposition mechanism (FM) occurs. This mechanism is typically realized for nearly lattice-matched combinations (i.e. <1%) with high interfacial bond energies, low supersaturation to suppress 3D nucleation, such a deposition manner are particularly favorite at high temperature on a slightly lattice-mismatched substrate. On the other hand, the SK growth mode operates in relatively higher mismatched systems (i.e. ~2-10%) in which strained films can grow in registry with the substrate until reaching a critical thickness, t_c . At this thickness the accumulated elastic strain energy initiates the formation of dislocations and the strain can be partially relaxed by the formation of a dislocation network and/or relieved partially through the formation of 3D islands. Combinations of highly mismatched (>10%) and dissimilar materials, Au/NaCl, on the other hand, preferentially crystallize in the Volmer-Weber mode, forming islands or clusters on the bare unwetted surface.

2-1 Quantum Dots Growth Mechanisms

The primary factors that determine the island growth manner of deposition of epitaxial film on substrate are the surface free energy of the substrate ($\sigma_{\text{substrate}}$), the surface free energy of the deposited film (σ_{film}), and the interface strain energy ($\sigma_{\text{interface}}$). The interface strain energy includes the interface energy (σ_{if}) due to lattice mismatch between substrate and deposited film and the strain energy (σ_{st}) due to induced strain caused by wetting layer and island film itself, which is increased with the increasing thickness of wetting layer. Table 2-1 list the required surface energy conditions for the SK and the VW growth modes. For both island growth modes, the sum of the surface free energy of the deposited film and their interface strain energy has to be greater than the surface free energy of substrate.

Table 2-1: *Surface energy conditions of VW and SK growth modes*

Surface energy conditions	
VW mode	$\sigma_{\text{substrate}} < \sigma_{\text{film}} + \sigma_{\text{interface}}, (\sigma_{\text{interface}} = \sigma_{\text{if}} + \sigma_{\text{st}}(t), t < \text{one lattice layer})$
SK mode	$\sigma_{\text{substrate}} < \sigma_{\text{film}} + \sigma_{\text{interface}}, (\sigma_{\text{interface}} = \sigma_{\text{if}} + \sigma_{\text{st}}(t), t > \text{one lattice layer})$

As shown in Fig. 2-2, the primary difference between these two modes is the thickness of wetting layer. If the required wetting layer thickness to produce island growth is greater than one lattice layer, the associated island growth mode is categorized into SK growth mode, if not, VW mode.

Surface energy

On the surface between the vapor and solid phases, the surface energy per unit area γ_s can be given approximately by :

$$\gamma_s = (1 - w/u)\Delta H_{v0} N_0^{2/3} \quad (2-1)$$

where u is the number of nearest neighbors of an atom in the bulk of the crystal and w is the number of nearest neighbors in the crystal of an atom on the surface in question. So, w/u means the number of bonds which connect a surface atom to atoms in the crystal, and $(1-w/u)$ means the number of dangling bonds of an atom on the surface. ΔH_{v0} is the enthalpy of evaporation of the material, and N_0 is the number of atoms per unit volume. The argument used is that the surface energy is the energy to break all of the nearest-neighbor bonds across a given plane. The number of atoms per unit surface area N_s can be related to N_0 as follows:

$$N_s = N_0^{2/3} \quad (2-2)$$

for a III-V wurtzite-type compound, N_s is given by:

$$N_s = \frac{2}{\sqrt{3}a^2} \quad (2-3)$$

for the (0001) face, where a is the lattice constant of the III-V binary compound. For growth from vapor, ΔH_{v0} is given by the enthalpy of evaporation per mole ΔH as follows:

$$\Delta H_{v0} = \frac{\Delta H}{2N_A} \quad (2-4)$$

where N_A is Avogadro's number ($N_A = 6.023 \times 10^{23}$). ΔH is estimated using Stringfellow's model written by :

$$\Delta H = Ka^{-2.5} \quad (2-5)$$

a is the lattice constant of the binary compound and the value of K is 1.15×10^7

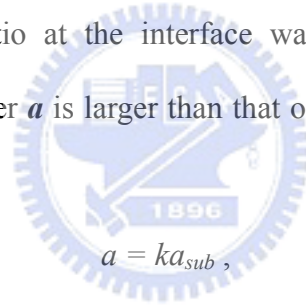
cal/mole-Å^{2.5}. Therefore, the surface energy σ can be written as follows:

$$\sigma = (1 - \alpha)A_s\gamma_s = \frac{(1 - \alpha)A_s\Delta H}{4\sqrt{3}a^2N_A} \quad (2-6)$$

for the (0001) face where w is 3 and u is 4, A_s is the surface area of unit cell (here QD), and α is the reconstruction ratio of dangling bonds on the surface. A part of dangling bonds on the surface makes bonds with each other on the surface. The number of dangling bonds decreases as α increases.

Interface energy

In order to calculate roughly the energy σ_{if} of the interface between the film and the substrate (FM and SK modes) or that between the cluster and the substrate (the VW mode), the bonding ratio at the interface was calculated. When the lattice constant of the film and cluster a is larger than that of the substrate a_{sub} ($a > a_{sub}$), a is given by



$$k = \Delta a / a + 1 = (a - a_{sub}) / a_{sub} + 1 \quad (k \geq 1) \quad (2-7)$$

where $\Delta a / a$ means the lattice misfit between the film (or cluster) and the substrate.

In this calculation, as shown in Fig. 2-3, we assumed that at the interface all dangling bonds on the film and cluster side are bonding with dangling bond on the substrate side. At the interface, assuming the bonding ratio β_1 on the upper film or cluster side is given by

$$\beta_1 = 1,$$

and the bonding ratio β_2 on the substrate side can be expressed by

$$\beta_2 = \frac{1}{k},$$

where this means that the fraction $1/k$ of the dangling bonds are satisfied. The interface energy per unit area γ_i can be given by

$$\gamma_i = (1 - \beta_1)\gamma_s + (1 - \beta_2)\gamma_{sub} = \left(1 - \frac{1}{\Delta a/a + 1}\right)\gamma_{sub} \quad (2-8)$$

where γ_{sub} is the surface energy per unit are of the substrate. Therefore, the interface energy σ_{if} can be written as follows:

$$\sigma_{if} = A_i\gamma_i = A_i\left(1 - \frac{1}{\Delta a/a + 1}\right)\frac{\Delta H}{4\sqrt{3}a^2N_A} \quad (2-9)$$

Strain energy

For the calculation of the strain energy, the method developed by Nakajima et al., is used in order to calculate the precise stress distribution of an island on top of a substrate. In this method, the island is divided into many imaginary thin layers with coherent interfaces. Shear lag analysis is then used to calculate the longitudinal stress distribution over the imaginary thin layers in the FM, SK, and VW mode structures.

The total strain energy of each structure σ_{st} which includes the strain energy of the layer, cluster, buffer layer, and substrate is given by

$$\sigma_{st} = \sum_{i=1}^m U_i = \sum_{i=1}^m \frac{A_i d_i \sigma_i^2}{2E_i} \quad (2-10)$$

where U_i is the elastic strain energy in the i th imaginary thin layer, m is total number of thin layers which constitute each structure, and σ_i , E_i , A_i and d_i are the stress (N/m²), Young modulus (GPa), surface area (m²), and thickness (m) of the i th thin layer.

Thus, the growth mode dependent part of the free energy σ_f can be given as:

$\sigma_f = \sigma + \sigma_{if} + \sigma_{st}$. All the surface energy calculation will be described in chapter 4.

2-2 Photoluminescence (PL), Temperature Dependent of PL Spectra

The photoluminescence (PL) was used for measurement of the optical properties of GaN and InN nanodots in this thesis. It was known that the PL is a powerful and non-destructive technique to probe the optical emission properties of materials, especially in luminescent semiconductors. The auto mapping PL system is also widely used in the industry to monitor the quality of semi-finished devices on wafer. By analyzing the PL spectra, a set of characteristic spectral features can identify the impurity types, the band gap energy, one can estimate the contents in compound semiconductors. PL analysis can also survey buried interfaces of heterostructures which are difficult to be probed by direct physical and electrical contacts. However, it is difficult to find the correlation between the spectral line intensity and concentration of the specific impurity, due to variation of non-radiative recombination through deep-levels or surface recombination centers. The luminescence process typically involves three steps: excitation, thermalization, recombination. The electron-hole pairs generated by incident light, through quasi-thermal equilibrium distribution, will recombine and produce photons. The impurities and defects can form various energy levels in the band gap, and the corresponding energies will be estimated by radiative recombination process or absorbed by non-radiative recombination process. The transition rates of these impurities are different due to various matrix elements and density of states at respective energy levels. The luminescence of semiconductors can be divided into three regions: the excitonic edge emission, the donor-acceptor pair emission, and deep level related emission.

A relation for the variation of the energy gap (E_g) with temperature (T) in semiconductors is proposed [28]:

$$E_g = E_0 - \alpha T^2 / (\beta + T) \quad (2-11)$$

where E_g is the energy gap which may be direct or indirect, E_0 is its value at 0 K, α and β are constants.

Most of the variation in the energy gap with temperature is believed to arise from the following two mechanisms:

- (1) A shift in the relative position of the conduction and valence bands due to the temperature-dependent dilatation of the lattice. Theoretical calculations show that the effect is linear with temperature at high temperatures. In that region this effect accounts for only a fraction (about 0.25) of the total variation of the energy gap with temperature. At low temperature the thermal expansion coefficient is nonlinear with T; indeed for a number of diamond structure solids it even becomes negative over a certain temperature interval. Correspondingly the dilatation effect on the energy gap is also nonlinear.
- (2) The major contribution comes from a shift in the relative position of the conduction and valence bands due to a temperature-dependent electron lattice interaction. Theoretical treatments show that this leads to a temperature dependence of the following form:

$$\begin{aligned} T \ll \theta, \quad \Delta E_g &\propto T^2 \\ T \gg \theta, \quad \Delta E_g &\propto T \end{aligned}$$

where θ is the Debye temperature.

Eq. (1) is consistent with the theoretical results if we assume that $\beta \approx \theta$. The constants in eq. (1) were evaluated from the experimental data for a member of semiconductors and are recorded in Table 2-2.

Table 2-2: Values of the parameters in Varshini's equation

Values of the parameters in Varshini's equation				
Substance	E_0 (eV)	α ($\times 10^{-4}$)	β	Debye θ ($^{\circ}K$)
Diamond	5.4125	-1.979	-1437	2220
Si	1.1557	7.021	1108	645
Ge	0.7412	4.561	210	374
SiC	3.024	-0.3055	-311	~ 1150
GaAs	1.5216	8.871	572	344
InP	1.4206	4.906	327	301
InAs	0.426	3.158	93	248
AlN	6.23	1.799	1462	800
GaN	3.507	0.909	830	570
InN	0.69	0.414	454	370

Generally, bandgap energies of semiconductor decreases with increasing temperature, namely, $E_0(T) = E_0 - \alpha T^2 / (\beta + T)$, where α and β are known as Varshini's fitting parameters. For wurzite GaN, it has been reported that $\alpha=0.909$ meV and $\beta=830K$ for the temperature variation of A-exciton transition. This shows that the temperature-induced red shift of transition energies is about 60 meV between 0K and 300K.

The temperature dependence of the PL integrated intensity of films was generally used to identify the mechanism of the PL quenching. In the bulk GaN (D^0, X) process, the thermal dissociation of donor bound excitons involves two activation energies, namely the localization energy and exciton binding energy [29-30]. At low temperature, the free excitons tend to localize at the neutral donors (localization energy) so that there is interplay between the localization and ionization of neutral donors to reduce the number of available neutral donors. In this study, we also use the following formula to fit our results,

$$I(T) = \frac{I(0)}{\left[1 + C_1 \exp\left(-\frac{E_a}{kT}\right) + C_2 \exp\left(-\frac{E_{loc}}{kT}\right) \right]} \quad (2-12)$$

where $I(T)$ and $I(0)$ are the integrated intensity at temperatures T and 0 K. C_1 and C_2 are fitting parameters. E_a and E_{loc} are the activation energies at the high and low temperature regime, respectively.

The localization state may be one of below cases: (1) Interface fluctuations particularly in narrow QWs, produce localization states for excitons and that such localization states act like QD. (i.e. localization of excitons in either QDs or potential minima in QWs). (2) Localization of the free exciton at neutral donors. (3) Detrapping of excitons from interface roughness fluctuation. (4) Potential fluctuations can be realized, for example, by CdSe islands with size fluctuations etc.

For AlGaIn/GaN MQWs case, From N Grandjean et al. report [31], taking into account the competitive non-radiative channel introduced by the dislocations, the PL intensity is given by Eq (2-12). The best fit of the experimental data is obtained with $E_{a1} = 125$ meV and $E_{a2} = 12$ meV. The 12 meV activation energy is consistent with the localization energy and accounts for the detrapping of excitons from interface roughness fluctuation. The activation energy of 125 meV corresponds to the carrier thermal escape out the well.

Frank- van der Merwe



- Layer by layer growth
- Lattice matched
- GaN on AlGaN

Volmer-Weber



- Direct island growth
- Large lattice mismatched
- GaN on sapphire

Stranski-Krastanow



- Layer by layer followed
by island nucleation
- Dissimilar lattice spacing

Fig. 2-1 Schematic diagram of typical films growth Frank-van-der Merwe (FvdM) mode, Volmer-Weber (VW) mode and Stranski-Krastanow (SK) mode.

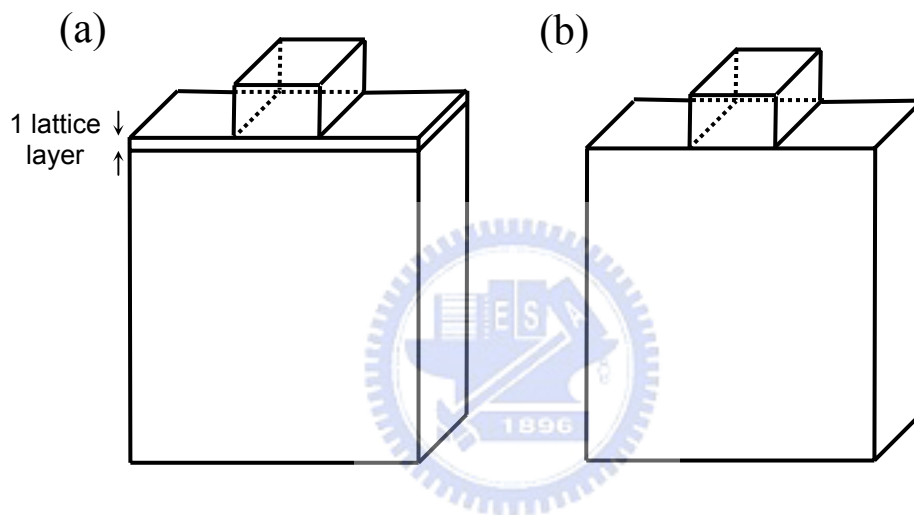


Fig. 2-2 (a) schematic geometries of a strained film on substrate for (a) SK mode and (b) VW mode.

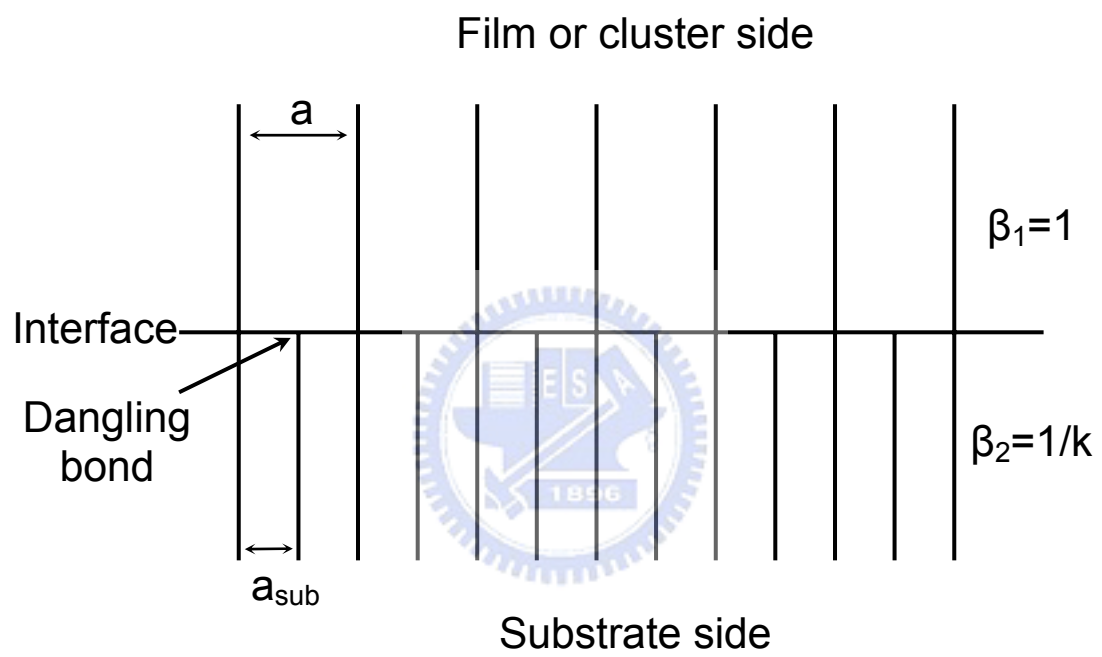


Fig. 2.3 Model of the interface energy.

References

- [1] B. Pěcz and Zs. Makkai, *Appl. Phys. Lett.*, **78**, 1529 (2001)
- [2] L. T. Romano and T. H. Myers, *Appl. Phys. Lett.*, **71**, 3486 (1997)
- [3] J.L. Weyher, P.D. Brown, A.R.A. Zauner, S. Müller, C.B. Boothroyd, D.T. Foord, P.R. Hageman, C.J. Humphreys, P.K. Larsen, I. Grzegory, S. Porowski, *J. Cryst. Growth*, **204**, 419 (1999)
- [4] W. Qian, G. S. Rohrer, and M. Skowronski, *Appl. Phys. Lett.*, **67**, 2284 (1995)
- [5] R. Liu, A. Bell, F. A. Ponce, C. Q. Chen, J. W. Yang, and M. A. Khan, *Appl. Phys. Lett.*, **86**, 21908 (2005)
- [6] S. K. Hong, T. Yao, B. J. Kim, S. Y. Yoon, and T. I. Kim, *Appl. Phys. Lett.*, **77**, 82 (2000)
- [7] Sergey Yu. Karpov and Yuri N. Makarov, *Appl. Phys. Lett.*, **81**, 4721 (2002)
- [8] S. F. Chichibu, M. Sugiyama, T. Onuma, T. Kitamura, H. Nakanishi, T. Kuroda, A. Tackeuchi, T. Sota, Y. Ishida, and H. Okumura, *Appl. Phys. Lett.*, **79**, 4319 (2001)
- [9] S. J. Rosner, E. C. Carr, M. J. Ludowise, G. Girolami, and H. I. Erikson, *Appl. Phys. Lett.*, **70**, 420 (1997)
- [10] E. F. Schubert, I. D. Goepfert, W. Grieshaber, and J. M. Redwing, *Appl. Phys. Lett.*, **71**, 921 (1997)
- [11] H. K. Cho and J. Y. Lee, *Appl. Phys. Lett.*, **80**, 1370 (2002)
- [12] W. Qian, G. S. Rohrer, and M. Skowronski, *Appl. Phys. Lett.*, **67**, 2284 (1995)
- [13] P. G. Middleton, C. Trager-Cowan, A. Mohammed, K. P. O'Donnell, W. Van Der Stricht, I. Moerman, and P. Demeester, *Mater. Res. Soc. Symp. Proc.* **449**, 471 (1997).
- [14] P. Caroff, C. Paranthoen, C. Platz, O. Dehaese, H. Folliot, N. Bertru, C. Labbé, R. Piron, E. Homeyer, A. Le Corre, and S. Lualiche, *Appl. Phys. Lett.* **87**, 243107 (2005).
- [15] Y. Arakawa and H. Sakaki, *Appl. Phys. Lett.* **40**, 939 (1982).
- [16] G. Saint-Girons, G. Patriarche, L. Largeau, J. Coelho, A. Mereuta, J. M. Moison, J. M. Gérard, and I. Sagnes, *Appl. Phys. Lett.* **79**, 2157 (2001).
- [17] Kazunari Ozasa, Yoshinobu Aoyagi, Young Ju Park, and Lars Samuelson, *Appl. Phys. Lett.* **71**, 797 (1997).
- [18] Yukio Narukawa, Yoichi Kawakami, Mitsuru Funato, Shizuo Fujita, Shigeo Fujita, and Shuji Nakamura, *Appl. Phys. Lett.* **70**, 981 (1997).

- [19] T. O. Poehler, Appl. Phys. Lett. **20**, 69 (1972).
- [20] Yen-Lin Lai, Chuan-Pu Liu, and Zheng-Quan Chen, Appl. Phys. Lett. **86**, 121915 (2005).
- [21] Satoru Tanaka, Sohachi Iwai, and Yoshinobu Aoyagi, Appl. Phys. Lett. **69**, 4096 (1996).
- [22] Tachibana, K.; Someya, T.; Ishida, S.; Arakawa, Y., J. Cryst. Growth, **237**, 1312 (2002)
- [23] C.-W. Hu, A. Bell, F. A. Ponce, D. J. Smith, and I. S. T. Tsong, Appl. Phys. Lett. **81**, 3236 (2002).
- [24] J. Zhang, M. Hao, P. Li and S. J. Chua, Appl. Phys. Lett. **80**, 485 (2002).
- [25] Timothy J. Goodwin, Valerie J. Leppert, Subhash H. Risbud, Ian M. Kennedy and Howard W. H. Lee, Appl. Phys. Lett. **70**, 3122 (1997).
- [26] E. Borsella, M. A. Garcia, G. Mattei, C. Maurizio, and P. Mazzoldi, J. Appl. Phys. **90**, 4467 (2001).
- [27] O. I. Mičić, S. P. Ahrenkiel, D. Bertram, and A. J. Nozik, Appl. Phys. Lett. **75**, 478 (1999).
- [28] Varshni Y P, *Physica* **34**, 149 (1967)
- [29] K. O'Donnell et al., in *Group III Nitride Semiconductor Compounds: Physics and Applications*, edited by B. Gil (Clarendon Pr, New Zealand, 1998), pp. 247-248.
- [30] A. Bimberg and M. Sondergeld, Phys. Rev. B **4**, 3451 (1971).
- [31] N Grandjean, Semicond. Sci. Technol. **16**, 358 (2001).

Chapter 3 Hillocks in Al_{0.11}Ga_{0.89}N Films

AlGaN is a wide bandgap semiconductor with many important applications including high-temperature and high-power electronics, solar-blind photodetectors, blue and ultraviolet light emitting and laser diodes [1-3]. However, AlGaN grown on sapphire substrate often contains a large amount of dislocations due to lattice mismatch. Even with recent improvements, as due to introduction of low temperature AlN or GaN buffers, AlGaN films grown in this fashion still consist of a mosaic of slightly misoriented domains of micro size with lots of microstructure like dislocations, grain boundaries, V-defect, hillocks, pores... etc. [4-5]. Thus, the detailed analysis of the spectra and spatial distribution of microstructure is very important to improve material quality. Nevertheless, microstructures sometimes show particular optoelectronic properties. For example, the hexagonal hillocks with dimensions of several microns are often observed on the surface of GaN layers. They are characterized by a high intensity of the band gap luminescence, while the boundaries of the hillocks are enriched with defects responsible for yellow luminescence at ~2.2 eV [6-7]. So far, the light emission from microstructures is commonly studied by using cathodoluminescence (CL), because the nano-probe produces secondary electron images in CL with high spatial resolution, as well as point analysis on specific areas. However, no report about micro-photoluminescence (μ -PL) studies of the microstructures of III-V nitride semiconductor appeared up to now. In this Letter, the spatial variation of μ -PL was studied to characterize the optical properties of AlGaN hillocks. The temperature dependent μ -PL spectra from 10K to 300K were obtained to show the interesting emission behaviors of the hillock.

3-1 Experimental details

The AlGa_N films were grown on AlN/sapphire (0001) substrates by low-pressure metalorganic vapor phase epitaxy (MOVPE) system in a horizontal reactor. Trimethylgallium, trimethylaluminum, and ammonia were used as the source precursors for Ga, Al, and N, respectively. Hydrogen was used as the carrier gas. Prior to material growth, the sapphire substrate was annealed to remove any residual impurities on the surface in a H₂ ambient at 1120 °C for 10 min. A nominal 25 nm thick AlN nucleation layer was deposited at 650°C. The substrate temperature was then raised to 1120°C to grow a 0.8 μm Al_{0.11}Ga_{0.89}N layer. Other details growth conditions of AlGa_N films were described in Table 3-1. For μ-PL measurements, a He-Cd laser (Omnichrome 2074) operating at 325 nm was used for above bandgap excitation and was focused to a spot size of 1.5 μm by a microscope objective (100×, 0.5 numerical aperture). The signals were collected by the same objective lens into a monochromator (ARC-500) with both the entrance and exit slits opened to about 50 μm so that the spectral resolution is about 0.2 nm.

Table 3-1: *The detail growth conditions of AlGa_N films.*

	Time (min)	Temperature (°C)	Pressure (mbar)	NH ₃ (mol/min)	TMGa (mol/min)	TMAI (mol/min)
Desorption	10	1120	200	-	-	-
Nucleation	3	650	100	8.93×10 ⁻²	-	3.05×10 ⁻⁵
Annealing	1	1120	50	8.93×10 ⁻²	-	-
AlGa _N	60	1120	50	8.93×10 ⁻²	4.42×10 ⁻⁵	6.98×10 ⁻⁶

3-2 Microstructure in AlGa_{0.11}N Films

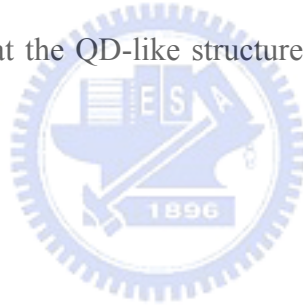
Optical examination of the Al_{0.11}Ga_{0.89}N layers revealed particular hillocks with a density of $1 \times 10^6 \text{ cm}^{-2}$ covering the substrate surface in Fig. 3-1. The base size of the hexagonal hillock is about 6 μm after 1 hour growth. From the three-dimensional (3D) atomic force microscopy (AFM) image (see inset), the hillock has the shape of a regular point-topped pyramid with a height about 200nm.

3-3 Micro-Photoluminescence (μ -PL) Spectra of AlGa_{0.11}N Hillock

A series of μ -PL spectra were taken at different locations along a dihedral direction across the hillock as shown in Fig. 3-2. The position label indicates the approximate distance from the hillock center. The spectra are dominated by the near-band-edge emission (I_{matrix}) at 341 nm as the probe spot is far away from the hillock. When it is focused on the hillock, the most significant change in the μ -PL spectra is the appearance of an extra peak (I_{H}) at 351 nm. Obviously, this strong and prominent emission is related only to the hillock. Note that, although the I_{nbe} is still present at 341 nm, it is so weak that is submerged in the strong and broad 351 nm band. Hoffmann et al. [8] reported that CL spectra showed the band-gap gradient from the base to the top of the selective growth GaN pyramids of 5 μm width and 10 μm height. In his report, the emission peak is 355.6 nm at the top of the pyramid and strongly red-shifted to 360.6 nm at the pyramid base. The different emission energies reveal the gradual relaxation of strain along the pyramid. However, no peak shift of I_{H} from the hillock edge to the center was observed in our study. Thus, it suggested that the stress was considerably small in AlGa_{0.11}N hillock which has a rather flat top region

in contrast to the steep pyramid.

The spatial μ -PL intensity and full-width-half-maximum (FWHM) distribution of the I_{matrix} (341 nm) and I_{H} (351 nm) are shown in Figs. 3-3 and 3-4, respectively. The I_{H} intensity at the hillock center is about five times larger than the I_{matrix} intensity far away from the hillock. We noticed that the FWHM of I_{matrix} obtained far away from the hillock is ~ 77 meV that is close to the report of Kim et al. [9] Moreover, the FWHM of I_{H} decreased from ~ 76 meV at the hillock edge to ~ 53 meV at the hillock center. The high intensity and narrow FWHM of I_{H} indicated that the hillock structure is an efficient emission center. From the 3D AFM image, a nipple structure appeared on the top of the AlGaIn hillock (see the inset of Fig. 1a). Since the quantum dot (QD)-like structure was observed on the top of AlGaIn/GaN selectively grown pyramid [10], it suggested that the QD-like structure is likely formed on the hillock top.



3-4 Temperature Dependent of μ -PL Spectra of AlGaN Hillock

To further examine optical properties of the AlGaN hillock, we also carried out temperature dependent μ -PL measurements from 10K to 300K as shown in Fig. 3-5. One clearly sees that the I_{matrix} photon energy not only decreases but also increases with temperature and forms a “S-shape” curve; so does the I_{H} . It was known that the “S-shape” is due to localization phenomena induced by alloy inhomogeneous in the AlGaN films [11]. From the Arrhenius plot for the luminescence intensity decrease of the donor bound exciton (D^0, X) of GaN film with increasing temperature [12]. The thermal dissociation of donor bound excitons involve two activation energies, namely the localization energy and donor binding energy. At low temperature, the free excitons tend to localize at the neutral donors (localization energy). However, at elevated temperature there is an interplay between the localization and ionization of neutral donor to reduce the number of available neutral donors. In contract, one activation energy was estimated from the PL emission intensity as a function of temperature of AlGaN films [11]. It was indicated that this activation energy implies impurity binding energies or carrier/exciton localization energies. Moreover, Cho et al. [13] also indicated that an activation energy estimated from the relationship $I(T)=I(0)/[1+A \exp(-E_a/kT)]$ in the low transition temperature region corresponds to the magnitude of effective potential fluctuations due to alloy inhomogeneous. Therefore, in order to understand the localization phenomena in AlGaN hillocks, we also finished the Arrhenius plots of the integrated PL intensities over the temperature range of 10-300 K shown in Fig. 3-6. The following formula was used to fit our results,

$$\frac{I(0)}{I(T)} = 1 + C_1 \exp\left(-\frac{\Delta E_{a1}}{kT}\right) + C_2 \exp\left(-\frac{\Delta E_{a2}}{kT}\right) \quad (3-1)$$

where ΔE_{a1} is the donor binding energy, ΔE_{a2} is the localization energy, C_1 and C_2 are fitting constant. From the slope, ΔE_{a1} is calculated to be 33.2 meV and ΔE_{a2} is 15meV for I_{matrix} , and ΔE_{a1} is 43.6 meV and ΔE_{a2} is 11.4 meV for I_{H} , respectively.

The temperature dependence of the emission energy is then shown in Fig. 3-7, for analyzing the localization energy. The expected temperature dependence (dashed lines) was calculated by using the Varshni's equation [14],

$$E_g = E_0 - \frac{\alpha T^2}{\beta + T} \quad (3-2)$$

with $\alpha=6.31 \times 10^{-4}$ eV/K and $\beta=2584$ K for I_{nbe} , and $\alpha=21.2 \times 10^{-4}$ eV/K, $\beta=606$ K for I_{H} .

The observed μ -PL temperature dependence follows Eq.(1) at high temperatures and deviates from it below a transition temperature T_c . The transition temperatures are 150 and 120 K for I_{matrix} and I_{H} , respectively, which are both higher than another report for the $\text{Al}_{0.11}\text{Ga}_{0.89}\text{N}$ films [9]. Nevertheless, the transition temperatures of 150 and 120 K are close to the localization energy of 15 and 11.4 meV. They reflect that the localization effect is strong in our sample.

Moreover, the transition temperature of I_{matrix} line was higher than that of the I_{H} line. The red-shift of the I_{matrix} (~ 35.8 meV) at low temperature relative to the dashed line is larger than that of I_{H} (~ 17.6 meV). It has been reported that the increase of transition temperature (T_C) and red-shift are due to the localization energy which increases with the Al content [9]. Our experimental results also support that the Al composition in the hillock is smaller than surrounding area in the $\text{Al}_{0.11}\text{Ga}_{0.89}\text{N}$ films. The recent x-ray energy dispersive spectroscopy observations (not shown) also confirm this. Thus, the hillock microstructure has lower Al composition than the regions free of hillocks in the AlGaN films.

3-5 Size Dependent of μ -PL Spectra of AlGaN Hillock

The OM images of different diameter of hillocks which ranges from 6 to 11 μ m are shown in Fig. 3-8. Their μ -PL spectra at the hillocks apex were shown in Fig. 3-9. It was observed that the μ -PL peak energy red-shifted from 3.537 eV to 3.509 eV as the diameter increased from 6 to 11 μ m. The Al composition estimated from μ -PL spectra for various diameter hillock is also shown in Fig. 3-10. The Al composition of AlGaN films was calculated as below:

From μ -PL spectra, the peak position can be converted into photon energy as : $E_g (eV) = 1240/\lambda(nm)$. By substituting it into the following empirical formula, one can obtain Al composition 'x':

$$E_g^{Al_xGa_{1-x}N}(x) = E_g^{GaN}(1-x) + E_g^{AlN}x - bx(1-x)$$

where the following constants were used for calculation.

$E_g^{GaN} = 3.42eV$, $E_g^{AlN} = 6.2eV$ and bowing parameter b is 1.3. We also shown the Al composition of 10 μ m hillock which measured from EDX. The result was agreed with the μ -PL measurement.

Since I_{nbe} peak energy is 3.625 eV around the hillock matrix region, the Al composition is ~11%. By increasing the hillock diameter from 6 μ m to 11 μ m, the red shift is from 88 meV to 116 meV. It was indicated that the Al composition decreases progressively while the hillock size increase. The Al composition variation is about ~2% in hillock.

3-6 Conclusions of AlGaN Hillock

In summary, we have measured the optical properties of hillocks in $\text{Al}_{0.11}\text{Ga}_{0.89}\text{N}$ film by using the μ -PL microscopy. The large intensity and narrow FWHM of I_{H} in the hillock structure indicated that it is a strong emission center. The temperature dependent μ -PL spectra showed that the I_{H} has the S-shape behavior with a transition temperature of 120 K reflecting the strong localization in the hillock. The lower transition temperature and smaller red-shift of I_{H} than that of I_{matrix} suggest that the Al composition is lower in hillock than in other parts of AlGaN film. Moreover, by increasing the hillock diameter from 6 μm to 11 μm , the red shift is from 88 meV to 116 meV. It was indicated that the Al composition decreases progressively while the hillock size increase. The Al composition variation is about $\sim 2\%$ in hillock.



References

- [1] S. Makamura, M. Senoh, S. Nagahama, N. Iwasa, T. Yamada, T. Matsushita, Y. Sugimoto, and H. Kiyoku, *Appl. Phys. Lett.* 69, 4056 (1996).
- [2] M. Asif Khan, X. Hu, A. Tarakij, G. Simin, J. Yang, R. Gaska, and M. S. Shur, *Appl. Phys. Lett.* 77, 1339 (2000).
- [3] E. Monroy, M. Hamilton, D. Walker, P. Kung, F. J. Sánchez, and M. Razeghi, *Appl. Phys. Lett.* 74, 1171 (1999).
- [4] L. Chang, S. K. Lai, F. R. Chen, and J. J. Kai, *Appl. Phys. Lett.* 79, 928 (2001).
- [5] B. Pécz, Zs. Makkai, M. A. di Forte-Poisson, F. Huet, and R. E. Dunin-Borkowski, *Appl. Phys. Lett.* 78, 1529 (2001).
- [6] F. A. Ponce, D. P. Bour, W. Götz, and P. J. Wright, *Appl. Phys. Lett.* 68, 57 (1996).
- [7] A. Y. Polyakov, A. V. Govorkov, N. B. Smirnov, M. G. Miuvidskw, J. M. Redwing, M. Shin, M. Skowronski, and D. W. Greve, *solid state Electron.* 42, 637 (1998).
- [8] A. Hoffmann, H. Siegle, A. Kaschner, L. Eckey, C. Thomsen, J. Christen, F. Bertram, M. Schmidt, K. Hiramatsu, S. Kitamura, and N. Sawaki, *J. Cryst. Growth* 189/190, 630 (1998).
- [9] H. S. Kim, R. A. Mair, J. Li, J. Y. Lin, and H. X. Jiang, *Appl. Phys. Lett.* 76, 1252 (2000).
- [10] K. Tachibana, T. Someya, S. Ishida, Y. Arakawa, *J. Cryst. Growth* 237, 1312 (2002).
- [11] J. Li, K. B. Nam, J. Y. Lin, and H. X. Jiang, *Appl. Phys. Lett.* 79, 3245 (2001).
- [12] K. O'Donnell et al., in *Group III Nitride Semiconductor Compounds: Physics and Applications*, edited by B. Gil (Clarendon Pr, New Zealand, 1998), pp. 247-248.
- [13] Yong-Hoon Cho, G. H. Gainer, J. B. Lam, J. J. Song, W. Yang, and W. Jhe, A. Bimberg and M. Sondergeld, *Phys. Rev. B* 61, 7203 (2000).
- [14] B. Monemar, *Phys. Rev. B* 10, 676 (1974).

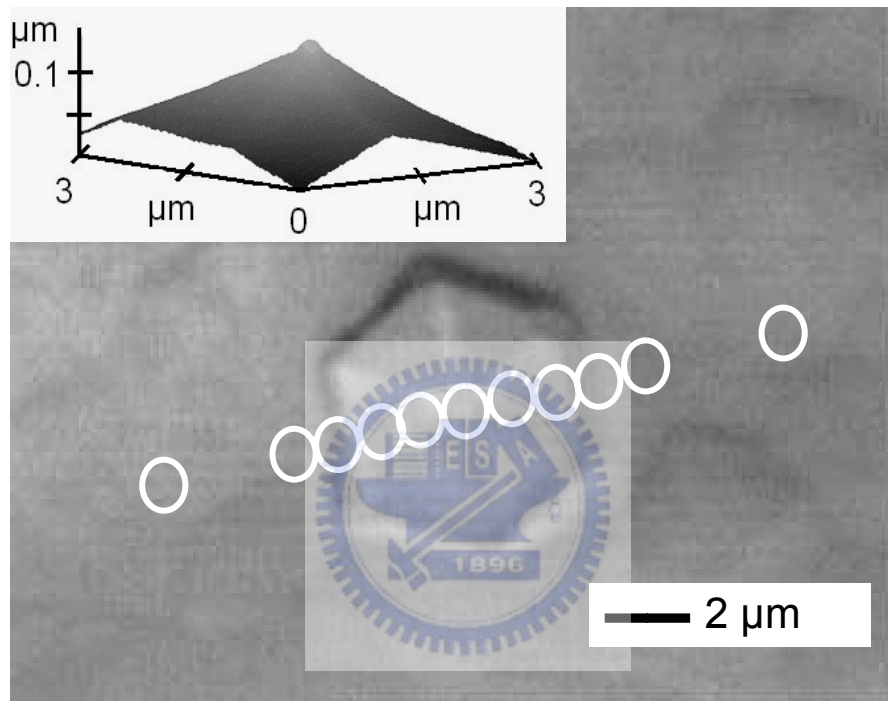


Fig. 3-1 The optical microscope (OM) image of hillock in AlGaIn films. The inset shows the 3D AFM images of hillock.

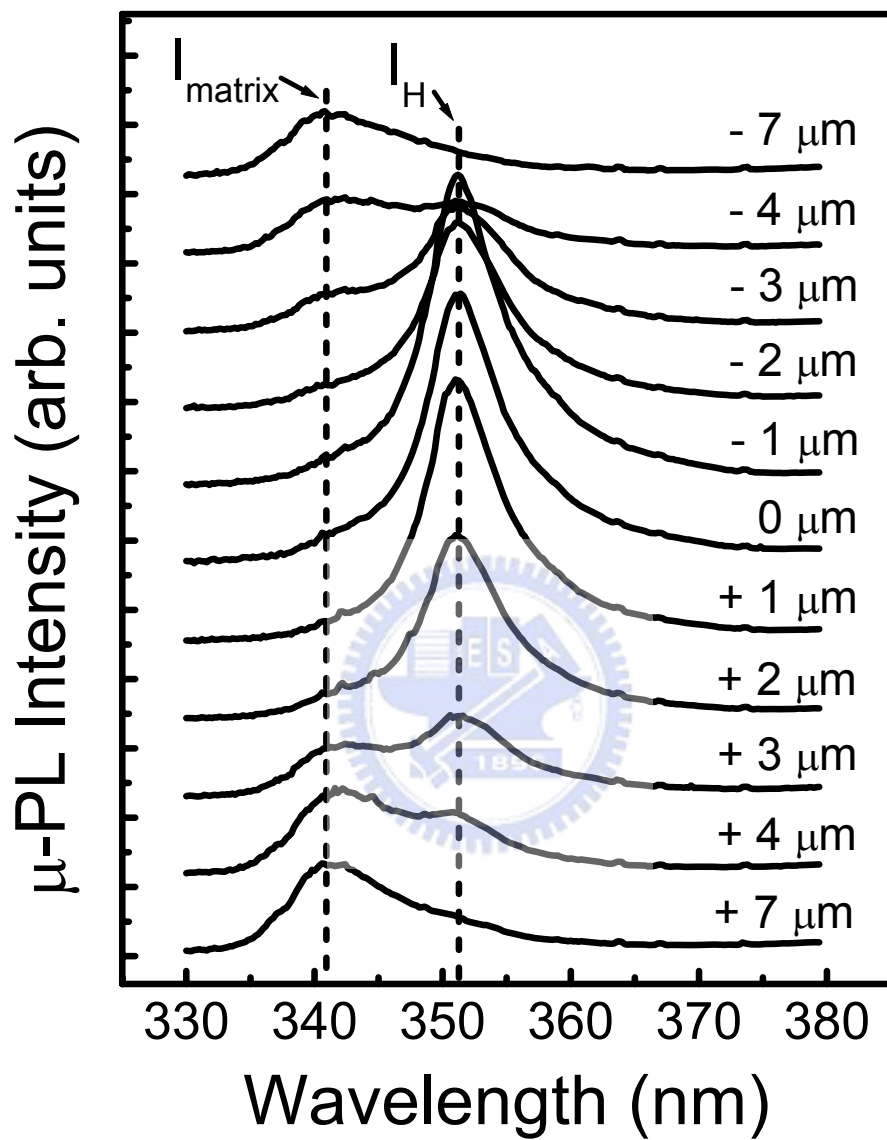


Fig. 3-2 The room temperature μ -PL spectra taken at different locations on OM image.

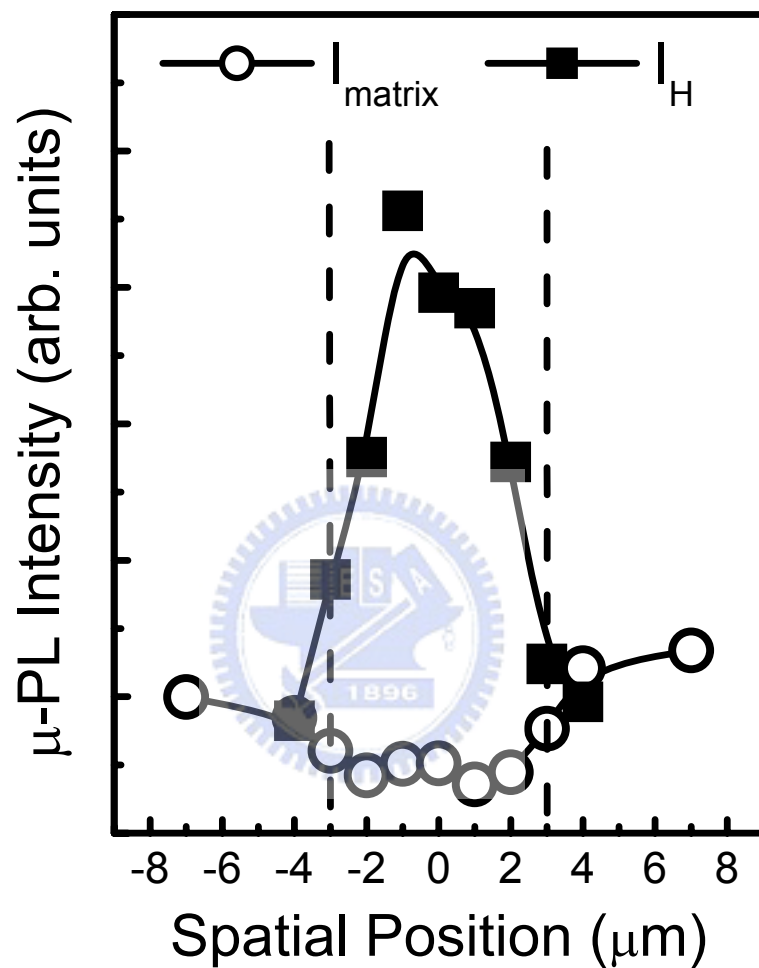


Fig. 3-3 The spatial μ -PL intensity distribution of I_{matrix} and I_{H} .

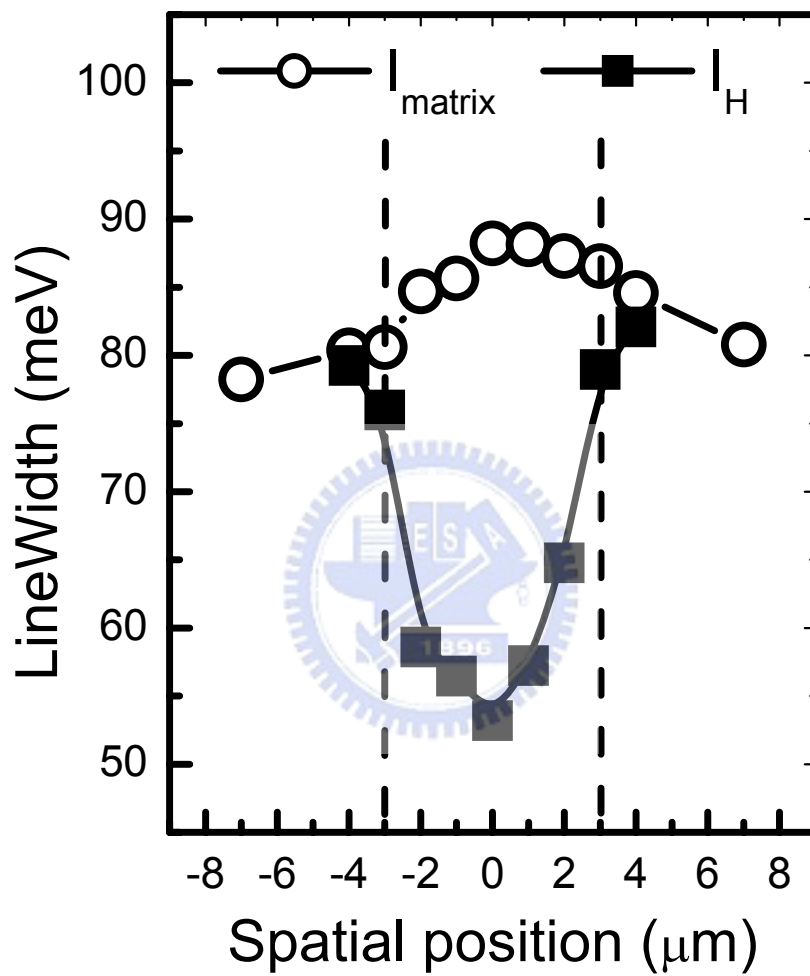


Fig. 3-4 The spatial μ -PL full-width-half-maximum (FWHM) distribution of I_{matrix} and I_{H} .

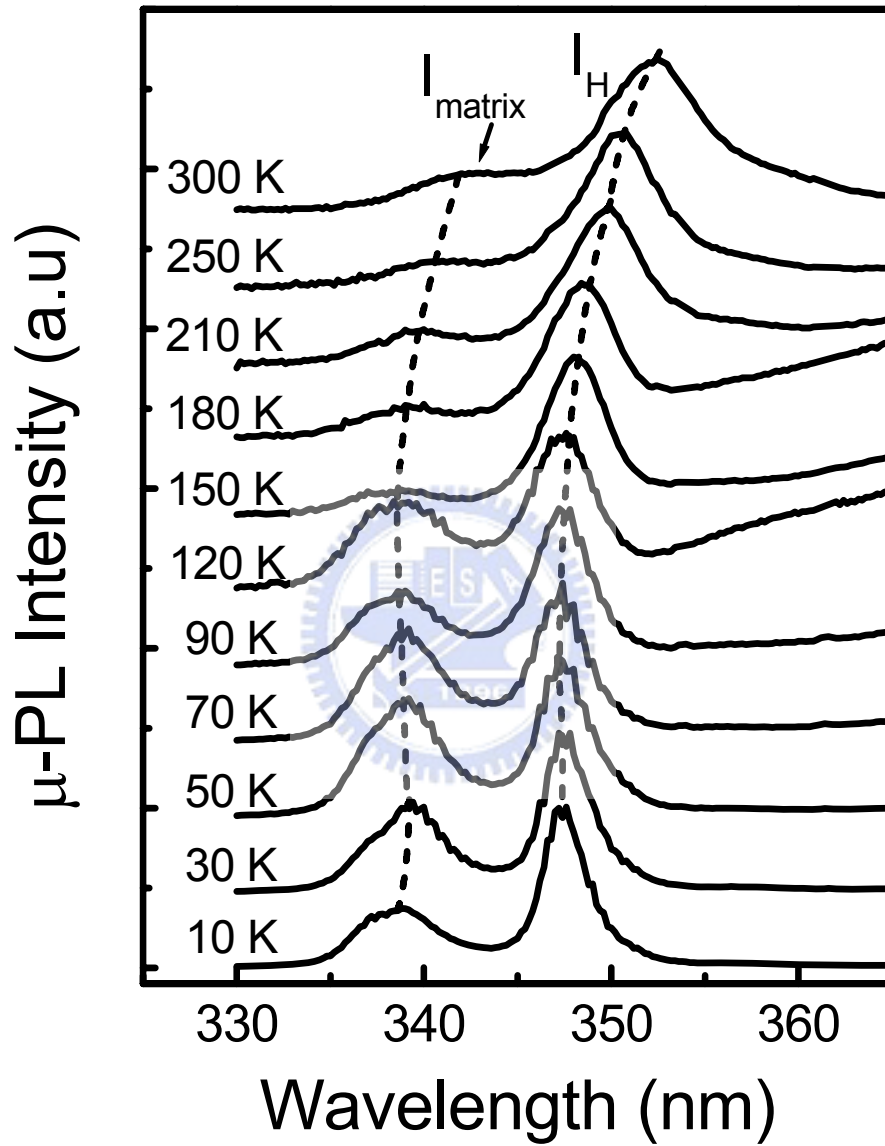


Fig. 3-5 Temperature dependent μ -PL measurements of AlGaIn hillock from 10 to 300K.

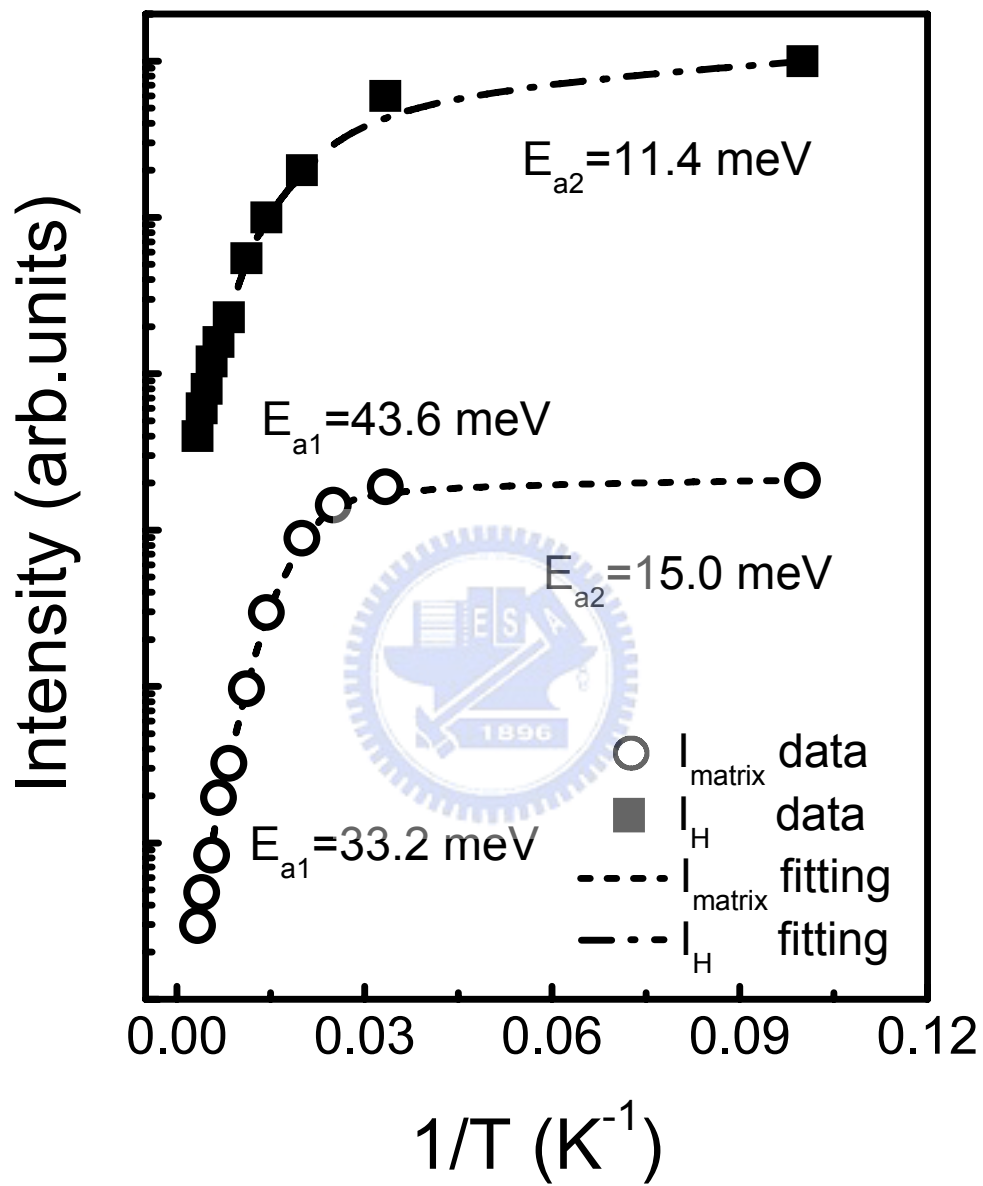


Fig. 3-6 Integrated PL intensity as a function of temperature for I_{matrix} and I_{H} .

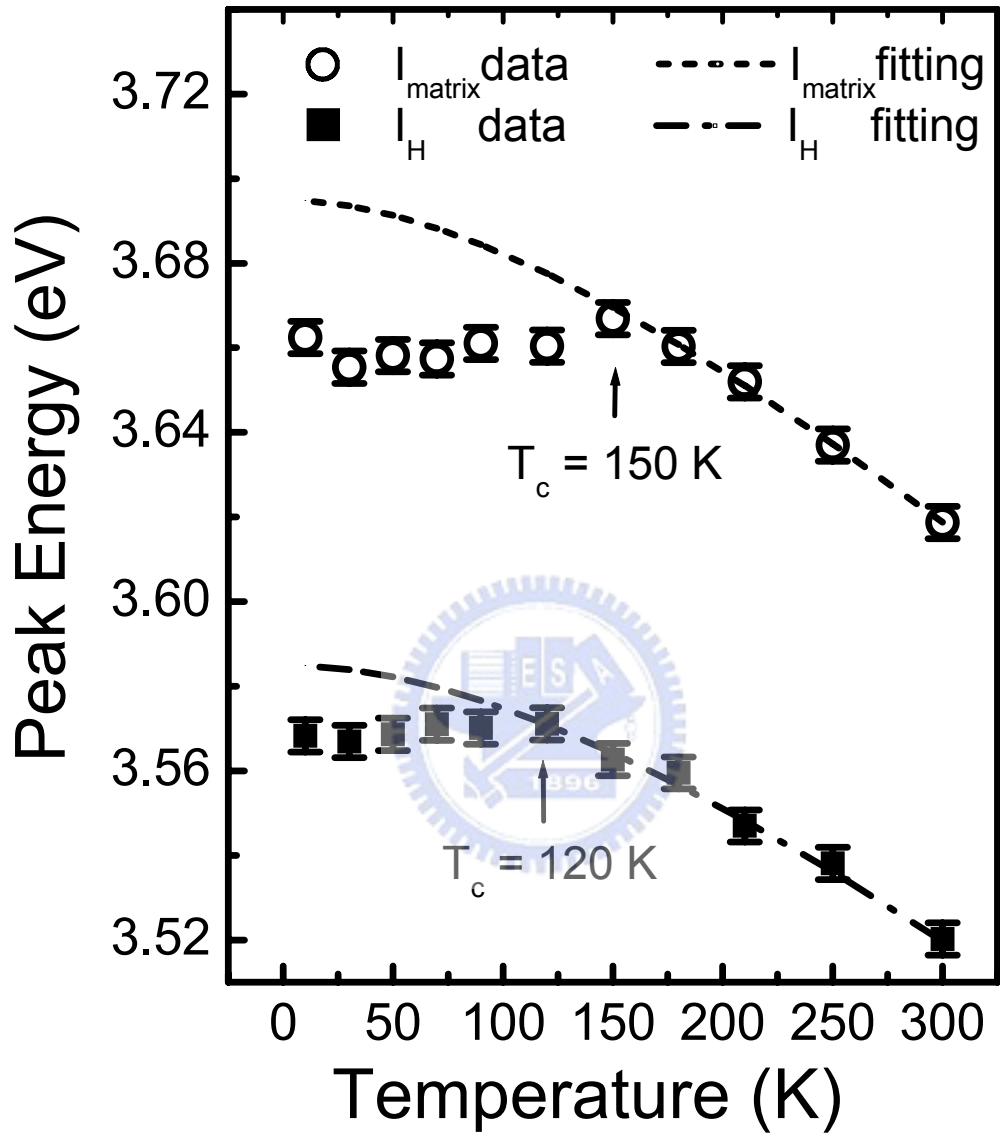


Fig. 3-7 Temperature dependence of the emission peak of I_{matrix} and I_H . Arrows indicate the transition temperature T_c .

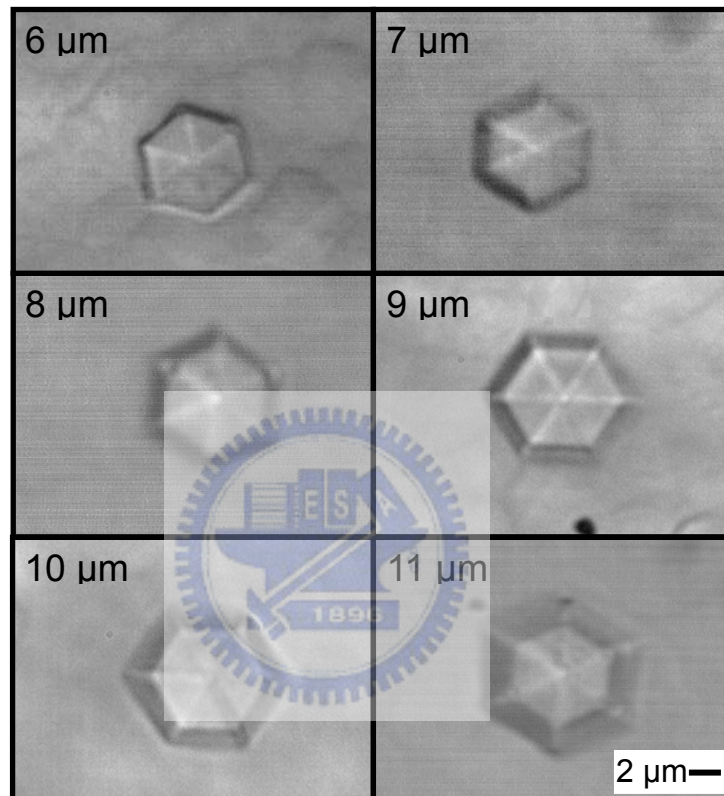


Fig. 3-8 The optical microscope (OM) image of the different size hillock in AlGaIn films.

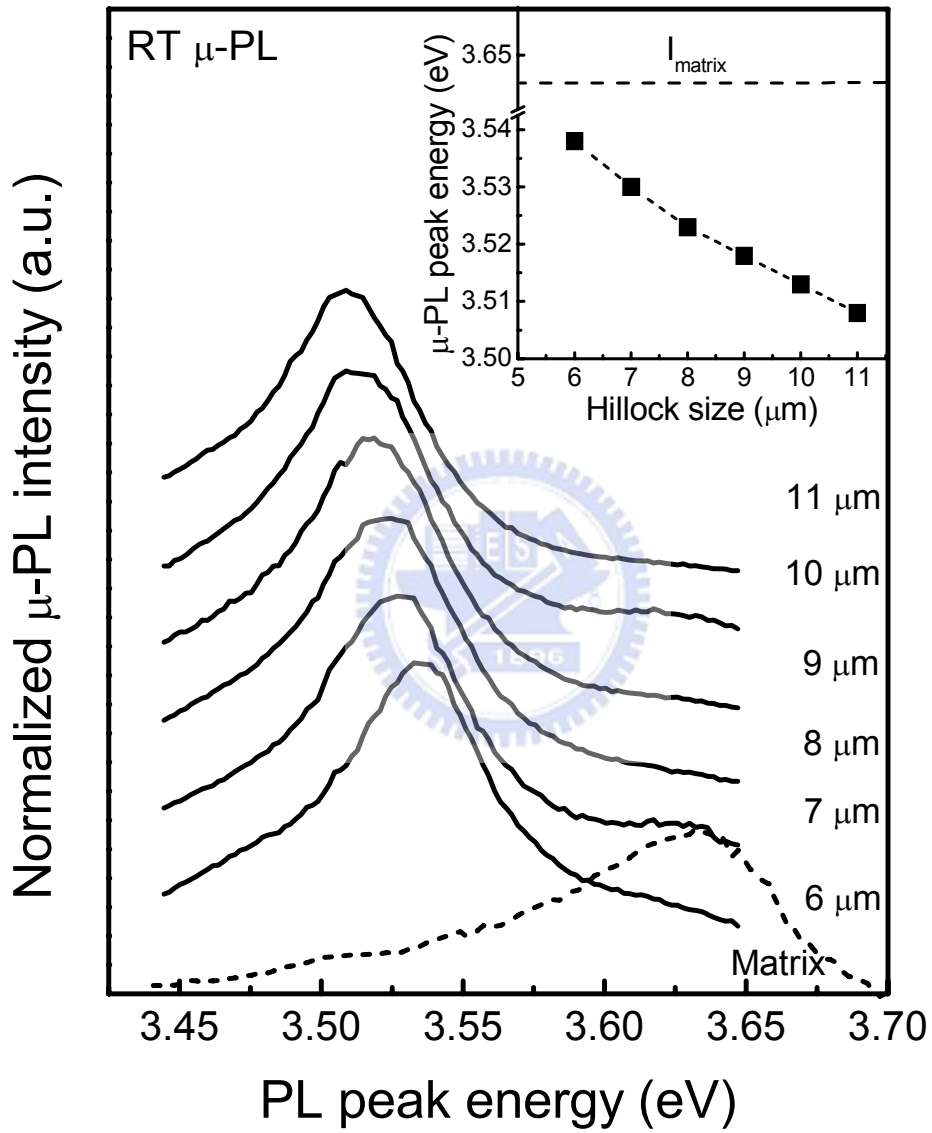


Fig. 3-9 The room temperature μ -PL spectra taken from different size of hillock.

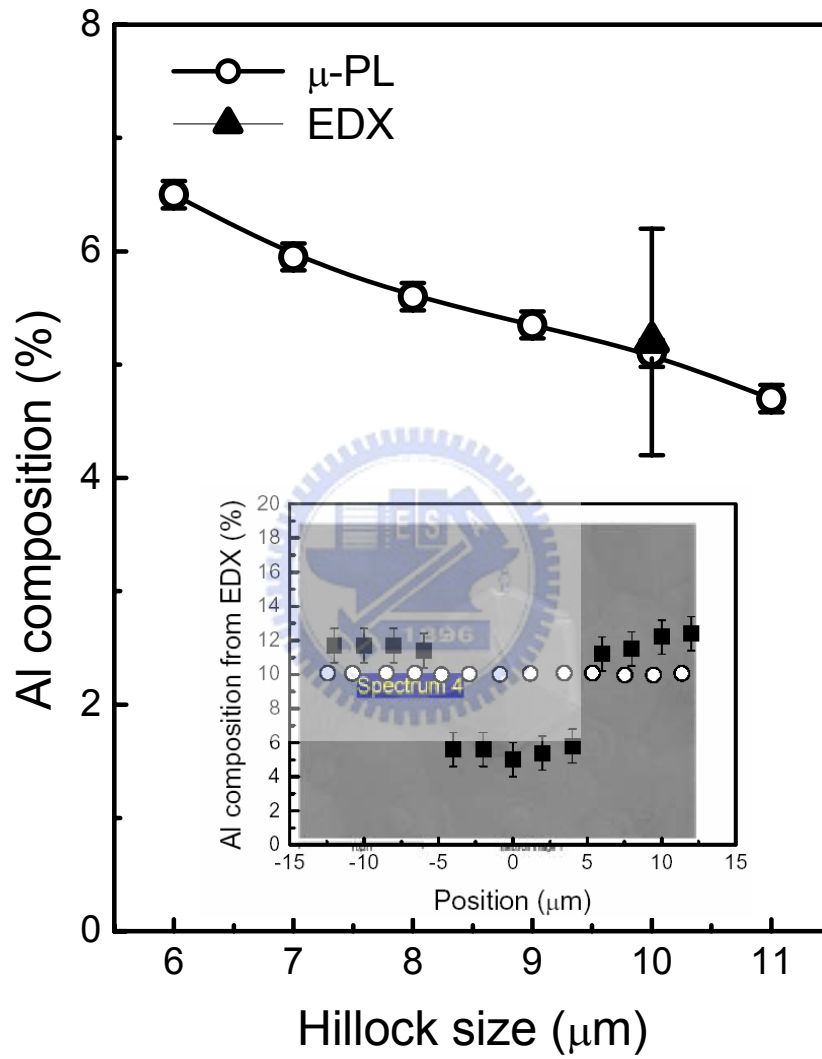


Fig. 3-10 The relation between Al composition and hillock size.

Chapter 4 GaN Nanodots Growth

Because of the lack of lattice-matched substrates, the growths of GaN, InGaN and AlGaN materials on sapphire substrates are known to contain numerous defects, such as threading dislocations, stacking faults and inversion domain boundary in the epilayer, accompanied generally by a high concentration of nonradiative recombination centers. The existence of such defects seems not to affect significantly the efficiency of band-edge luminescence in InGaN/GaN blue/green light-emitting diodes. It is ascribed to the formation of self-assembled In-rich islands during InGaN film growth, which form dotlike states and lead to a marked gain enhancement in their optical process [1]. However, this is not the case for ultraviolet AlGaN materials. To date, no evidence has shown that Al segregation exists. Even though Al-rich nanoislands indeed occur, because of their higher band-gap energy feature, it would not improve the carrier confinement and hence luminescence efficiency in AlGaN films. From published reports on AlGaN ternary [2,3], we consider that the presence of a high concentration of threading dislocations and the absence of self-assembled lower energy dotlike structures are the two most detrimental factors that cause the poor quantum efficiency of AlGaN-based UV-light-emitting devices. Thus, the successful fabrication of GaN or AlGaN dotlike structures operating in the ultraviolet range is an essential step for the implementation of high-brightness UV-LEDs.

Despite the numerous studies on InGaN dots, the published reports on GaN dots, particularly on specific sample preparation procedure, are still quite limited. The growth of GaN dots on AlN using the commonly used Stranski-Krastanow (S-K) growth mode was not reported until 1997 by Daudin *et al.*[4] using molecular beam epitaxy (MBE), and more recently by Miyamura *et al.* [5] using metalorganic vapor phase epitaxy (MOVPE) by maximizing the advantages of the driving force induced

by the lattice mismatch between GaN and AlN. Probably because of the insufficient lattice mismatch provided by the underlying layer, very few updated reports have been published recently on the GaN island growth on AlGaIn ternary. That imposes a strict restriction for its practical use in UV-light-emitting devices. To overcome this problem, an interesting approach, called antisurfactant method, has been used to grow GaN dots on AlGaIn ternary [6]. By supplying a small amount of Si antisurfactants on an $\text{Al}_x\text{Ga}_{1-x}\text{N}$ surface, the GaN growth is found to change from the step-flow growth feature to the three-dimensional island growth, resulting in the formation of nanoscale GaN dot structures on the AlGaIn surface. In this letter, we present another feasible method for preparing GaN dots on the AlGaIn surface. Preliminary results indicate that by alternating the source precursors during the MOVPE epitaxial growth, a dotlike GaN structure can be obtained on an $\text{Al}_{0.11}\text{Ga}_{0.89}\text{N}$ epilayer. This method is proved to be a simple and yet effective way for preparing dotlike structures in the GaN material system and may find potential use in fabricating the ultraviolet GaN-based light-emitting devices.

4-1 experimental details

In this study, the uncapped GaN dots were grown on Al_{0.11}Ga_{0.89}N/sapphire (0001) substrates by AIX 200/4 RF-S horizontal-reactor MOVPE system. The substrate temperature is measured by inserting the S-type thermal couple into a susceptor, which has a deviation of approximately $\pm 2^\circ\text{C}$. Trimethylgallium (TMGa), trimethylaluminum (TMAI), and ammonia (NH₃) were used as the source precursors of Ga, Al, and N, respectively. Hydrogen was used as a carrier gas. Prior to material growth, the sapphire substrate was annealed to remove any residual impurities on the surface in a H₂ ambient at 1120 °C for 10 min. A nominal 25-nm-thick AlN nucleation layer was deposited at 650 °C. The substrate temperature was then increased to 1120°C to grow a 0.5 μm Al_{0.11}Ga_{0.89}N layer. The GaN dots were deposited at temperatures ranging from 840 to 960°C by flow-rate modulation epitaxy (FME) technique. The gas flow sequence for FME, basically consists of four steps: 20 s Ga source step, 10 s NH₃ source step and intervening 5 s purge steps in between. To suppress such reevaporation, we intended to introduce a 1/10 nominal flow rate of NH₃ during the entire FME growth cycle except the N step, where full NH₃ flux (1.79×10^5 $\mu\text{mol}/\text{min}$) was used. Such arrangement can conceivably suppress, if any, the re-evaporation of N atoms to a minimum extent. After the dot growth, the substrate temperature was then decreased to room temperature under a continuous flush of NH₃ gas. The other detail growth conditions were described in Table 4-1.

The theory of the periodic flow-rate modulation epitaxy growth according to this study is shown in Fig. 4-1. First, substrate 1 is provided (Fig. 4-1(a)), and buffer layer 2 is grown on the substrate (Fig. 4-1(b)). Purge gas 3 is turned on and the first reactant 4 is modulated to a range below the first molar flow rate (Fig. 4-1(c)), so that

the second reactant 5 turned on thereafter forms metal or metal-rich compound islands 6 on the buffer layer (Fig. 4-1(d)). After the formation of said island, purge gas is turned on to clean remaining second reactant which does not form islands (Fig. 4-1(e)). Subsequently, the first reactant 4 is modulated to a range above the second molar flow rate (Fig. 4-1(f)), so that said islands form high quality nanoparticles 7 with excellent structure under sufficient first reactant molar flow rate, and a growth cycle is completed. The geometric shape and size can be controlled through modulating the first and second reactant molar flow rates and the turn-on time.

The time chart of reactant precursor flow sequence is shown in Fig. 4-2. In the first purge step (as shown in Fig. 4-2(a)), purge gas (hydrogen 3) was turned on to clean remaining excess NH_3 reactant, and NH_3 reactant 4 was modulated to the lower first molar flow rate range (1.79×10^{-2} mole/min), so that TMGa reactant turned on in next step was able to grow metal gallium or Ga-rich islands on $\text{Al}_{0.11}\text{Ga}_{0.89}\text{N}$ buffer layer below the first molar flow rate without the formation of 2D grown GaN film. Further, NH_3 reactant was modulated to the lower first molar flow rate to avoid re-evaporation of nitrogen atoms on the surface of $\text{Al}_{0.11}\text{Ga}_{0.89}\text{N}$ buffer layer in low grown temperature environment of 900°C , and the nitrogen vacancy defect on the surface of $\text{Al}_{0.11}\text{Ga}_{0.89}\text{N}$ buffer layer was reduced.

In TMGa reactant turn-on stage (as shown in Fig. 4-2(b)), TMGa reactant 5 was turned on with molar flow rate setting of 8.84×10^{-5} mole/min for 20 seconds, to form metal gallium or Ga-rich islands on $\text{Al}_{0.11}\text{Ga}_{0.89}\text{N}$ buffer layer. In the second purge stage (as shown in Fig. 4-2(c)), TMGa reactant was turned off, and purge gas 3 was turned on for 5 seconds to clean remaining TMGa reactant which did not form metal gallium or Ga-rich islands. In NH_3 reactant turn-on stage (as shown in Fig. 4-2(d)), the molar flow rate of NH_3 reactant 4, which was modulated from below the first

molar flow rate to above the second molar flow rate (1.79×10^{-1} mole/min), was turned on for 10 seconds, so that islands formed GaN nanoparticles 7 with excellent quality at sufficient NH_3 reactant molar flow rate.

Table 4-1: *The growth conditions of GaN dots on AlGaIn films.*

	Time (min)	Temperature (°C)	Pressure (mbar)	NH_3 (mol/min)	TMGa (mol/min)	TMAI (mol/min)
Desorption	10	1120	200	-	-	-
Nucleation	3	650	100	8.93×10^{-2}	-	3.05×10^{-5}
Annealing	1	1120	50	8.93×10^{-2}	-	-
AlGaIn	60	1120	50	8.93×10^{-2}	4.42×10^{-5}	6.98×10^{-6}
GaN dots (Ga step)	20 (sec)	900	200	1.79×10^{-2}	8.84×10^{-5}	-
Purge	10 (sec)	900	200	1.79×10^{-2} - 1.79×10^{-1}	-	-
GaN dots (NH_3 step)	20 (sec)	900	200	1.79×10^{-1}	-	-
Purge	10 (sec)	900	200	1.79×10^{-1} - 1.79×10^{-2}	-	-

4-2 Growth Temperature Effect

With regard to GaN growth, Stephenson *et al.*[7] reported that the typical GaN growth on a nearly lattice-matched substrate by conventional MOVPE undergoes mainly three different growth modes with increasing substrate temperature, namely, three-dimensional (3D) island growth, two-dimensional (2D) layer-by-layer growth, and one-dimensional (1D) step-flow growth. The corresponding transition temperatures are approximately 800 and 1000°C, respectively. Since growth temperature is one of the critical parameters affecting the growth mode, to verify whether the FME technique is suitable for GaN dot growth, we conducted GaN growth on AlGa_N at 840, 870, 900, 930, 940 and 960°C with two FME growth cycles. The flow rates of TMGa and NH₃ during the source exposure steps were kept at 88.4 and 1.79×10^4 μmol/min, respectively. The resulting surface morphologies are shown in Fig. 1. Unlike the conventional MOVPE layer-by-layer 2D growth feature at the high-growth-temperature region (>800°C), by employing FME, we do observe that GaN dots can be formed on the slightly lattice-mismatched Al_{0.11}Ga_{0.89}N epilayer in the temperature range from 840 to 940°C.

Dot density as a function of reciprocal temperature is shown in the inset of Fig. 2. As anticipated, the dot density is very sensitive to the substrate temperature. There are two distinct regions in our dot density curve, divided by a temperature of ~915°C. As can be seen in the figure, the density decreases gradually from 1.7×10^9 to 3×10^8 cm⁻² as the temperature is increased from 840 to 900°C, which then tends to drop sharply with further increasing temperature, and eventually becomes zero, *i.e.*, no dot growth, if the substrate temperature is beyond 960°C. From the island nucleation mechanism proposed by Robinson and Robins *et al.*[8], we learn that the dot density

at low growth temperatures is governed by the diffusion capability of the adatom, while that at high temperatures is determined predominately by the re-evaporation rate of adatoms, hence the binding energy of the adatom to the adsorbed site. The respective characteristic equations are

$$N_s = N_{0L} \exp(E_d / 3kT) \quad \text{for low temperature, and} \quad (1)$$

$$N_s = N_{0H} \exp(E_a / 2kT) \quad \text{for high temperature,} \quad (2)$$

where N_s is dot density, N_{0L} and N_{0H} pre-exponential parameters, E_d activation energy of diffusing Ga adatom, and E_a binding energy of Ga adatom to the adsorbed sites. The calculated E_d and E_a for the Ga adatom are $\sim 0.64\text{eV}$ and $\sim 1.20\text{eV}$, respectively, for GaN growth on AlGaIn film by FME, which are considerably smaller than the simulated value of $E_d = 1.8\text{ eV}$ [9] and the experimental value of $E_a = 2.2\text{ eV}$ obtained by the conventional MBE growth system, [10] and the value of $E_a = 3.0\text{ eV}$ by the conventional MOCVD system [7]. Our result is also similar to the case of GaAs growth in which the activation energy during the FME growth is smaller than that during the conventional MOCVD growth [11]. It was also noted that the smaller E_a of 0.4 eV was reported in the GSMBE system [12].

Aside from the dot density, the other dot parameters that concern us are height and diameter. One can find in Fig. 2 that by using FME, the GaN dot diameter tends to increase slowly with increasing temperature and increases marked as the growth temperature exceeds the dividing temperature of 915°C . In contrast, the dot height almost remains constant of 30nm at low temperatures, becomes reduced with further increasing the growth temperature and vanishes completely at temperatures above 960°C . The observation extremely large dot diameter, concurrently with essentially zero height for $T > 960^\circ\text{C}$, indicates that the growth manner for FME-GaN on AlGaIn

starts to transform from 3D to 2D growth mode at $\sim 960^\circ\text{C}$. That is, by using FME, we can extend the upper limit of the growth temperature for GaN island growth from $\sim 800^\circ\text{C}$ in the conventional MOVPE to 960°C . Since a higher growth temperature usually yields a better film quality, this will make the FME a very promising method for preparing nanodot structures.

4-3 Size Control

For light-emitting devices, the size of low-band-gap dot structure used in the active layer is a matter related to the device luminescence efficiency. The use of a smaller dot structure will certainly result in a better carrier confinement, and even provoke quantum excitonic effects to improve the quantum efficiency. For this reason, we thus performed another series of GaN dot growth on $\text{Al}_{0.11}\text{Ga}_{0.89}\text{N}$ at 900°C by decreasing the TMGa exposure time in FME, with all the other growth parameters kept the same. Figure 3 shows the atomic force microscopy (AFM) images for films grown at different TMGa exposure times of 20, 15, 10, 7, 5 and 0 s per cycle. The resulting variation of GaN dot height and diameter are shown in Fig. 4. The average dot diameter and height are clearly decreased as the Ga exposure time is decreased. By decreasing the Ga exposure time to 5 s, we are able to attain a GaN dot structure with a height of 5 nm; a strong quantum effect is expected to dominate the light transition.

4-4 Growth Mode

Based on the growth theory, there are two growth modes responsible for the self-organized island growth, namely, Stranski-Krastanow and Volmer-Weber (V-W) growth modes [13,14]. Regardless of which growth mode, the sum of the surface free energy of the deposited film (σ_{film}) and the interface strain energy ($\sigma_{\text{interface}}$), including interface energy (σ_{if}) due to lattice mismatch between substrate and deposited film, and strain energy ($\sigma_{\text{st}}(t)$) due to induced strain caused by the wetting layer, has to be greater than the surface free energy of the substrate ($\sigma_{\text{substrate}}$); otherwise, the layer-by-layer growth manner will occur during deposition. The primary difference between these two island growth modes is the thickness of the wetting layer. If the required wetting layer thickness for producing island growth is greater than one lattice layer, the associated island growth mode is categorized into the S-K growth mode; if not, then the V-W mode.

If the SK mode is the case for our FME GaN dot structure grown on $\text{Al}_{0.11}\text{Ga}_{0.89}\text{N}$, the critical thickness of the GaN wetting layer should be at least of 330\AA [15] to accumulate sufficient strain energy to induce island growth. This seems unlikely to happen in our study, because such a thickness can never be achieved with the same growth time and source supplies under our nominal MOVPE growth method, not to mention the FME method, where the growth rate is considered to be lower due to the high desorption nature of the reactants.

Thus, we consider that our FME GaN dot growth on $\text{Al}_{0.11}\text{Ga}_{0.89}\text{N}$ is via the Volmer-Weber growth mode. The explanation for this is as follows. It is known that the V-W island growth will proceed if the surface free energy of the substrate ($\sigma_{\text{substrate}}$) is less than the sum of the surface free energy of the depositing film (σ_{film}) and the

interface strain energy ($\sigma_{\text{interface}}$).

$$\sigma_{\text{substrate}} < \sigma_{\text{film}} + \sigma_{\text{interface}} \quad (3)$$

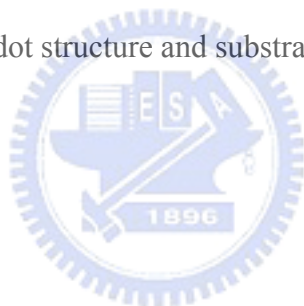
Because of the special alternating gas supply feature in FME, during the Ga source step, it is the Ga metal, not the GaN, that is deposited on the underlying AlGa_{0.11}N layer, which will be converted lately into GaN film during the following NH₃ source step. The surface free energies of Al_{0.11}Ga_{0.89}N and Ga metal [16] are ~107 and 45 meV/Å², respectively. To meet the V-W island growth constraint, it would need at least an additional ~62 meV/Å². Since the interface strain energy includes an interface energy and a strain energy of one lattice layer, [17]

$$\sigma_{\text{interface}} = \sigma_{\text{AlGa}_0.11\text{N}} \left(1 - \frac{1}{(\frac{\Delta a}{a}) + 1} \right) + \frac{1}{2} Y (\varepsilon_a)^2 t, \quad (4)$$

where the first term is interface energy ($\sigma_{\alpha\text{-Ga}/\text{AlGa}_0.11\text{N}}$) and the second term is strain energy $\sigma_{\text{st}}(t)$, Y is modulus of Ga metal (5.69×10^{10} N/m²) [18], ε_a in-plane strain ($a_{\alpha\text{-Ga}} - a_{\text{AlGa}_0.11\text{N}} / a_{\text{AlGa}_0.11\text{N}}$), t the thickness of one lattice layer of Ga metal ($c_{\alpha\text{-Ga}} = 7.64$ Å, $a_{\alpha\text{-Ga}} = 4.51$ Å [19] and $a_{\text{AlGa}_0.11\text{N}} = 3.18$ Å). The calculated interface energy and strain energy of one lattice layer are 31.5 and 237 meV/Å², respectively. The resulting total interface strain energy is 268.5 meV/Å², which is far beyond the need for V-W island growth mode. Thus, we consider that this is the reason that accounts for the successful growth of the GaN dot on AlGa_{0.11}N in our study by FME method.

4-5 Conclusions of GaN Nanodots Growth

In summary, we have demonstrated that the GaN dots can be grown on a slightly lattice-mismatched $\text{Al}_{0.11}\text{Ga}_{0.89}\text{N}$ epilayer using flow-rate modulated epitaxy. The dot growth in this method is found to be controlled primarily by surface diffusion of adatoms at substrate temperatures below $\sim 915^\circ\text{C}$ and by desorption at higher temperatures. Because of the alternating gas supply nature in FME, we consider that the dot growth studied here is mainly via the Volmer-Weber growth mode, not through the Stranski-Krastanow growth mode. Our results indicate that the FME growth technique is a very promising tool for preparing self-organized quantum dot structures for most practical devices due to the release of requirement of large lattice mismatch between the grown dot structure and substrate.



References

- [1] H. K. Cho, J. Y. Lee, N. Sharma, C. J. Humphreys, G. M. Yang, C. S. Kim, J. H. Song and P. W. Yu: *Appl. Phys. Lett.* **79** (2001) 2594.
- [2] T. Akasaka, T. Nishida, Y. Taniyasu, M. Kasu, and T. Makimoto: *Appl. Phys. Lett.* **83** (2003) 4140.
- [3] S. Tanaka, Jeong-Sik Lee, Peter Ramvall and Hiroaki Okagawa: *Jpn. J. Appl. Phys.* **42** (2003) L885.
- [4] B. Daudin, F. Widmann, G. Feuillet, Y. Samson, M. Arlery, and J. L. Rouvière: *Phys. Rev.* **B56** (1997) 7069.
- [5] M. Miyamura, K. Tachibana, and Y. Arakawa: *Appl. Phys. Lett.* **80** (2002) 3937.
- [6] Satoru Tanaka, Sohachi Iwai, and Yoshinobu Aoyagi: *Appl. Phys. Lett.* **69** (1996) 4096.
- [7] G. B. Stephenson, J. A. Eastman, C. Thompson, O. Auciello, L. J. Thompson, A. Munkholm, P. Fini, S. P. Denbaars, and J. S. Speck: *Appl. Phys. Lett.* **74** (1999) 3326.
- [8] V. N. E. Robinson and J. L. Robins: *Thin Solid Films* **20** (1974) 155.
- [9] Tosja Zywiets, Jörg Neugebauer, and Matthias Scheffler: *Appl. Phys. Lett.* **73** (1998) 487.
- [10] S. Guha, N. A. Bojarczuk, and D. W. Kisker: *Appl. Phys. Lett.* **69** (1996) 2879.
- [11] Naoki Kobayashi, Toshiki Makimoto and Yoshiji Horikoshi: *Jpn. J. Appl. Phys.* **24** (1985) L962.
- [12] Keith R. Evans, Ting Lei and Charles R. Jones: *Solid-State Electron.* **41** (1997) 339.
- [13] D. J. Eaglesham and M. Cerullo: *Phys. Rev. Lett.* **64** (1990) 1943.
- [14] D. Winau, R. Koch, A. Führmann, and K. H. Rieder: *J. Appl. Phys.* **70** (1991)

3081.

[15] William G. Perry, M. B. Bremser, T. Zheleva, K. J. Linthicum and R. F. Davis:
Thin Solid Films **324** (1998) 107.

[16] L. Z. Mezey and J. Giber: Jpn. J. Appl. Phys. **21** (1982) 1569.

[17] Kazuo Nakajima, Toru Ujihara, Satoru Miyashita, and Gen Sazaki: J. Appl. Phys.
89 (2001) 146.

[18] K. Gschneidner, Jr.: Solid State Phys. **16** (1964) 275.

[19] X. G. Gong, Guido L. Chiarotti, M. Parrinello, and E. Tosatti: Phys. Rev. **B43**
(1991) 14277.



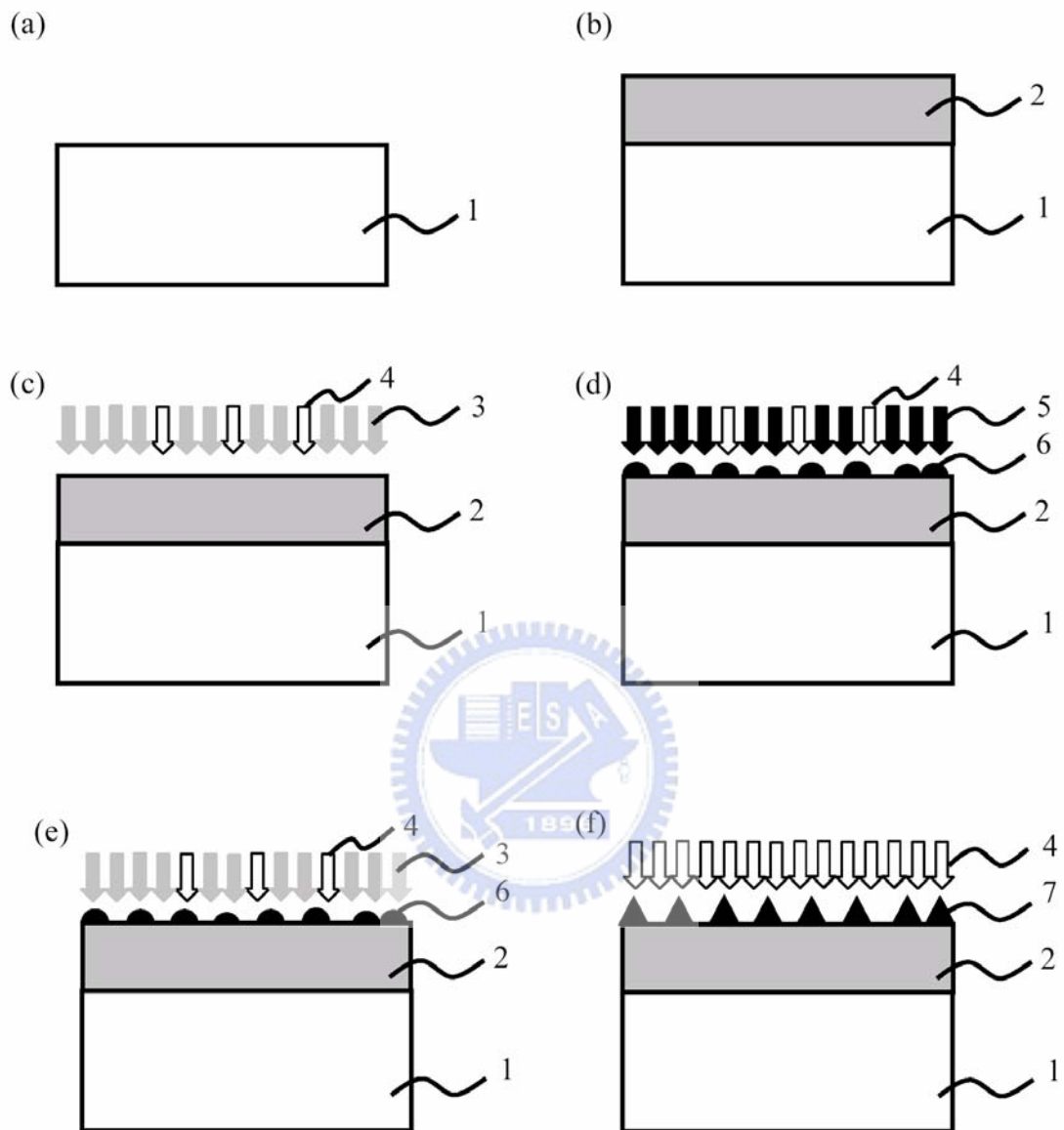


Fig. 4-1 A scheme showing the principle of the periodic flow-rate modulation epitaxy growth GaN dots on AlGaN films.

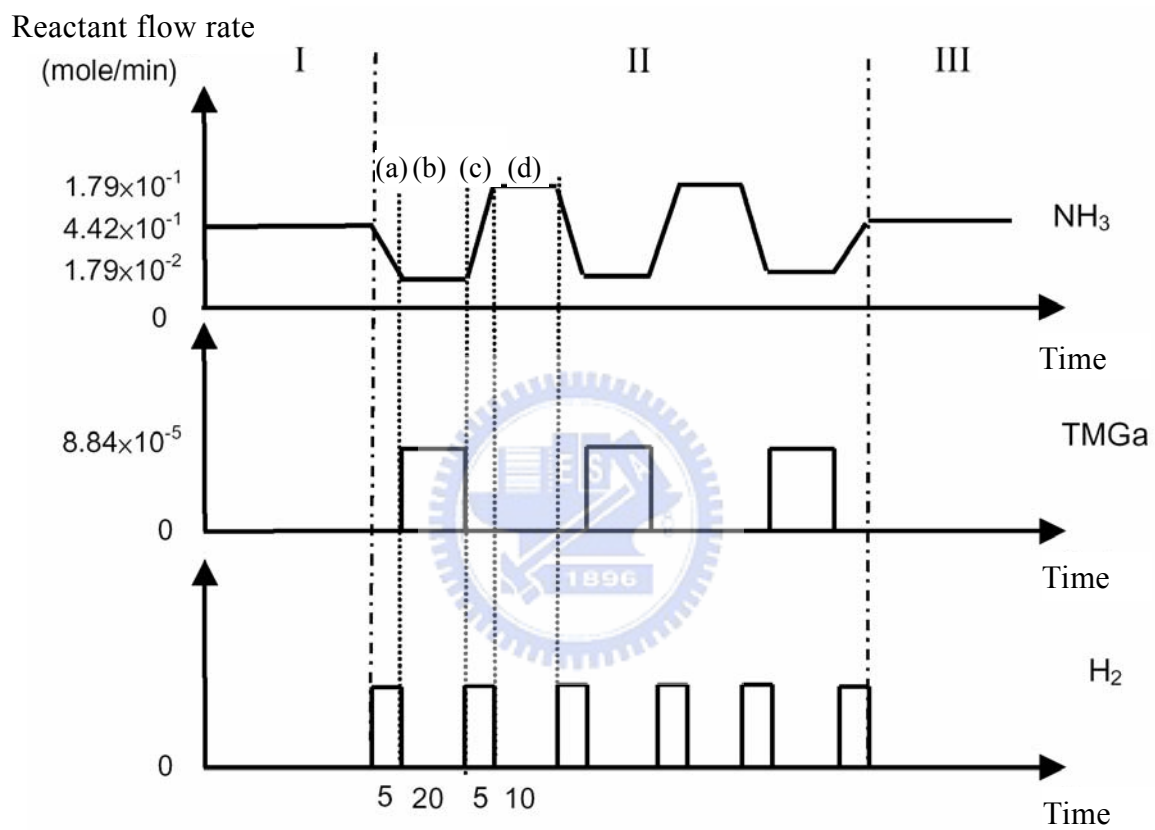


Fig. 4-2 A time chart showing the modulation of reactant molar flow rate in the periodic flow-rate modulation epitaxy.

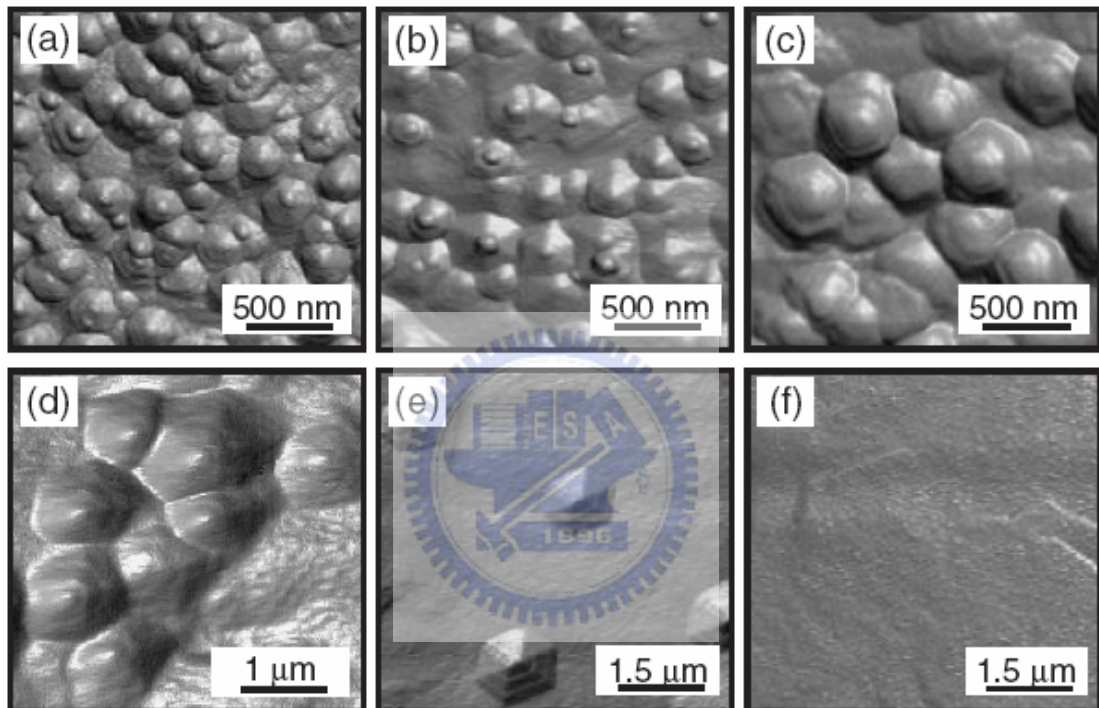


Fig. 4-3 AFM images of GaN dots grown at (a) 840, (b) 870, (c) 900, (d) 930, (e) 940 and (f) 960 °C.

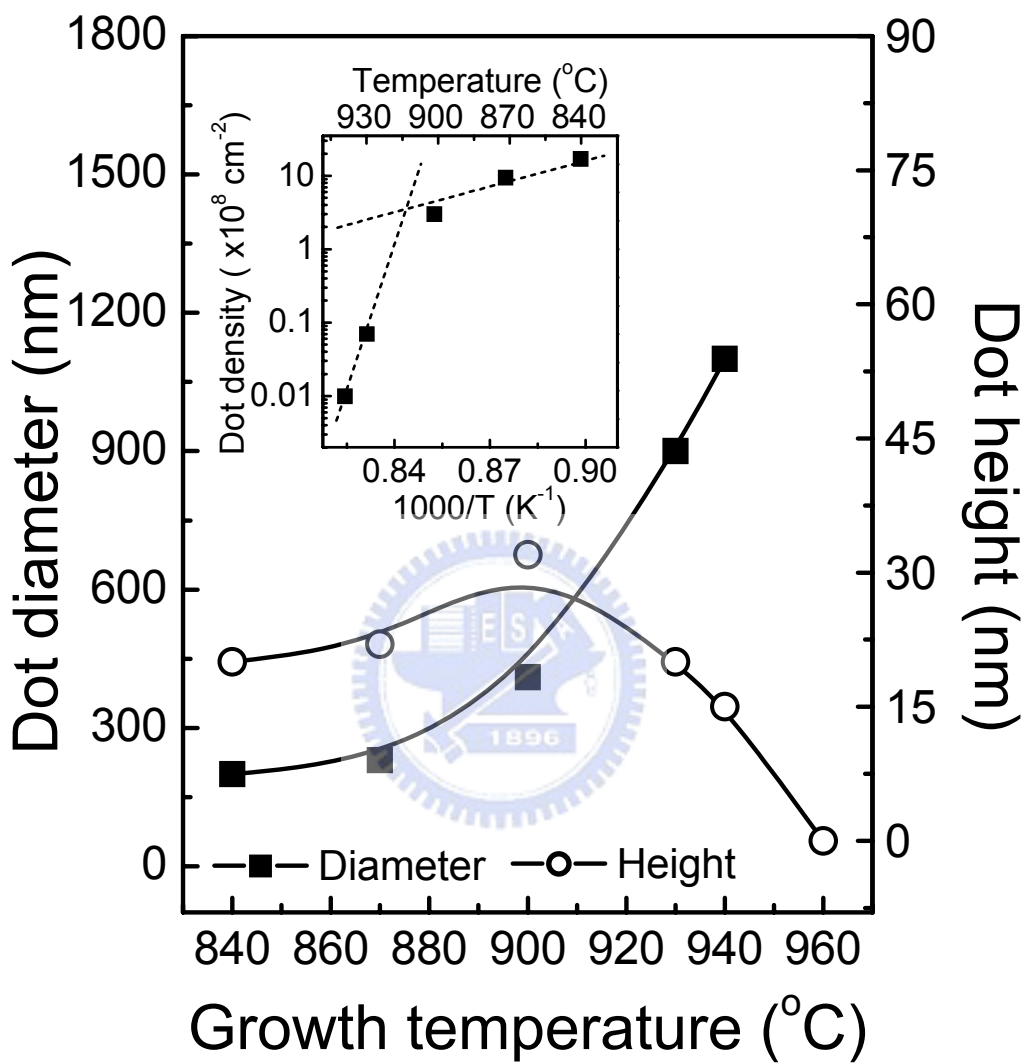


Fig. 4-4 Dependence of average diameter and height of GaN dots on growth temperature. The inset shows island density as a function of reciprocal temperature.

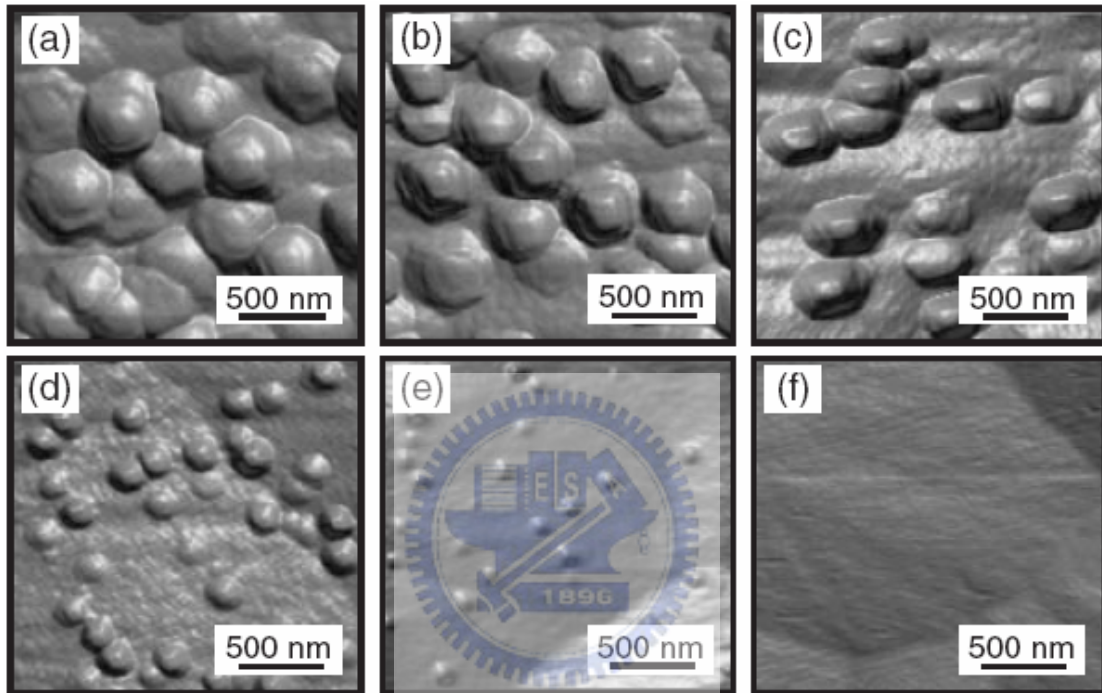


Fig. 4-5 AFM images of GaN dots grown by FME technique. The exposure times of TMGa are (a) 20, (b), 15 (c), 10 (d), 7 (e), 5 and (f) 0 s per cycle.

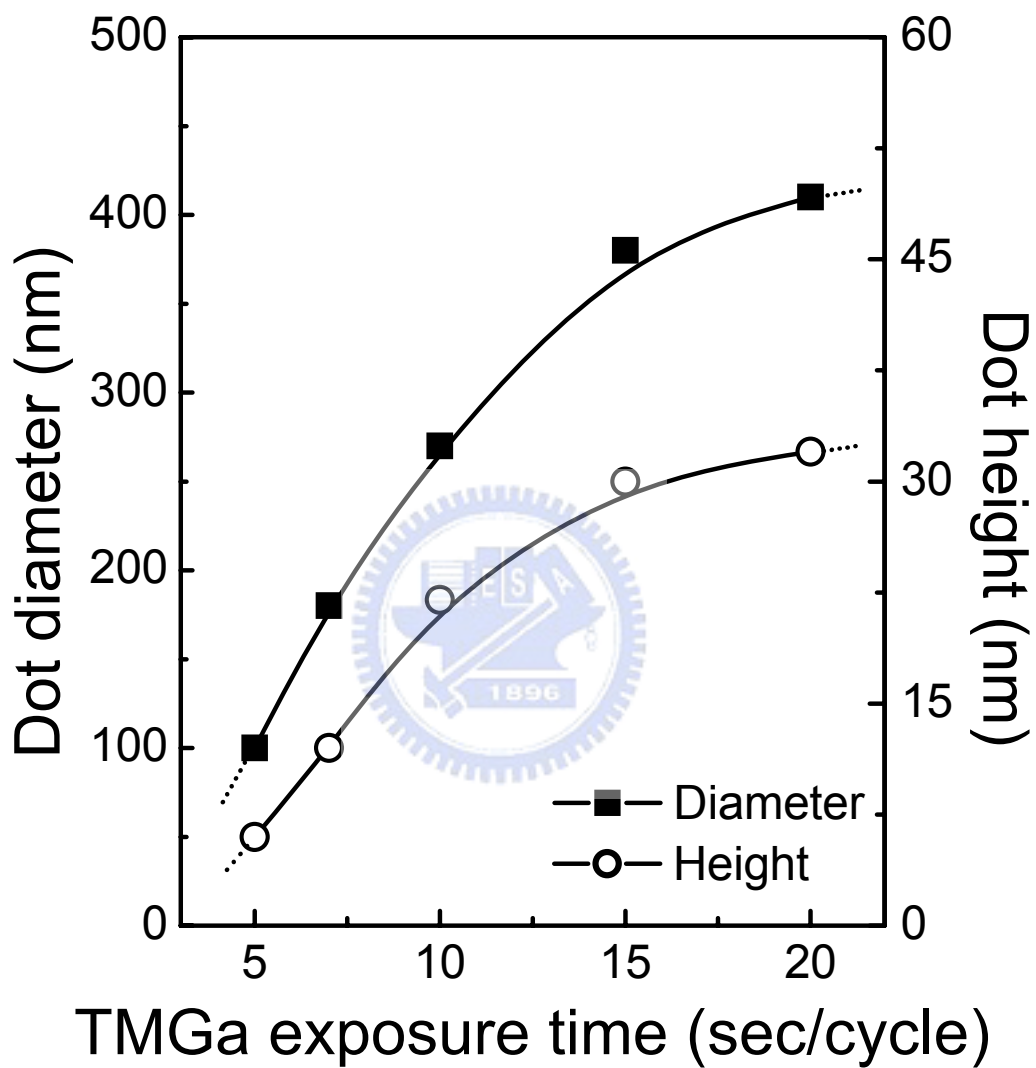


Fig. 4-6 Dependence of average diameter and height of GaN dots on exposure time of TMGa.

Chapter 5 Optical Properties of GaN Nanodots

GaN quantum dot (QD) has attracted a great deal of interest due to its potential application in single electron devices [1], solid state quantum computing [2], photo-detectors, and UV light emitting devices [3]. The major challenges to boost GaN QD in device applications are to improve the crystal quality, artificially control the size and density and fully understand its opto-electronic properties. To grow GaN QDs of perfect crystal quality and controlled size and density, several approaches were reported. The early growth of self-assembling GaN QDs was achieved by using a tetraethylsilane surfactant [4]. Recently, molecular beam epitaxy (MBE) was employed to control the density of GaN QDs [5]. High density and size control were also accomplished by metalorganic chemical vapor deposition (MOCVD) [6]. Additionally, a combination of electron-beam lithography and chemical vapor deposition was used to fabricate uniform GaN QD arrays [7]. In addition, vertically aligned GaN QDs were observed by transmission electron microscopy [8]. Moreover, deep level luminescence study indicated the existence of impurity-assisted QD assembly formation [9]. The exciton states of GaN/AlN QDs were also theoretically investigated [10]. However, the above-mentioned investigations are abstract of optical study. An additional understanding of optical properties as well as searching for alternative growth technique are urgent to drive the progress of GaN QD based device technology.

Recently, we have shown that flow rate modulation epitaxy (FME) is a successful technique to grow GaN QDs on rough $\text{Al}_{0.11}\text{Ga}_{0.89}\text{N}$ films by the Volmer-Weber growth mode [11]. In this study, we will show that by lowering the TMGa source flow time and decreasing the TMGa flow rate and increasing the number of cycles, the GaN QDs can be self-assembled on $\text{Al}_{0.11}\text{Ga}_{0.89}\text{N}$ buffer layer

by the Stranski-Krastanov (SK) growth mode. The small lattice mismatch and migration enhanced effect lead to the self-organization of the low aspect (height to diameter ratio is about 1/30) GaN QDs. The temperature dependent micro photoluminescence (μ -PL) spectra from 10 to 300K were obtained to investigate the size dependent localization and activation of QD excitonic state to the AlGaN barrier impurity state. The localization energy was found to increase with the increasing dot size. The decrease in the PL intensity above 100 K is due to the carrier escape from the QDs to the nitrogen vacancy (V_N) state of AlGaN barrier layer.



5-1 Experimental details

In previous chapter, we have demonstrated the GaN dots can be formed on rough AlGa_{0.11}N films by flow rate modulation epitaxy technique. In this chapter, we further show that not only on roughing surface the GaN QDs can be also grown successfully on smooth Al_{0.11}Ga_{0.89}N films. In this study, a nominal 25-nm-thick AlN nucleation layer was deposited at 600°C. The substrate temperature was then increased to 1120°C to grow a smooth 1.5 μm Al_{0.11}Ga_{0.89}N layer. The resulted roughness is ~0.25 nm. Then the GaN QDs were deposited at temperatures of 900°C by the FME technique. The gas flow sequence for FME basically consists of: Ga source step 3s, NH₃ source step 10s and intervening purge steps 5s in between. A total of 7 cycles were used. After the growth, the substrate temperature was then increased to 1000 °C to grow 30 nm-thick Al_{0.11}Ga_{0.89}N cap layer for optical measurements. The detailed growth conditions of GaN QDs on AlGa_{0.11}N films were described in Table 5-1. Uncapped GaN QDs were used to profile morphological structure of dots themselves using AFM measurement. In case of μ-PL measurements, a He-Cd laser operating at 325 nm was used for the above band-gap excitation and was focused to a spot size of 1.5 μm by a microscope objective lens (100×, NA 0.5). The signals were collected by the same objective lens into a monochromator (ARC-500) with both the entrance and exit slits opened to 50 μm so that the spectral resolution is about 0.2 nm.

In this study, the Al_{0.11}Ga_{0.89}N films were deposited on 25 nm AlN nucleation layer at 600°C. The surface morphology of the Al_{0.11}Ga_{0.89}N buffer layer measured by tapping-mode AFM was shown in Fig. 5-1(a). The root-mean-square roughness of the Al_{0.11}Ga_{0.89}N surface was ~0.25 nm in the area of 25 μm². After the growth of Al_{0.11}Ga_{0.89}N film, GaN dots were then grown on Al_{0.11}Ga_{0.89}N film at the condition

exactly the same in the chapter 4 (i.e. TMGa and NH₃ flow rate are 8.84×10^{-5} and 1.79×10^{-1} mol/min, respectively; TMGa step is 20 sec/cycle; growth temperature is 900°C). During the early stage, we made several FME growth at cycles of 5, 10 and 30, respectively. Beyond our exception, we observe no GaN dot formed on the smooth Al_{0.11}Ga_{0.89}N surface, in contrast to the results on roughed Al_{0.11}Ga_{0.89}N surface. Their AFM images are shown in Fig. 5-1(b), (c) and (d), respectively. Their surface roughness increased from 0.8 nm to 4.2 nm as the growth cycles increased from 5 to 30 cycles. The corresponding PL spectra measured at room temperature are shown in Fig. 5-2. The spectra are dominated by the near-band-edge (I_{nbe}) of GaN at 362 nm, which confirms absent of GaN dot growth on smooth AlGaN films.

To clarify the origin, we then conduct a thick GaN film growth by employing 100 cycles FME growth under the same TMGa flow rate of 8.84×10^{-5} mol/min with 20 sec per cycle during TMGa step. Fig. 5-3(a) and (b) show the cross section of SEM images of thick Al_{0.11}Ga_{0.89}N film itself and GaN on Al_{0.11}Ga_{0.89}N film, respectively. In both of the cases, the AlGaN films are prepared at exactly the same growth conditions, which implying the same thickness of both of AlGaN films. Since the thickness of AlGaN is 1.42 μm, and the thickness of GaN/AlGaN is 2.54 μm, the derived thickness of 100-cycles FME growth GaN films is of 1120 nm, corresponding to 11.2 nm/cycle. Obviously, such a growth rate is too high to form GaN QDs. Therefore, we decreased the TMGa flow rate to 2.21×10^{-5} mol/min and decreased the duration of TMGa step down to 3 sec/cycle and at the same time perform the GaN dot growth at FME cycles of 10 to 7 and 3 cycles (i.e. the estimated thickness of GaN are 14, 10 and 4 nm respectively for 10, 7 and 3 FME cycles). The resulted AFM images were shown in Fig. 5-4. Under this efforts still no islands was found on smooth Al_{0.11}Ga_{0.89}N films.

By referring to the conventional GaN dot growth by Y. Arakawa et al. and Gherasimova et al., in which rather very low V/III ratio (i.e. 26 and 0) was employed, we then accordingly decreased the NH₃ flow rate in NH₃ step. Fig. 5-5(b), (c) and (d) shows the AFM images of GaN QDs grown under the NH₃ flow rate at 2.68×10^{-2} , 1.34×10^{-2} to 4.46×10^{-3} mol/min, respectively. The TMGa flow rate was fixed at 2.21×10^{-5} mol/min. Finally, satisfactory results are obtained under such growth conditions, we are able to grow GaN dots usefully on the smooth Al_{0.11}Ga_{0.89}N films when NH₃ flow rate reduced down to 4.46×10^{-3} mol/min during NH₃ step.

Table 5-1: *The growth conditions of GaN QDs on AlGaN films.*

	Time (min)	Temperature (°C)	Pressure (mbar)	NH ₃ (mol/min)	TMGa (mol/min)	TMAI (mol/min)
Desorption	10	1120	200	-	-	-
Nucleation	3	600	100	8.93×10^{-2}	-	3.05×10^{-5}
Annealing	1	1120	50	8.93×10^{-2}	-	-
AlGaN	60	1120	50	1.12×10^{-1}	5.52×10^{-5}	8.72×10^{-6}
GaN dots (Ga step)	3 (sec)	900	200	0	$4.42 \times 10^{-6} \sim$ 3.31×10^{-5}	-
Purge	5 (sec)	900	200	$0-4.46 \times 10^{-3}$	-	-
GaN dots (NH ₃ step)	10 (sec)	900	200	4.46×10^{-3}	-	-
Purge	5 (sec)	900	200	$4.46 \times 10^{-3}-0$	-	-

5-2 GaN QDs growth mechanism

In order to understand the growth mechanism of GaN QDs on smooth AlGaIn films. We performed series of samples at different TMGa flow rate. Fig. 5-5 showed AFM image of smooth AlGaIn films. Fig 5-6(b)-(h) showed AFM images of GaN QDs grown at TMGa flow rate of from 4.42×10^{-6} , 1.33×10^{-5} , 1.77×10^{-5} , 1.99×10^{-5} , 2.21×10^{-5} , 2.65×10^{-5} and 3.31×10^{-5} mol/min, respectively. For the GaN films grown at 900°C , the growth rate is about $\sim 0.45 \text{ nm/sec}$ under $88.4 \mu \text{ mol/min}$ of TMGa flow rate, which implying a Ga growth efficiency of $0.305 \text{ nm}/\mu \text{ mol}$. Based on these results, the calculated coverage GaN thicknesses are list in Table 5-2. The resulted GaN QDs average height/diameter are also listed in Table 5-2. Obviously, the diameter is much far greater than the height giving to an aspect ratio of about 1/30. This result is different from that of other reports from other growth techniques [12]. Dot density versus GaN coverage thickness plot shows an abrupt increase near 7.2 MLs in Fig.5-7. The solid curve can be fitted theoretically using the equation:

$$\rho = \rho_0(\theta - \theta_c)^\alpha \quad (5-1),$$

proposed by D. Leonard *et al.*[13], where ρ is the dot density, θ is the estimated GaN coverage, and $\rho_0 = 6.72 \times 10^8 / \text{cm}^2$, $\theta_c = 7.2$ MLs, and $\alpha = 0.389$ are fitting parameters. From Fig.5-6, the SK growth mode with wetting layer (WL) thickness (θ_c) of 7.2 MLs is determined. This result is corroborated by the AFM investigations, i.e., no QD formation was observed in AFM for the samples grown with GaN coverage less than 7.2 MLs.

Table 5-2: Sample list of GaN QDs on AlGa_N films.

	TMGa flow rate (mol/min)	Coverage thickness (nm/ML)	Height/Diameter (nm/nm)	Density (cm ⁻²)
Sample A	4.42×10 ⁻⁶	0.47/1.8	-	-
Sample B	1.33×10 ⁻⁵	1.42/5.5	-	-
Sample C	1.77×10 ⁻⁵	1.89/7.3	~ 5.5 / 175	2.3×10 ⁸
Sample D	1.99×10 ⁻⁵	2.12/8.2	~ 6.0 / 180	6.2×10 ⁸
Sample E	2.21×10 ⁻⁵	2.25/8.7	~ 6.5 / 190	9.1×10 ⁸
Sample F	2.65×10 ⁻⁵	2.83/10.9	~ 7.0 / 200	1.1×10 ⁹
Sample G	3.31×10 ⁻⁵	3.5/13.6	~ 8.5 / 220	7.2×10 ⁸

For GaN QDs self-assembled on the AlN buffer layer, WL thickness of 2 to 4 MLs were reported [5,6,8]. P. Ramvall *et al.*[14] predicted that GaN QDs could not be self-assembled on Al_{0.15}Ga_{0.85}N buffer by SK growth mode. This is because that the lattice mismatch between GaN and Al_{0.15}Ga_{0.85}N is only 0.37%, which is too small for conducting SK mode growth which normally requires a lattice mismatch of 2-3%. By using chapter 4 described the calculation of the surface free energy. We finished the calculation of GaN QDs on different Al composition of AlGa_N films as shown in Table 5-3. From this table, we can observed that the wetting layer thickness is larger than 16 ML for GaN QDs on Al_{0.4}Ga_{0.6}N films. Therefore, the GaN QDs could not be grown on Al_{0.4}Ga_{0.6}N films by SK mode. Because GaN grown on Al_{0.4}Ga_{0.6}N films will prefer to form 2D layer growth with dislocation.

Table 5-3: The calculated surface energy and wetting layer thickness of GaN QDs on different Al composition of AlGa_xN films.

	Substrate surface energy (meV/Å ²)	Interface energy (meV/Å ²)	Strain energy (meV/Å ²)	Wetting layer (ML)
GaN QDs/AlN	165	3.93	5.39	4.3
GaN QDs/Al _{0.8} Ga _{0.2} N	156	2.89	3.42	5.9
GaN QDs/Al _{0.6} Ga _{0.4} N	146	1.98	1.90	8.9
GaN QDs/Al _{0.4} Ga _{0.6} N	137	1.20	0.84	16.3
GaN QDs/Al _{0.2} Ga _{0.8} N	127	0.54	0.21	49.8
GaN QDs/Al _{0.15} Ga _{0.85} N	125	0.39	0.12	81.5
GaN QDs/Al _{0.11} Ga _{0.89} N	123	0.28	0.06	141

From above discussion, it was known that it is impossible to grow GaN QDs on smaller than 40% Al composition of AlGa_xN films by conventional MOCVD growth method. Therefore, in this work, we show that SK GaN QDs can be self-assembled on Al_{0.11}Ga_{0.89}N epilayer by using the FME growth technique. Because of the lower NH₃ flow rate was used during TMGa step in FME growth process, a metal Ga and Ga-rich island was formed on the Al_{0.11}Ga_{0.89}N epilayer. The surface free energies of Al_{0.11}Ga_{0.89}N and Ga-rich island¹⁶⁾ are ~123 and 45 meV/Å², respectively. To meet the island growth constraint, it would need at least an additional ~78 meV/Å². The calculated interface energy is 31.5 meV/Å² and the additional strain energy must be larger than 46.5 meV/Å² (i.e. the wetting layer at less >7.2 ML (18 Å)) to form GaN

dots on $\text{Al}_{0.11}\text{Ga}_{0.89}\text{N}$ films. In chapter 4, we show that GaN dots were grown on the lower angle facet of $\text{Al}_{0.11}\text{Ga}_{0.89}\text{N}$ hillock. Because of the surface energy of $\text{AlGaN}(1-101)$ surface is small than the $\text{AlGaN}(0001)$ surface. The surface free energy of AlGaN hillocks is smaller than smooth AlGaN films. Thus, VW growth mode is easy obtained for GaN dots on AlGaN hillocks. However, in order to form GaN dots on smooth AlGaN films, there must be accumulated the strain energy by wetting layer to form GaN dots.



5-3 Micro-Photoluminescence (μ -PL) Spectra of GaN Nanodots

The AFM images of GaN QDs used for optical measurement are shown in Fig. 5-8. The average height/diameter of GaN QDs are 6.5/190, 7.0/200, and 8.5/220 nm, respectively. The 10 K μ -PL spectra of the Al_{0.11}Ga_{0.89}N epilayer and above three self-organized GaN QDs are shown in Fig. 5-9(a) to (d). As can be seen in Fig. 5-9(a), the μ -PL spectrum of Al_{0.11}Ga_{0.89}N epilayer alone is dominated by the near-band-edge (I_{nbe}) emission, at 3.651 eV. The additional peak (I_{defect}) at 3.594 eV, is 57 meV lower than I_{nbe} , can be attributed to be a defect-related emission (i.e. nitrogen vacancy, V_{N}) from the Al_{0.11}Ga_{0.89}N epilayer. In Fig. 5-9(b)-(d), the energy positions of the GaN dots, labeled as I_{QD} , were determined by a polynomial fit to the PL signals. The results are 3.487, 3.510, and 3.546 eV for the 8.5/220, 7/200, and 6.5/190 nm thick GaN dots, respectively. The I_{QD} peak positions are 7, 30, and 66 meV higher than that of bulk GaN.

Such a blue-shift can be approximated simply by considering electrons or holes in a rectangular box. The calculated confinement energy of the ground state is expressed as:

$$E = \frac{\hbar^2}{8} \left(\frac{1}{m_x d_x^2} + \frac{1}{m_y d_y^2} + \frac{1}{m_z d_z^2} \right) \quad (5-2),$$

where, d_x , d_y , and d_z denote the dimensions of the box and m_x , m_y , and m_z represent the effective mass of electron in x, y, and z directions, respectively. For a disk-like dot, the in-plane sizes d_x and d_y are much larger than the height $d_z = d$. Thus, the above equation (5-2) can be further simplified as

$$E = \frac{\hbar^2}{8m_{ez}d^2} \quad (5-3),$$

in case of disk-like GaN dots, GaN $m_{ez} = 0.2 m_0$, $m_{hz} = 1.0 m_0$. The calculated results as a function of dot height are depicted as solid curve in Fig. 5-10. For comparison, the curve based on spherical dot model, denoted by dashed curve, from the relevant equation $E = h^2/2m_{ez}d^2$ are also included in the figure. The square points represent experimental PL data measured from our disk-like GaN dot samples. The horizontal bars are obtained from AFM measurements to represent the size fluctuation. We show that the experimental results agree well with the theoretical calculations. In this figure, the results from other groups are also included. Except for Hu et al. data, all of the PL spectra of GaN QDs from else research groups behave essentially the disk-like dot behavior.



5-4 Temperature Dependent of μ -PL Spectra of GaN Nanodots

To further examine the optical properties of GaN QDs, we also carried out the temperature dependent μ -PL measurements from 10K to 300K. The temperature dependence of the emission energy is shown in Fig. 5-11. The expected temperature dependence (dashed curves) was calculated by using the Varshni's equation [15],

$$E_g(T) = E_g(0) - \frac{\alpha T^2}{\beta + T} \quad (5-4),$$

where $E_g(T)$ and $E_g(0)$ are the band gap energies at temperatures T and 0 K, and α and β are fitting parameters that are characteristics of a given material. For $T > 100$ K the shift of the I_{QD} energy follows the typical band gap emission of a bulk semiconductor: a decrease of the emission energy with increasing temperature due to thermal expansion, which is well described by the Varshni's model. However, at low temperatures, the PL peak energy exhibits an initial blue-shift then red-shift. It is a representative property for the thermalization from a localized state to a higher energy state. The energy difference between the Varshni's prediction (dashed curves) and the observed PL peak energy gives a crude estimate of the localization energy. The strength of carrier localization increases with dot size. The localization energies for the 8.5 nm, 7 nm, and 6.5 nm GaN dots are 28, 19, and 6 meV, respectively. For the III-V and II-VI self-assembled QDs systems grown by SK mode [16-19], a stronger red shift than bulk material in PL energy was observed at high temperature following the initial blue shift at low temperature. The initial blue-shift then strong red-shift can be attributed to the exciton thermalization from smaller dots and then transport to larger dots through the underlying wetting layer [16-19]. A steady state model for the carrier dynamics which takes into account the QD size distribution, random population effects, carrier capture and relaxation, and re-trapping was presented to

explain the above phenomena [20]. However, in current study, the line width narrowing and the strong red shift were not observed for the SK GaN QDs. It could be due to the large lateral size and short carrier recombination time. Thermalization of carriers from smaller dots to larger dots is not possible. However, due to the large diameter/height ratio, the QDs could be treated as quasi-2D islands with different quantum confinement energies in different locations within the island owing to different height of the QD at different locations. Temperature-activated hopping of excitons/carriers within the island could not be excluded.

In order to identify the mechanism of the PL quenching, the temperature dependence of the PL integrated intensity of GaN QDs is shown in Fig.5-12. The following formula [21] was used to fit our experimental results,

$$I(T) = \frac{I(0)}{\left[1 + C_1 \exp\left(-\frac{E_a}{kT}\right) + C_2 \exp\left(-\frac{E_{loc}}{kT}\right) \right]} \quad (5-5),$$

where $I(T)$ and $I(0)$ are the integrated intensities at temperatures T and 0 K. C_1 and C_2 are fitting parameters. E_a and E_{loc} are the activation energy and localization energy at the high and low temperature regime, respectively. Localization energies, E_{loc} , are 7 ± 2 , 14 ± 1 , and 30 ± 2 meV for the 6.5/190, 7.0/200, and 8.5/220 nm dots, respectively. The localization energy obtained in this way agrees with the results of Fig.5-11. The thermal activation energies (E_a) are 43 ± 4 , 70 ± 13 , and 106 ± 13 meV for the 6.5/190, 7.0/200, and 8.5/220 nm dots, respectively. The activation energy increases with the increasing dot size. Similar behavior was clearly studied in the AlGaIn/GaN quantum well system. In general, the temperature-induced quenching of luminescence in the low dimensional structures could involve thermal emission of (at least one type of) charge carriers out of confined quantum-dot (well) states into barrier states [22,23], thermal dissociation of excitons into free-electron-hole pairs [24], and thermal

activation of excitons to non-radiative defect states [25]. The activation energy is a quantity to measure the exciton binding energy or the energy difference between the energy of quantum dot (well) confined state and the barrier continuum state or defect state. In our high temperature (100K) μ -PL spectra, the energy differences (E_b) between the GaN QD (I_{QD}) state and AlGaN barrier (which is close to I_{nbe}) energy are 114, 131, and 173 meV for 6.5/190, 7.0/200, and 8.5/220 nm dots, respectively. The E_b energies do not match E_a of the high temperature activation energies obtained by Fig.5. On the other hand, it was found that the energy differences, 43 meV (6.5/190), 69 meV (7.0/200), and 104 meV (8.5/220), between the defect state of $Al_{0.11}Ga_{0.89}N$ ($I_{defects}$) and the GaN QD (I_{QD}) are close to the activation energies E_a obtained from Fig.5-11. Furthermore, the electron states associated with nitrogen vacancy (V_N) in GaN and AlN are respectively located at about 30 and 200 meV [26] below the conduction band. Assuming a linear dependence of the energy level of nitrogen vacancy (V_N) on the aluminum (Al) concentration, the nitrogen vacancy (V_N) of $Al_{0.11}Ga_{0.89}N$ lies about 50 meV below the conduction band. Therefore, the extra peak (I_{defect}) at 3.594 eV, which is 57 meV lower than I_{nbe} , is possibly attributed to be a nitrogen vacancy emission from the $Al_{0.11}Ga_{0.89}N$ epilayer. The band schematic Fig. 5-13 Schematic band diagrams of GaN QDs with height of 8.5 nm (a) 10 K and (b) >100 K. Therefore, we believed that the charge carriers likely escape from the confined QD state to the nitrogen vacancy (V_N) state of $Al_{0.11}Ga_{0.89}N$ barrier for $T > 100K$. The nitrogen vacancy (V_N) state of $Al_{0.11}Ga_{0.89}N$ provides a carrier escape channel for quenching the PL intensity.

5-5 Conclusions of Optical Properties of GaN Nonodots

In summary, we have shown that GaN QDs can be self-assembled on $\text{Al}_{0.11}\text{Ga}_{0.89}\text{N}$ films by FME. The AFM measurements showed the SK growth mode with a WL thickness of 7.2 MLs. The localization energy was found to increase with the increasing dot size. The decrease in the PL intensity above 100 K is due to the carrier escape from the QDs to the nitrogen vacancy (V_N) state of AlGaN barrier layer.



References

- [1] Koji. Kawasaki, Daisuke Yamazaki, Atsuhiro Kinoshita, Hideki Hirayama, Kazuo Tsutsui and Yoshinobu Aoyagi 2001 Appl. Phys. Lett. **79**, 2243 ; Irene D'Amico and Fausto Fossi 2002 Appl. Phys. Lett. **81**, 5213
- [2] Irene D'Amico, Eliana Biolatti, Fausto Rossi, Sergio Derinaldis, Ross Rinaldis, Roberto Cingolani 2002 Superlattices and Microstructures **31**, 117 ; S. De Rinaldis, I. D'Amico, E. Biolatti, R. Rinaldi, R. Cingolani, and F. Rossi 2002 Phys. Rev. **B65**, 081309
- [3] B. Damilano, N. Grandjean, F. Semon, J. Massies, and M. Leroux 1999 Appl. Phys. Lett. **75**, 962
- [4] Satoru Tanaka, Sohachi Iwai, and Yoshinobu Aoyagi 1996 Appl. Phys. Lett. **69**, 4096
- [5] J. Brown, F. Wu, P. M. Petroff and J. S. Speck 2004 Appl. Phys. Lett. **84**, 690
- [6] M. Miyamura, K. Tachibana, and Y. Arakawa 2002 Appl. Phys. Lett. **80**, 3937
- [7] P.A. Crozier, J. Tolle, J. Kouvetakis, and Cole Ritter 2004 Appl. Phys. Lett. **84**, 3441
- [8] K. Hoshino, S. Kako, and Y. Arakawa 2004 Appl. Phys. Lett. **85**, 1262
- [9] G. N. Panin, Y. S. Park, T. W. Kang, T. W. Kim, K. L. Wang and M. Bao 2005 J. Appl. Phys. **97**, 043527
- [10] Vladimir A. Fonoberov and Alexander A. Balandin 2003 J. Appl. Phys. **94**, 7178
- [11] Wen-Cheng Ke, Huai-Ying Huang, Ching-Shun Ku, Kao-Hsi Yen, Ling Lee, Wei-Kuo Chen, Wu-Ching Chou, Ming-Chih Lee, Wen-Hsiung Chen, Wen-Jen Lin, Yi-Cheng Cheng and Ya-Tong Cherng 2004 Jpn. J. Appl. Phys. **43**, 6B, L780
- [12] M. Arlery, J. L. Rouvière, F. Widmann, B. Daudin, G. Feuillet and H. Mariette 1999 Appl. Phys. Lett. **74**, 3287 ; E. Martinez-Guerrero, C. Adelman, F. Chabuel, J. Simon, N. T. Pelekanos, Guido Mula, B. Daudin, G. Feuillet, and H. Mariette 2000 Appl. Phys. Lett. **77**, 809
- [13] D. Leonard, K. Pond, and P. M. Petroff 1994 Phys. Rev. **B50**, 11687
- [14] Peter Ramvall, Satoru Tanaka, Shintaro Nomura, Philippe Riblet, and Yoshinobu Aoyagi 1999 Appl. Phys. Lett. **75**, 1935
- [15] Y.P. Varshni, Physica **34**, 149 (1967).
- [16] A. Polimeni, A. Patanè, M. Henini, L. Eaves, and P. C. Main 1999 Phys. Rev.

B59, 5064

- [17] J. Seufert, M. Rambach, G. Bacher, A. Forchel, M. Keim, S. Ivanov, A. Waag, and G. Landwehr 2000 Phys. Rev. **B62**, 12609
- [18] G. Karczewski, S. Maćkowski, M. Kutrowski, T. Wojtowicz, and J. Kossut 1999 Appl. Phys. Lett. **74**, 3011
- [19] C. S. Yang, Y. J. Lai, W. C. Chou, W. K. Chen, M. C. Lee, M. C. Kuo, J. Lee, J. L. Shen, D. J. Jang and Y. C. Cheng 2005 J. Appl. Phys. **97**, 033514
- [20] S. Sanguinetti, M. Henini, M. Grassi Alessi, M. Capizzi, P. Frigeri and S. Franchi 1999 Phys. Rev. **B60**, 8276
- [21] I. Friel, C. Thomidis, and T. D. Moustakas 2004 Appl. Phys. Lett. **85**, 3068
- [22] S. Weber, W. Limmer, K. Thonke, R. Sauer, K. Panzlaff, G. Bacher, H. P. Meier and P. Roentgen 1995 Phys. Rev. **B52**, 14747
- [23] Y. T. Shih, Y. L. Tsai, C. T. Yuan, C. Y. Chen, C. S. Yang, and W. C. Chou 2004 J. Appl. Phys. **96**, 7267
- [24] I. Ya. Gerlovin, Yu. K. Dolgikh, V. V. Ovsyankin, Yu. P. Efimov, I. V. Ignat'ev, and E. E. Novitskaya 1998 Phys. Solid State **40**, 1041
- [25] Yi-hong Wu, Kenta Arai and Takafumi Yao 1996 Phys. Rev. **B53**, 10485
- [26] T. L. Tansley and R. J. Egan 1992 Phys. Rev. **B45**, 10942

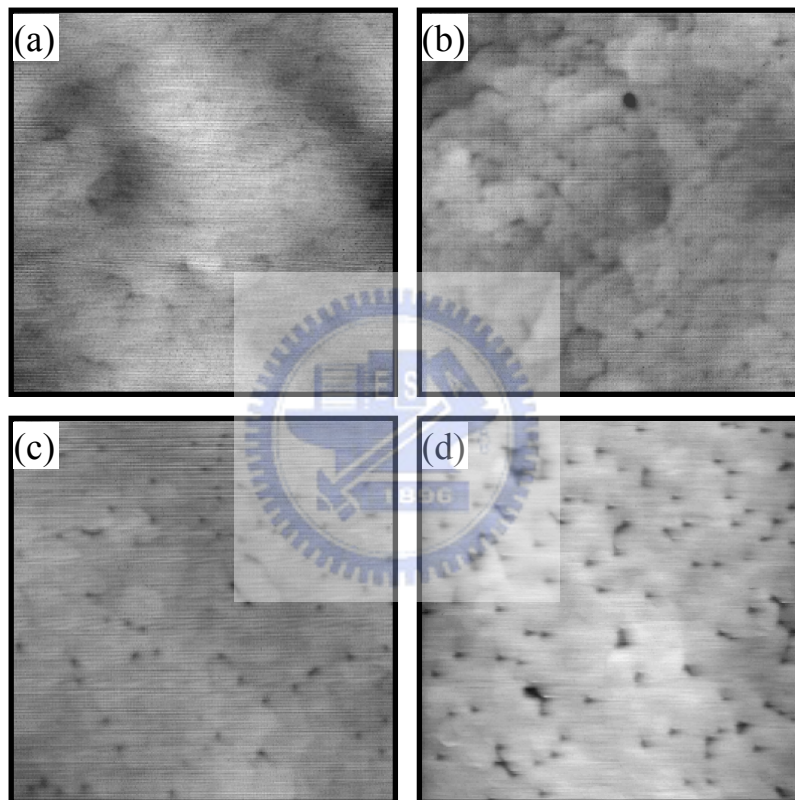


Fig. 5-1 Plane view image of a $5\mu\text{m} \times 5\mu\text{m}$ AFM scan on (a) the $\text{Al}_{0.11}\text{Ga}_{0.89}\text{N}$ buffer layer, the GaN QD samples grown on $\text{Al}_{0.11}\text{Ga}_{0.89}\text{N}$ buffer layers with different FME cycles (b) 5, (c) 10 and (d) 30 cycles.

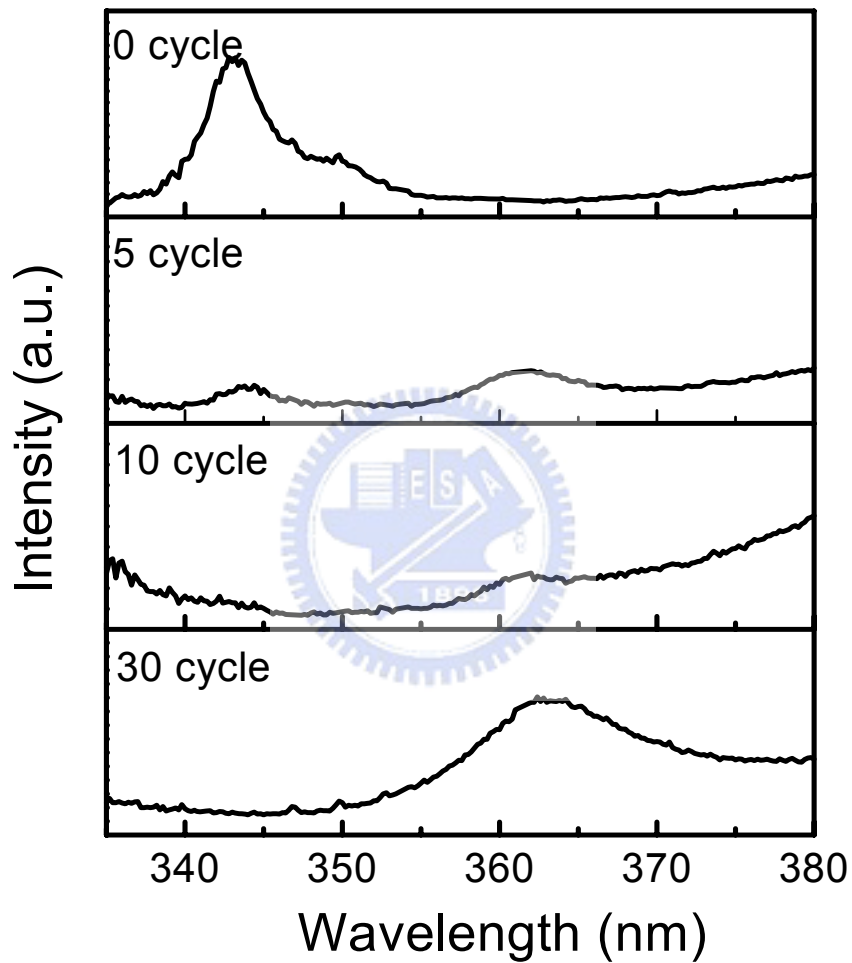


Fig. 5-2 Room temperature μ -PL spectra of (a) $\text{Al}_{0.11}\text{Ga}_{0.89}\text{N}$ epilayer, the GaN QD samples grown on $\text{Al}_{0.11}\text{Ga}_{0.89}\text{N}$ buffer layers with different FME cycles (b) 10, (c) 20 and (d) 30 cycles.

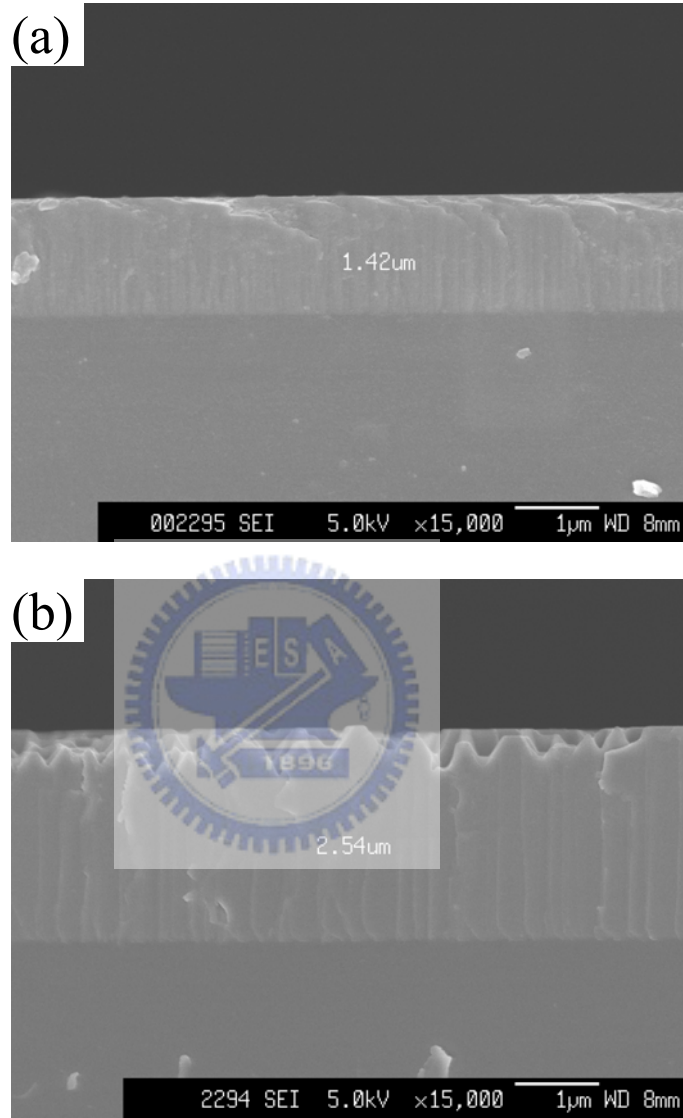


Fig. 5-3(a) The cross-section SEM images of (a) Al_{0.11}Ga_{0.89}N epilayer, the GaN with 100 FME cycles grown on Al_{0.11}Ga_{0.89}N buffer layers.

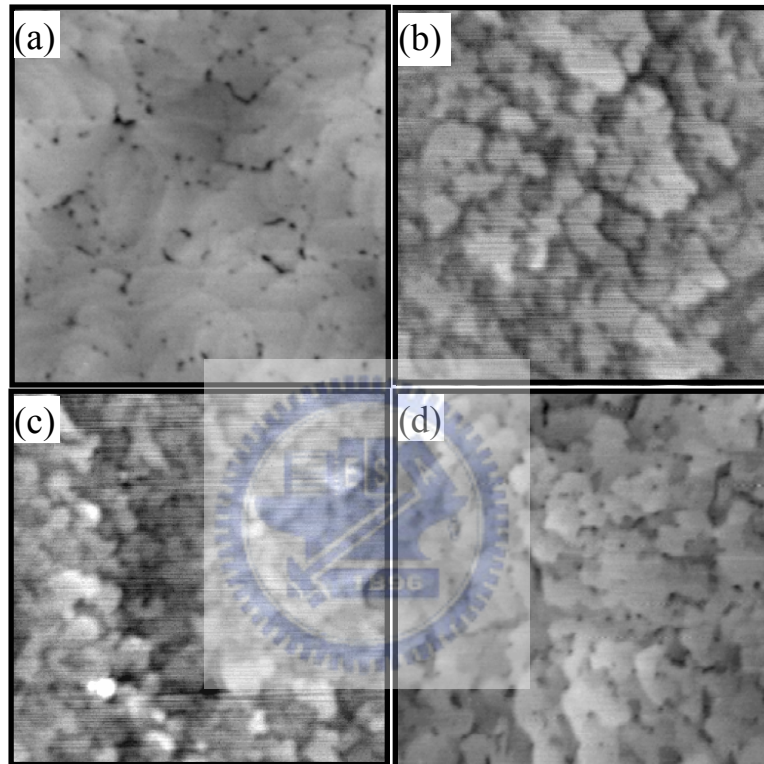


Fig. 5-4 Plane view image of a $2\mu\text{m} \times 2\mu\text{m}$ AFM scan on (a) the $\text{Al}_{0.11}\text{Ga}_{0.89}\text{N}$ buffer layer, the GaN QD samples grown on $\text{Al}_{0.11}\text{Ga}_{0.89}\text{N}$ buffer layers with different FME cycles (b) 10, (c) 7 and (d) 3 cycles.

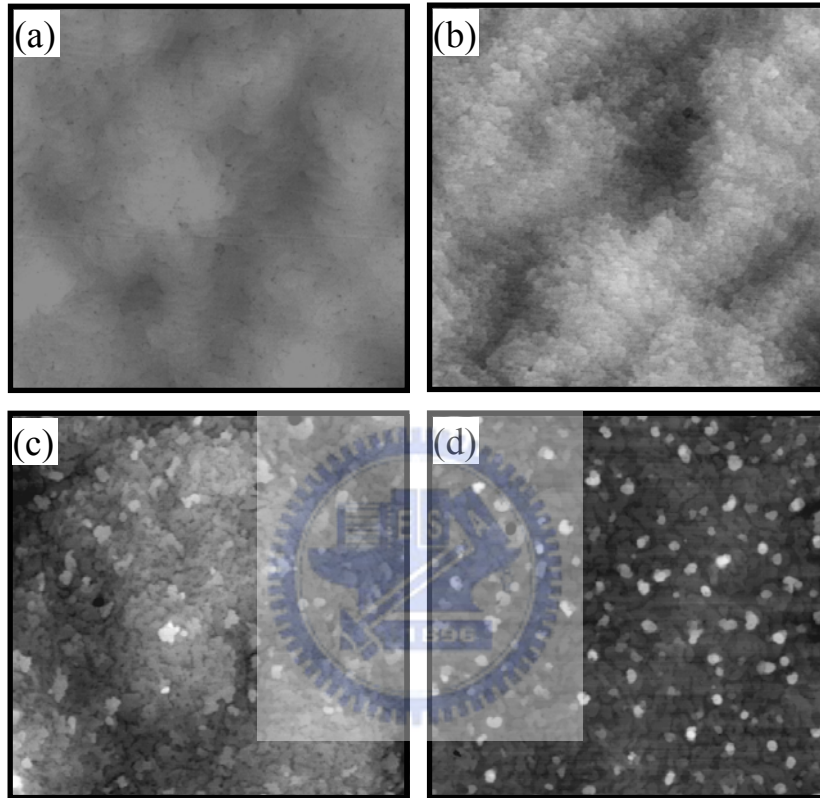


Fig. 5-5 Plane view image of a $5\mu\text{m} \times 5\mu\text{m}$ AFM scan on (a) the $\text{Al}_{0.11}\text{Ga}_{0.89}\text{N}$ buffer layer, the GaN QD samples grown on $\text{Al}_{0.11}\text{Ga}_{0.89}\text{N}$ buffer layers with different NH_3 flow rate during NH_3 flow period of (b) 2.68×10^{-2} , (c) 1.34×10^{-2} , and (d) 4.46×10^{-3} mol/min. The TMGa flow rate was 1.99×10^{-5} mol/min.

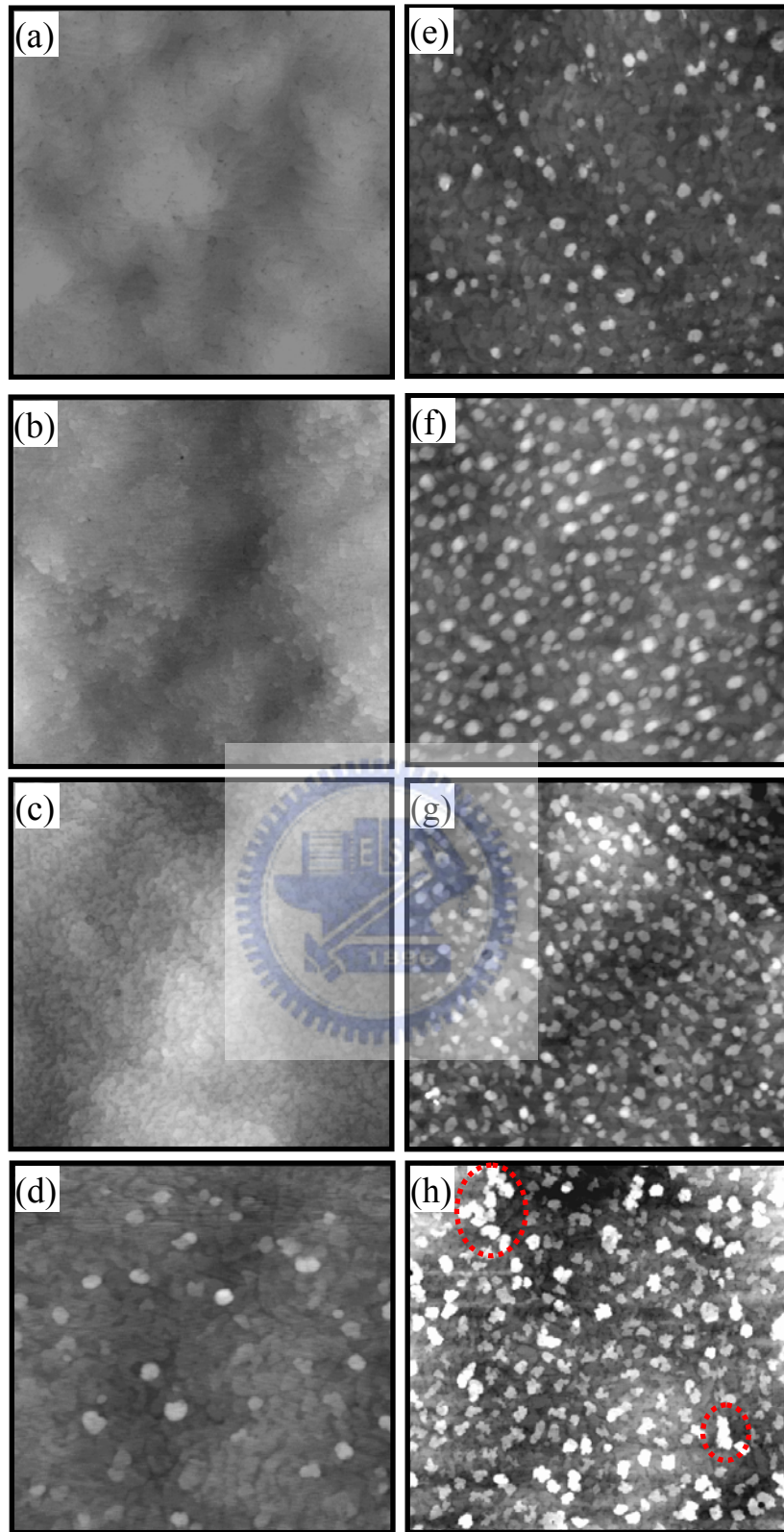


Fig. 5-6 Plane view image of a $5\mu\text{m} \times 5\mu\text{m}$ AFM scan on (a) the $\text{Al}_{0.11}\text{Ga}_{0.89}\text{N}$ buffer layer, the GaN QD samples grown on $\text{Al}_{0.11}\text{Ga}_{0.89}\text{N}$ buffer layers with different GaN coverage of (a) 2, (b) 5.5, (c) 7.3, (d) 8.2, (e) 9.1, (f) 10.9, and (g) 13.6 MLs.

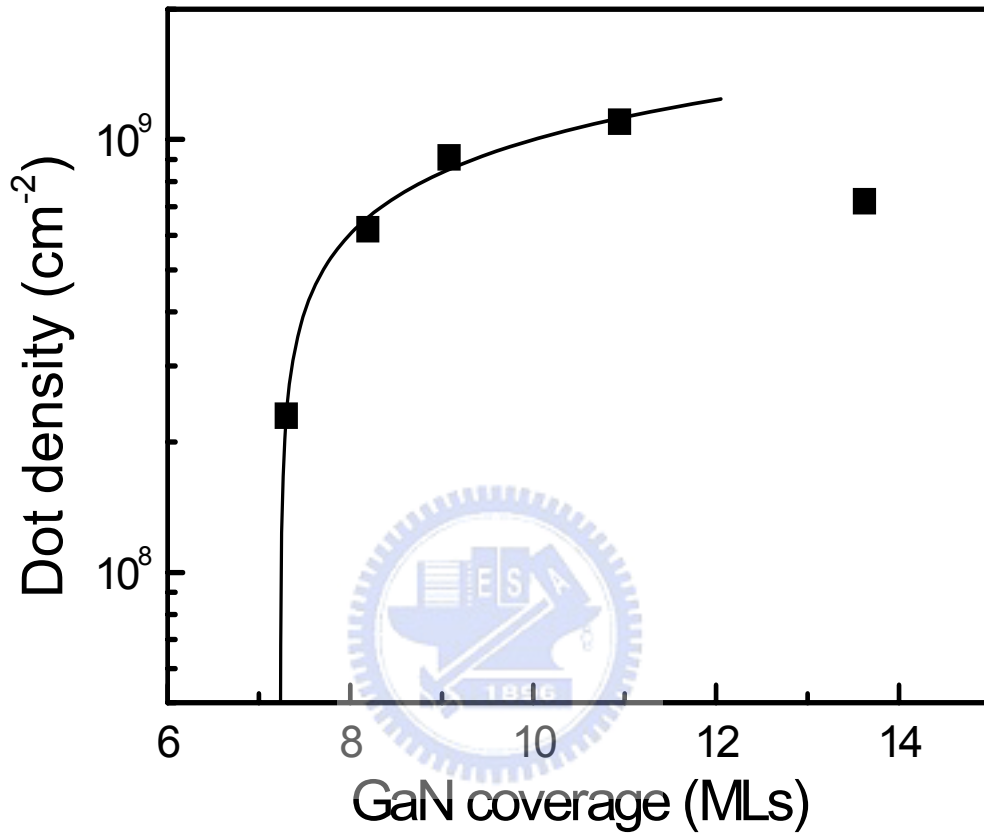


Fig.5-7 Dot density versus average coverage plot of the GaN QDs. The solid curve is a fit using equation (5-1).

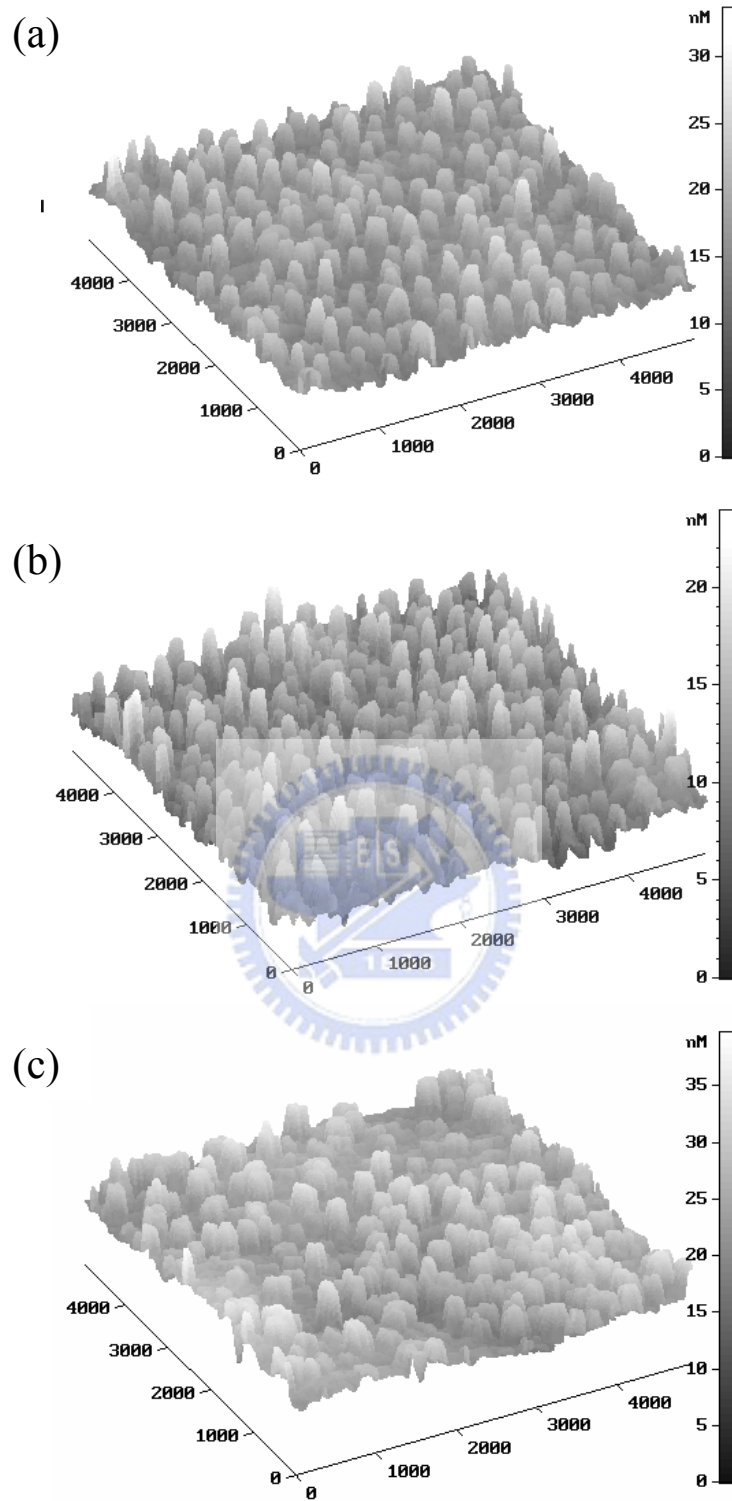


Fig. 5-8 3D image of a $5\mu\text{m} \times 5\mu\text{m}$ AFM scan of the GaN QD samples grown on $\text{Al}_{0.11}\text{Ga}_{0.89}\text{N}$ buffer layers with different height (a) 6.5 nm, (b) 7 nm and (c) 8.5 nm.

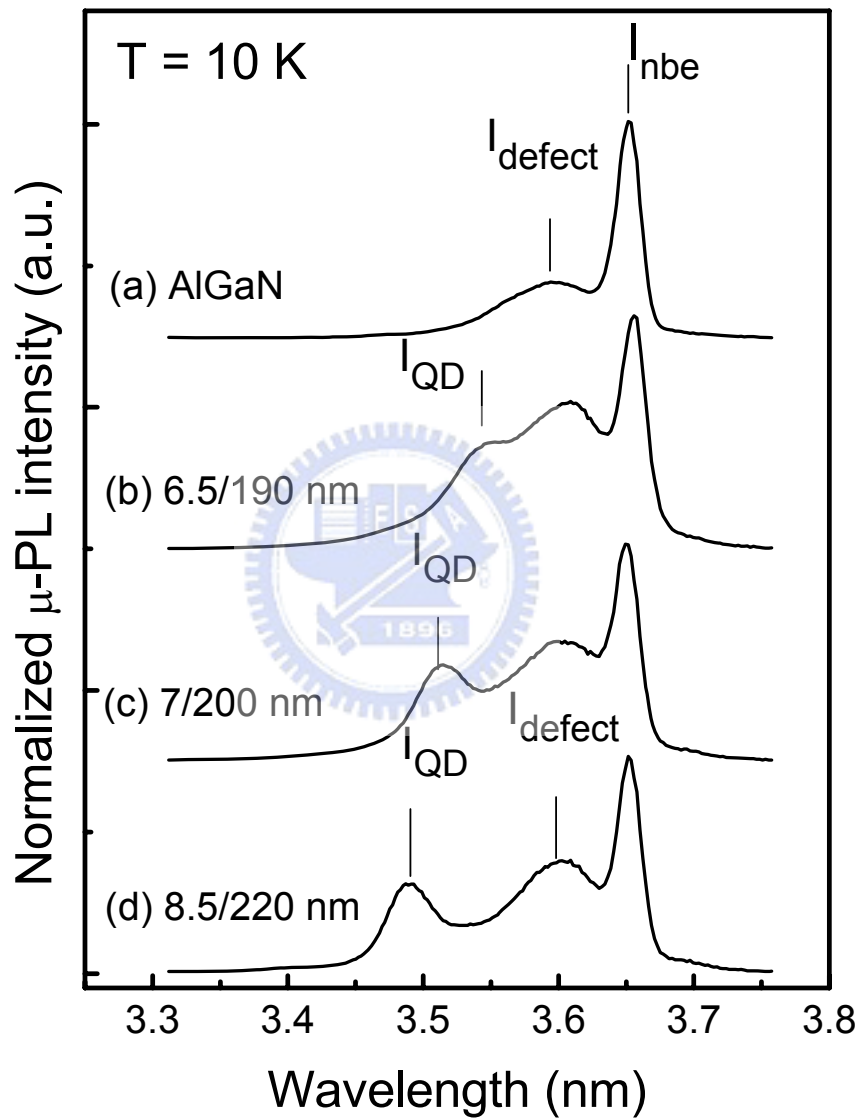


Fig. 5-9 Normalized μ -PL spectra at 10 K of (a) $\text{Al}_{0.11}\text{Ga}_{0.89}\text{N}$ epilayer, and the GaN QD samples grown on $\text{Al}_{0.11}\text{Ga}_{0.89}\text{N}$ buffer layers with different GaN coverage of (b) 9.1 MLs, (c) 10.9 MLs, and (d) 13.6 MLs.

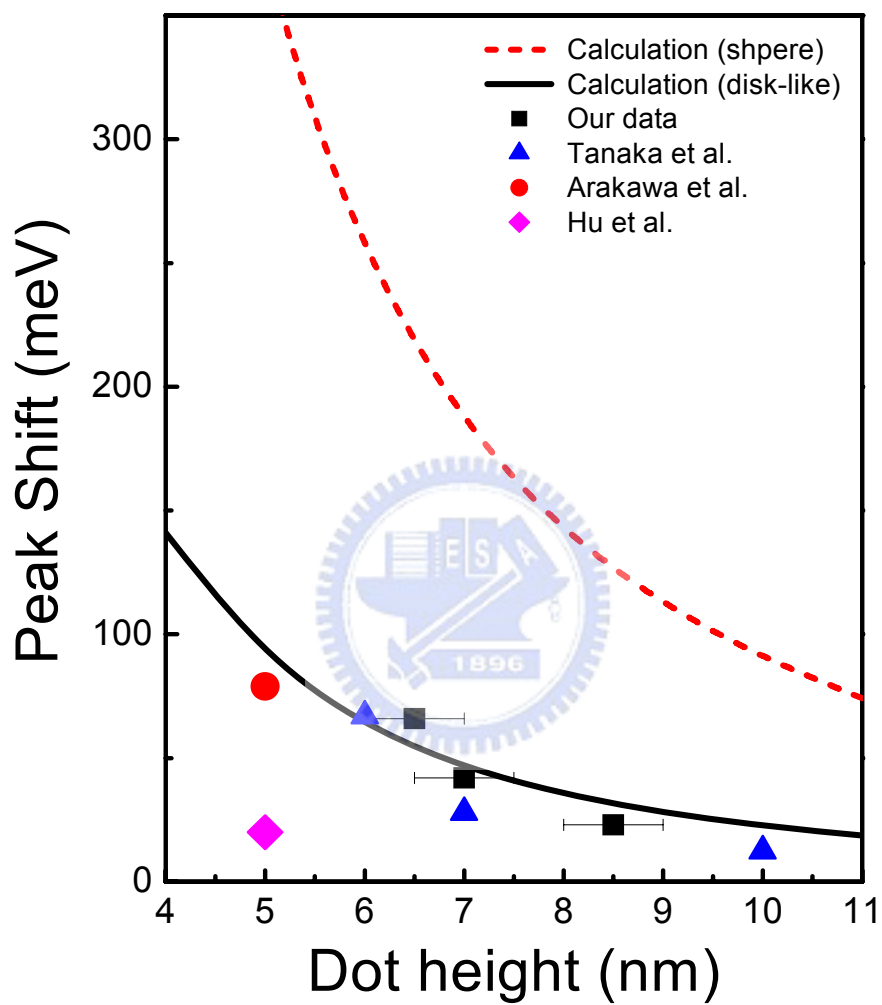


Fig. 5-10 Comparison with the PL experimental data and calculation derived from the disk-like rectangular box model.

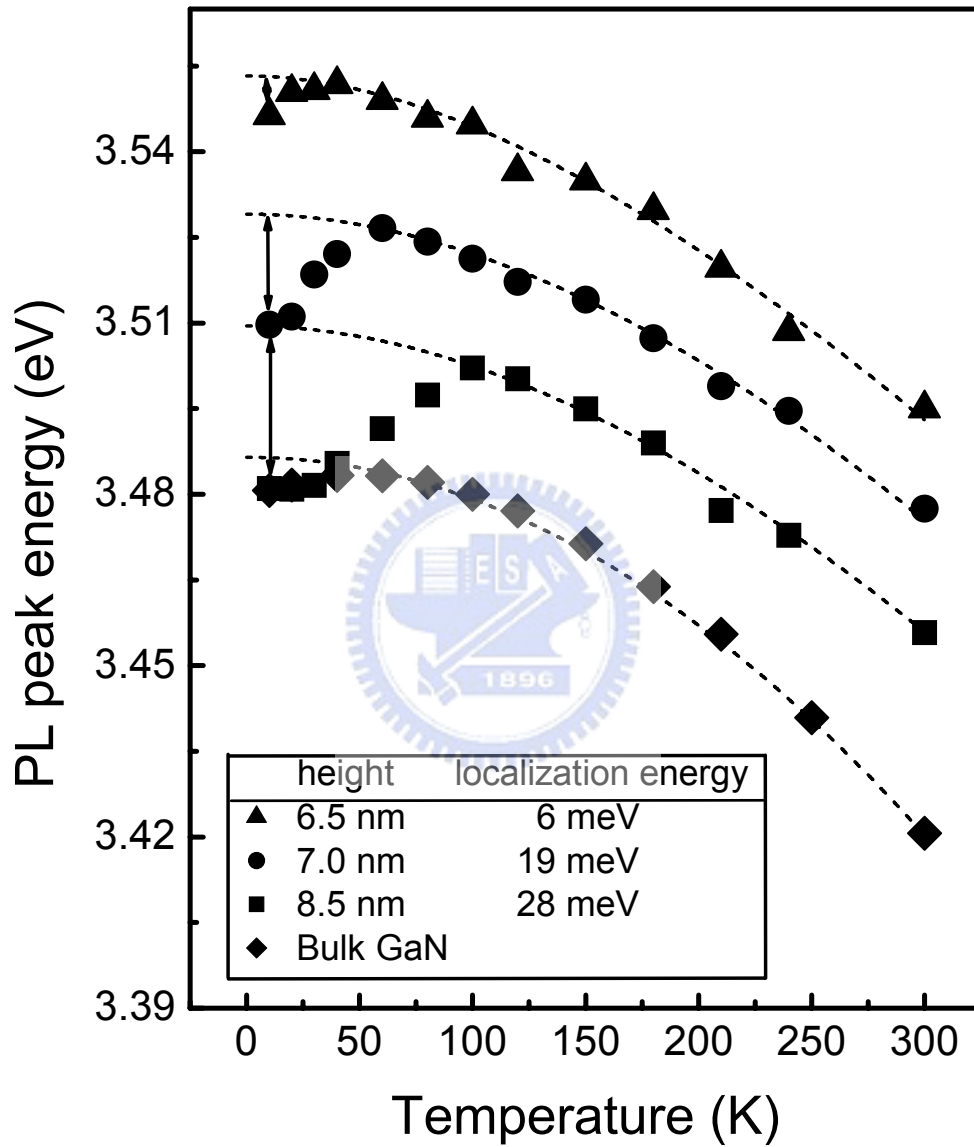


Fig.5-11 PL peak energy as a function of temperature for the 6.5 nm (triangles), 7.0 nm (circles), 8.5 nm (squares) GaN dot and the GaN epilayer (rhombus). The dashed lines are theoretical fits using equation (2), Vashini's equation.

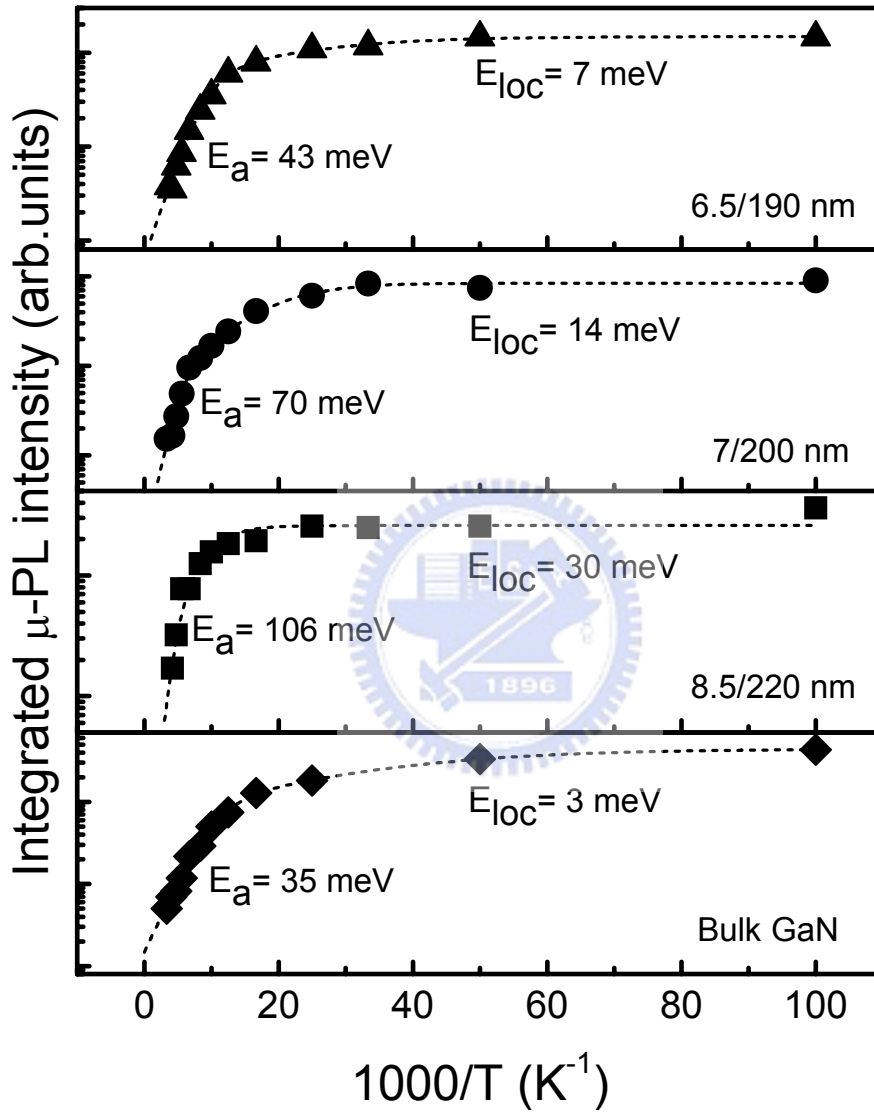


Fig.5-12 PL integrated intensity as a function of temperature for the dot height of 6.5 nm, 7.0 nm, 8.5 nm and the GaN epilayer. The dashed lines represent the fitting by using the Arrhenius equation, equation (3).

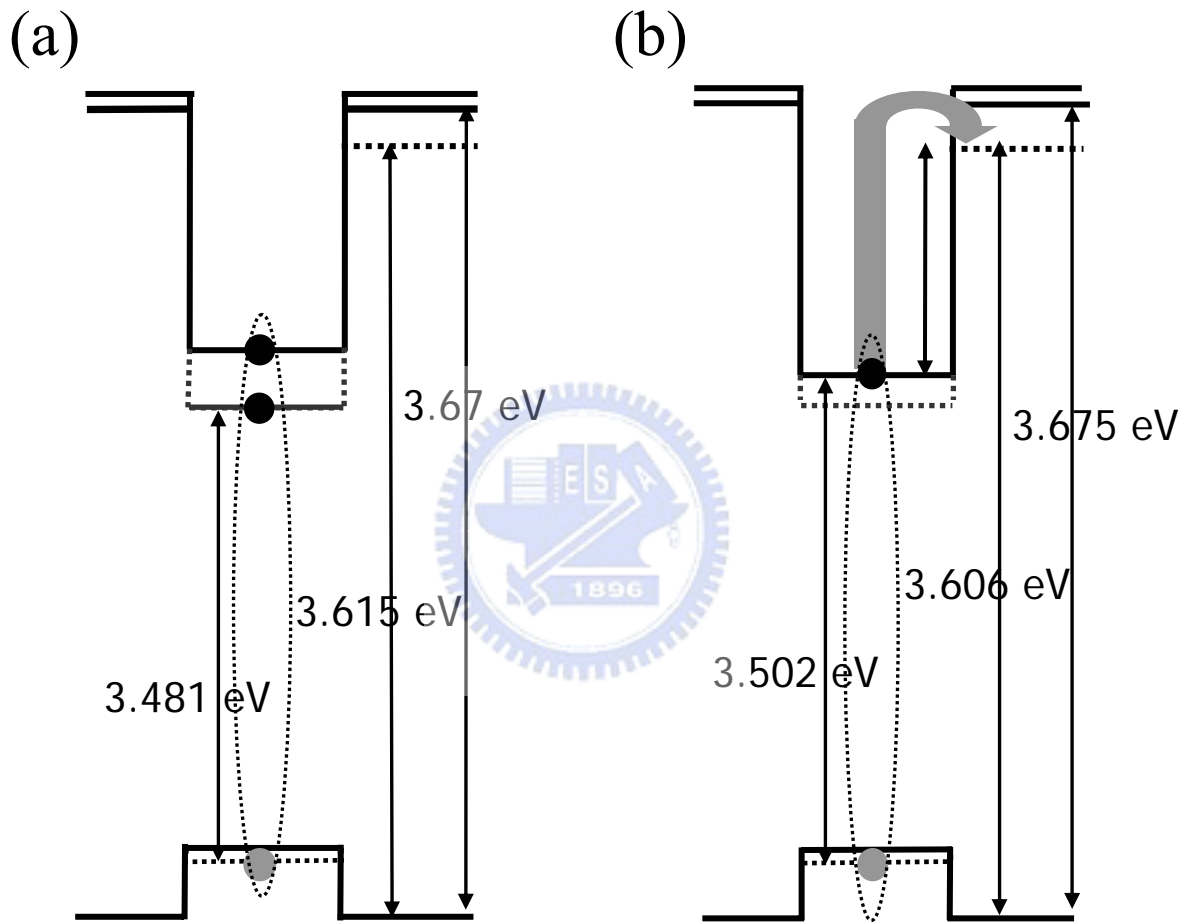


Fig. 5-13 Schematic band diagrams of GaN QDs with height of 8.5 nm (a) 10 K and (b) >100 K.

Chapter 6 Optical Properties of InN Nanodots

Recently, a great deal of work has been devoted to elaboration of InN studies, because of its unique properties, such as high theoretical maximum mobility, extremely high peak drift velocity and low energy bandgap in the III-nitride system [1-3]. Besides, the use of InN and its alloys with GaN and AlN can extend the emission wavelength of nitride-based materials from ultraviolet to near-infrared spectral range, making it very suitable for the fabrication of light emitting devices operating in optical communications wavelengths, 1.3-1.55 μm , and visible range. Among all III-nitride semiconductors, InN remains one of the least studied materials, due mainly to the difficulty in growing high-quality epitaxial film because of the low dissociation temperature and the extremely high vapor pressure of nitrogen for InN, as compared with those for AlN and GaN [4-6]. With the rapid progress in epitaxial growth techniques, remarkably improved InN film, with high carrier mobility ($> 2000 \text{ cm}^2/\text{V}\cdot\text{s}$) and low background concentration ($< 10^{18} \text{ cm}^{-3}$), can now be realized by the uses of molecular beam epitaxy (MBE) [7]. Recent advances further indicated that nanoscale InN dots with controllable size and density can be synthesized on GaN using MOVPE. This kind of nanoscale InN dots, after proper capping with GaN or AlN lowering huge confinement energy is a very promising system for various practical applications. However, systematic study of the emission properties of embedded InN dots in GaN or AlN is still absent; only one report addressed on the emission properties of the InN dots encapsulated by SiO_2 [8].

In this chapter, we report the photoluminescence (PL) properties of embedded InN dots in GaN. A continuous blueshift in the emission energy of the InN dots was observed as the average dot height was reduced to less than 12 nm, ascribing primarily to the size quantization effect. Temperature-dependent measurements show

that the PL peak energy of the InN dots is almost insensitive to the temperature, indicating the localization of carriers in our InN dot structure. Finally, a reduced quenching of the PL from the dots was observed, which implying good emission properties for our embedded InN dots.



6-1 Experimental details

The InN dots were grown on GaN/sapphire (0001) at a temperature varied from 600 to 750 °C by pulsed mode MOCVD growth technique using trimethylgallium (TMGa), trimethylindium (TMIn) and NH₃ as source materials. The gas flow sequence for pulsed mode growth technique, if not mentioned elsewhere, basically consists of four steps: 20-sec TMIn+NH₃ growth step, 20-sec NH₃ source step and the intervened 10-sec purge steps in between. During the growth step, the mole flow rates of TMIn and NH₃ are 1.53×10^{-5} and 8.04×10^{-1} mol/min, respectively. It is worth to mention that during 20-sec TMIn source and 10-sec purge steps an amount of NH₃ (4.46×10^5 μmole/min) is also introduced intentionally in order to suppress the re-evaporation of adsorbed nitrogen atoms. Moreover, we also grow the InN dots by conventional MOCVD method, in which the TMIn and NH₃ flow rate are kept constant at 1.53×10^1 and 4.46×10^5 μmole/min, respectively. The total growth time for InN dots was 2 min. After the growth of InN dots, the substrate temperature was then decreased under a continuous flush of NH₃ gas for the growth of a 35 nm-thick GaN cap layer. For comparison, we also performed bulk InN growth (500 nm) on GaN/sapphire (0001) at 625 °C using conventional MOVPE method. Hall measurement on the bulk InN film shows a room-temperature mobility of 1300 cm²/V-s with background electron concentration of 8×10^{18} cm⁻³. Photoluminescence (PL) measurements were performed by using the 488-nm line of an argon-ion laser as an excitation source. The PL signals were analyzed by a 0.5-m monochromator and detected by an uncooled InGaAs photodiode with a cut-off wavelength at 2.05 μm.

Table 6-1: *The detail growth conditions of InN dots on GaN films by pulsed mode growth technique.*

	Time (min)	Temperature (°C)	Pressure (mbar)	NH ₃ (mol/min)	TMGa (mol/min)	TMIn (mol/min)
Desorption	10	1120	200	-	-	-
Nucleation	4	520	800	1.79×10^{-1}	2.21×10^{-5}	-
Annealing	3	1120	200	8.93×10^{-2}	-	-
GaN	60	1120	200	1.79×10^{-1}	8.84×10^{-5}	-
InN dots (In step)	5~20 (sec)	600~750	200	4.41×10^{-1}	-	1.53×10^{-5}
Purge	10 (sec)	600~750	200	4.41×10^{-1} - 8.04×10^{-1}	-	-
InN dots (NH ₃ step)	20 (sec)	600~750	200	8.04×10^{-1}	-	-
Purge	10 (sec)	600~750	200	8.04×10^{-1} - 4.41×10^{-1}	-	-

6-2 Growth temperature of InN dots

To verify the growth temperature effect on InN dot density, we changed the growth temperature from 600 to 750 °C. Fig. 6-1(a)-(f) shows the AFM images of pulsed-mode-grown InN dots at six different substrate temperatures, namely 600, 625, 650, 700, 720, and 750°C, respectively. For comparison, the AFM images of conventional MOCVD grown InN dots at 600, 650, 700, 715, 730, and 750°C are also depicted in Fig 6-2(a)-(f), respectively. The InN dots density as a function of reciprocal temperature is shown in Fig. 6-3. As anticipated, the dots density depends greatly on the substrate temperature. There are two distinct regions in our dots density curve, divided by a temperature of $\sim 700^\circ\text{C}$. As can be seen in the Fig. 6-3, the dot density is reduced gradually from 1×10^{10} to $2.8 \times 10^8 \text{ cm}^{-2}$ as the temperature is increased from 600 to 700 °C, which then tends to drop sharply with further increasing temperature and eventually become zero, i.e. no dots growth, as the substrate temperature is beyond 750°C (see Fig. 6-1(f) and 6-2(f)). For temperature higher than 700°C, the dots density drops drastically (see Fig. 6-1(e) and 6-2 (e)). This dot density effect is contributed by dots coarsening (see Fig. 6-1(d) and 6-2(c)), driven by the desire of the system to reduce the boundary free energy by transforming small dots into large ones. The process involves both migration of adatoms across terraces and the evaporation of atoms from dots. It is therefore that the dots density should become a much steeper function of temperature.

By referring to the island nucleation mechanism proposed by Robison et al., we learn that the dot density at low temperature is governed by the diffusion capability of adatom, while that at high temperatures is determined predominately by

the re-evaporation rate of adatoms, hence the binding energy of adatom to the adsorbed site. The respective characteristic equations are

$$N_s = N_{0L} \exp(E_d / 3kT) \quad \text{for low temperature, and} \quad (6-1)$$

$$N_s = N_{0H} \exp(E_a / 2kT) \quad \text{for high temperature,} \quad (6-2)$$

where N_s is dot density, N_{0L} and N_{0H} pre-exponential parameters. The E_d activation energy of diffusing In adatom, and E_a binding energy of In adatom to the adsorbed sites were 2.65 ± 0.13 eV and 6.84 ± 0.51 eV, respectively, for InN dots growth on GaN film by pulsed mode growth technique. The value of E_d and E_a are 1.25 eV and 12.3 eV respectively for InN dots growth on GaN film by the conventional MOCVD method. Because of abundant supply of NH_3 in NH_3 step (8.04×10^5 $\mu\text{mole/min}$), result large density of nitrogen dangling bonds on the growing interface, and form the diffusion barrier of the In adatoms in the next growth step in pulsed mode growth scheme. This explains the high E_d diffusion activation energy of In adatom in pulsed mode as compared to conventional MOCVD method. In the high temperature region, the desorption of In adatoms from growing surface is effectively suppressed by the high NH_3 supply in pulsed growth mode. Therefore, the E_a binding energy of In adatom was smaller than the conventional MOCVD method. For InN dot growth, O. Briot et al. also conducted similar experiments in their study. They found the activation energy of diffusion In adatom E_d is 4.19 ± 0.53 eV which is much larger than our results for InN dots prepared either by pulsed mode or conventional MOCVD method. Since they performed InN dot grown at V/III of ~ 30000 , much higher than the V/III ratio (~ 20000) used in our study, this may be the reason causing the discrepancy in diffusion activation energy in the InN dot growth study.

Aside from the dot density, the other dots parameters that concern us are height and diameter. From AFM images (see Fig. 6-1 and Fig. 6-2), we can observe that the InN dots show one kind of size distribution when growth temperature is below 650°C. However, two different InN dots in size was observed when growth temperature above 700°C. Fig. 6-4(a) and (b) show the relation between the average dots height, diameter of pulsed mode growing InN dot against growth temperature. They are assigned as group A and group B. Group A InN dots appeared at low growth temperatures and become vanished at high temperatures higher than 720°C. Group B InN dots appear only at high growth temperatures (i.e. >700°C). As shown in Fig. 6-4(a), the average height of group A dots is increased from 18 to 32 nm as growth temperature is increased from 600 to 650°C, however, further increasing the growth temperature bring into the average height decreased from 32 to 15 nm as the growth temperature increased from 650 to 710°C. In contrast to the InN dots growth by conventional MOCVD method, the average height of group A dots decreased from 35 to 20 nm as increased growth temperature from 600 to 715°C (see Fig. 6-5(a)). For group B of InN dots grown by two kinds of growth method, the average height increased as growth temperature increased from 700 to 730°C as shown in Fig 6-4(a) and 6-5(a). Beside the average height, we also showed the average diameter of InN dots that grown by pulsed mode and conventional MOCVD method in Fig. 6-4(b) and 6-5(b), respectively. Whether group A or group B of InN dots shown the average diameter of InN dots increased as increased growth temperature and finally the InN dots vanishes completely at temperatures above 750 °C.

We also shown the 17 K PL spectra of 600, 625, 650 and 700 °C grown InN dots growth by pulsed mode growth technique in Fig. 6-6(a), (b), (c) and (d),

respectively. As the growth temperature increased from 600 to 700°C, the FWHM of the PL spectra was decreased from 75 to 66 meV (see insert of Fig. 6-6). It is known that the dissociation temperature of InN is about 600 °C, that become the major limiting factor for InN growth. Generally, higher growth temperature leads to high crystalline quality dots. Thus, the high optical quality of InN dots could be obtained by pulsed growth mode under higher growth temperature. Otherwise, the PL peak energy blueshift from 0.78 eV to 0.8 eV as growth temperature decreased from 700 to 600°C. However, no obvious peak energy shift was observed between 650 and 700°C growth sample. In contrast to our result, the PL peak energy of InN bulk shifted to higher energies as the growth temperature rose was reported by T. Matsuoka et al. Until now, we can't clearly indicate the main effect that caused the PL peak energy shift for the different growth temperature of InN dots.

In order to obtain smaller InN dots, we thus performed another series of InN dots growth on GaN at 700°C by decreasing the TMIn exposure time in pulsed growth mode, with all the other growth parameters kept the same during the growth. Figure 6-7 shows the AFM images for films grown at different TMIn exposure times of 20, 15, 10, 7, 5 and 3 s per cycle. The resulting variation of InN dots height and diameter are also shown in Fig. 6-7. The average dots diameter and height are decreased from 300/23 to 70/6.5 nm as the TMIn exposure time decreased from 20 to 3 sec/cycle.

6-3 Photoluminescence (PL) Spectra of InN Nanodots

Table 6-2 summarizes the quantitative structural properties and emission energies of InN QDs and bulk samples. The samples studied in this work consist of 32/255, 24/210, 18/180, 12/130 and 6/70 nm/nm InN dots where the size is listed as height/diameter with a size distribution estimated $\sim 15\%$. The aspect ratio, assigned as height/diameter, ranging from $\sim 1/8$ to $1/12$ and descending with decreasing dot thickness. The AFM images of InN dots in this study are also shown in Fig.6-8.

The PL spectra for the capping InN dots of different sizes, as well as the bulk InN film, measured at $T= 17$ K are shown in Fig. 6-9. The PL spectrum for the InN film shows a peak energy at 0.77 eV, with a full width at half maximum (FWHM) of 69 meV. This emission energy is somewhat higher than the reported bandgap energy of 0.69 eV, [9] indicating a strong Burstein-Moss effect due to the presence of high electron concentration in the film. For the InN dots, a pronounced blueshift in the PL peak energy with the decreasing dot height can be observed. The peak energies shift systematically from 0.78 to 1.07 eV as the average dot height was reduced from 32.4 to 6.5 nm. Such a large shift in the emission energy may be indicative of size quantization effect of the InN dots. We have used a simple effective mass approximation to estimate the quantization effect. Because of the small aspect ratio (height/diameter < 0.13) of our InN dots, only the quantization effect along the growth (z) direction is considered. Since the band offset between InN and GaN is quite large, the confinement energy can be estimated using $E = (\pi^2 \hbar^2 / 2d^2)(1/m_{e,z} + 1/m_{h,z})$, [10] where d is the dot height, and $m_{e,z}$ ($m_{h,z}$) is the effective mass of electrons (holes) in InN along z -direction. The calculated results are depicted in the inset of Fig. 6-9. In our calculations, the effective mass of

holes was set to be $m_{h,z} = 0.1 m_0$, while both $m_{e,z} = 0.042 m_0$ and $0.07 m_0$ were tested for the electron's effective mass. In both cases, the calculated curves agree well with the experimental data.



6-4 Temperature Dependent of PL Spectra of InN Nanodots

To gain more information on emission properties of the InN dots, temperature-dependent PL were investigated and were compared with those of bulk InN film. In Fig. 6-10, the measured PL peak energies for the bulk film as well as the dots of 24-nm height as a function of temperature are displayed. In this figure, we also show the temperature-induced band-gap shrinkage for the InN bulk deduced from the Varshni empirical formula, [11] $E(T) = E_0 - \alpha T^2 / (\beta + T)$, with E_0 as a parameter and using $\alpha = 5.71 \times 10^{-4}$ eV/K and $\beta = 900$ K reported in Ref. 7. For the bulk InN film, the measured peak energy follows very well with the Varshni-type band-gap shrinkage, except for $T < 90$ K. The deviation at low temperature implies that the InN film may exhibit some localized states arising possibly from the band-tail states due to the presence of the background impurities.

More interesting results are observed for the 24 nm height InN dot sample. We found that the measured PL peak energy is less sensitive to the temperature, in contrast to the Varshni-type behavior of the bulk sample. Instead, the InN dot sample displays a so-called “S-shaped” energy shift [12-15]: it redshifts in the range of $T < 110$ K, blueshifts slightly for $T = 110-190$ K, and then redshifts again with the further increasing temperature. If the energy shift for the bulk material is considered as a reference, the observed S-shaped energy shift for the InN dots corresponds to a blueshift of about ~ 40 meV counterbalancing the temperature-induced band-gap shrinkage.

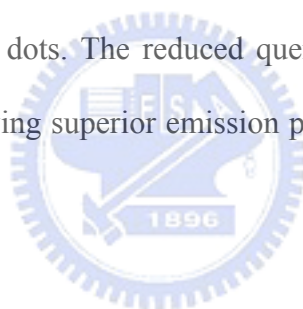
This kind of S-shaped energy shift has been observed in Ga-rich InGaN quantum wells (QWs) and was usually explained by the filling of localized/band-tail states, [16-17] as well as the screening of polarization fields by the photogenerated and/or

thermally released carriers. [18] In the case of our InN dots, the lateral sizes are quite large so that such large dots can still be regarded as a QW-like system. This suggests that a similar *S*-shaped behavior can be expected for the large InN dots, resembling those observed in InGaN QWs. However, since the embedded InN dot system itself is a rather complex material system, the origins of carrier localization/delocalization in the InN dots with temperature are still not clear at present stage. Additionally, whether there exists a wetting layer in our InN dots/GaN ensemble, as channels for carrier transfers among nearby dots, is still an issue needed to be explored.

The carrier localization effect in the InN dots is further confirmed by the reduced thermal quenching of the PL from the dots. Figure 6-11 shows an Arrhenius plot of the integrated PL intensity for the InN dots of 24-nm height and the bulk film. It clearly displays a reduced thermal quenching of the PL from the dots. The thermal activation energy for the InN dots was determined to be $E_a \sim 73$ meV, significantly larger than the value of $E_a \sim 43$ meV for the bulk, indicating a stronger localization of carriers in the dots. This also suggests that the PL-quenching behaviors can be mitigated by the embedded InN dot structures, due not only to the stronger localization effect, but also to the reduced nonradiative centers at the InN/GaN heterointerface after proper capping with GaN.

6-5 Conclusions of Optical Properties of InN Nonodots

In summary, we have investigated the PL properties of MOVPE-grown InN dots capped with GaN. Size-tunable emission energy was observed at the first time in our InN dot samples (i.e. the peak energies shift systematically from 0.78 to 1.07 eV as the average dot height was reduced from 32.4 to 6.5 nm). Temperature-dependent PL measurements showed that the PL peak energies of the InN dots are less sensitive to temperature (~ 7 meV between 17 to 300K), as comparing with that of bulk film (~ 40 meV between 17 to 300K), indicating the localization of carriers in the dots. The thermal activation energy for the InN dots was determined to be $E_a \sim 73$ meV, significantly larger than the value of $E_a \sim 43$ meV for the bulk, indicating a stronger localization of carriers in the dots. The reduced quenching of the PL from the InN dots was also observed, implying superior emission properties for our embedded InN dots.



References

- [1] V. W. L. Chin, T. L. Tansley, and T. Osotchan, *J. Appl. Phys.* 75, 7365 (1994).
- [2] B. E. Foutz, S. K. O'Leary, M. S. Shur, L. F. Eastman, *J. Appl. Phys.* 85, 7727 (1999).
- [3] Ashraful Ghani Bhuiyan, Akihiro Hashimoto, and Akio Yamamoto, *J. Appl. Phys.* 94, 2779 (2003).
- [4] J. W. Trainer and K. Rose, *J. Electron. Mater.* 3, 821 (1974).
- [5] Hai Lu, William J. Schaff, Jeonghyun Hwang, Hong Wu, Wesley Yeo, Amit Pharkya, and Lester F. Eastman, *Appl. Phys. Lett.* 77, 2548 (2000).
- [6] Ming-Chih Lee, Heng-Ching Lin, Yung-Chung Pan, Chen-Ke Shu, Jehn Ou, Wen-Hsiung Chen, and Wei-Kuo Chen, *Appl. Phys. Lett.* 73, 2606 (1998).
- [7] J. Wu, W. Walukiewicz, W. Shan, K. M. Yu, J. W. Ager III, S. X. Li, E. E. Haller, Hai Lu, and William J. Schaff, *J. Appl. Phys.* 94, 4457 (2003).
- [8] S. Ruffenach, B. Maleyre, O. Briot, and B. Gil, *Phys. Stat. Sol. C* 2, 826 (2005).
- [9] Fei Chen, A. N. Cartwright, Hai Lu, William J. Schaff, *J. Cryst. Growth* 269, 10 (2004).
- [10] E. Borovitskaya and Michael S. Shur, in *QUANTUM DOTS*, edited by M. S. Shur (World Scientific, New Jersey, 2002), pp. 94-95.
- [11] B. Monemar, *Phys. Rev. B* 10, 676 (1974).
- [12] Yong-Tae Moon, Dong-Joon Kim, Jin-Sub Park, Jeong-Tak Oh, Ji-Myon Lee, Young-Woo Ok, Hyunsoo Kim, and Seong-Ju Park, *Appl. Phys. Lett.* 79, 599 (2001).
- [13] Y. H. Cho, G. H. Gainer, A. J. Fischer, J. J. Song, S. Keller, U. K. Mishra, and S. P. DenBaars, *Appl. Phys. Lett.* 73, 1370 (1998).
- [14] H. P. D. Schenk, M. Leroux, and P. D. Mierry, *J. Appl. Phys.* 88, 1525 (2000).
- [15] J. Li, K. B. Nam, J. Y. Lin, and H. X. Jiang, *Appl. Phys. Lett.* 79, 3245 (2001).
- [16] P. G. Eliseev, P. Perlin, J. Lee, and M. Osinski, *Appl. Phys. Lett.* 71, 569 (1997).
- [17] P. Perlin, V. Iota, B. A. Weinstein, P. Wisniewski, T. Suski, P. G. Eliseev, and M. Osinski, *Appl. Phys. Lett.* 70, 2993 (1997).
- [18] H. Schömig, S. Halm, A. Forchel, G. Bacher, J. Off and F. Scholz, *Phys. Rev. Lett.* 92, 106802 (2004).

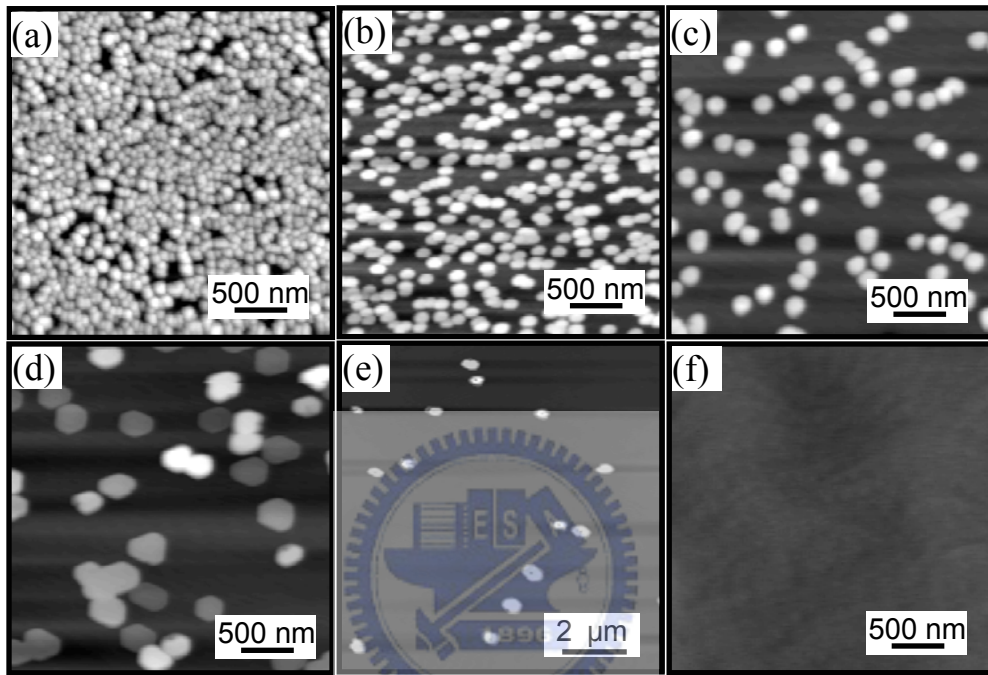


FIG. 6-1 AFM images of InN dots grown at (a)600, (b)625, (c)650, (d)700, (e) 720 and (f) 750 °C.

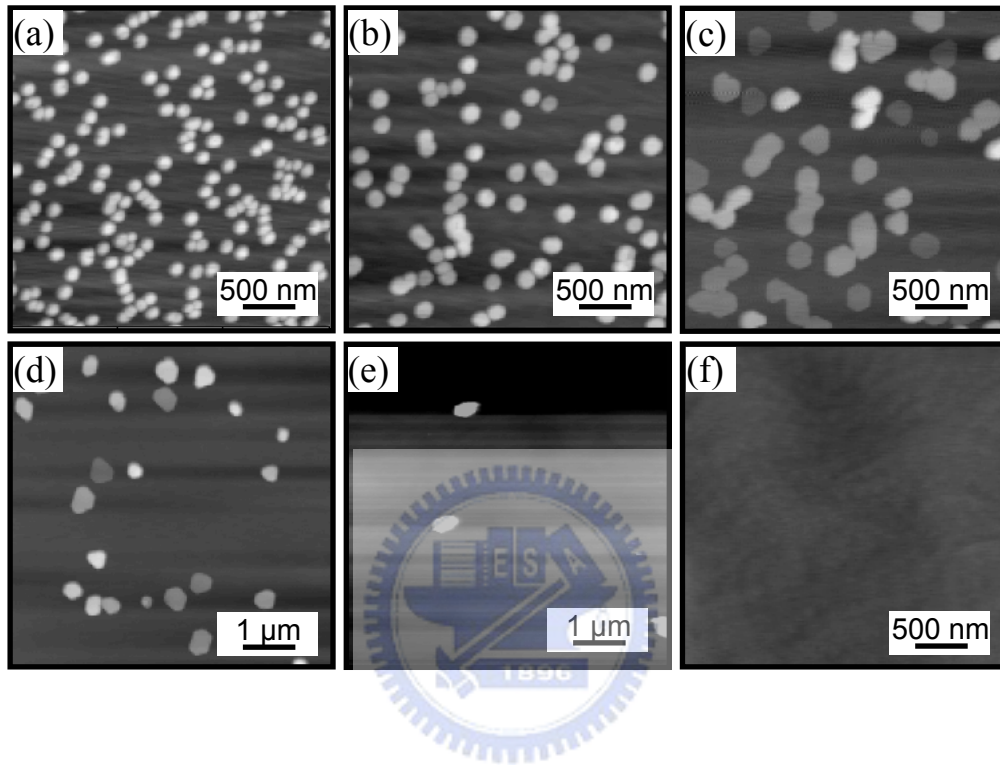


FIG. 6-2 AFM images of InN dots grown by conventional MOCVD at (a)600, (b)650, (c)700, (d)715, (e) 730 and (f) 750 °C.

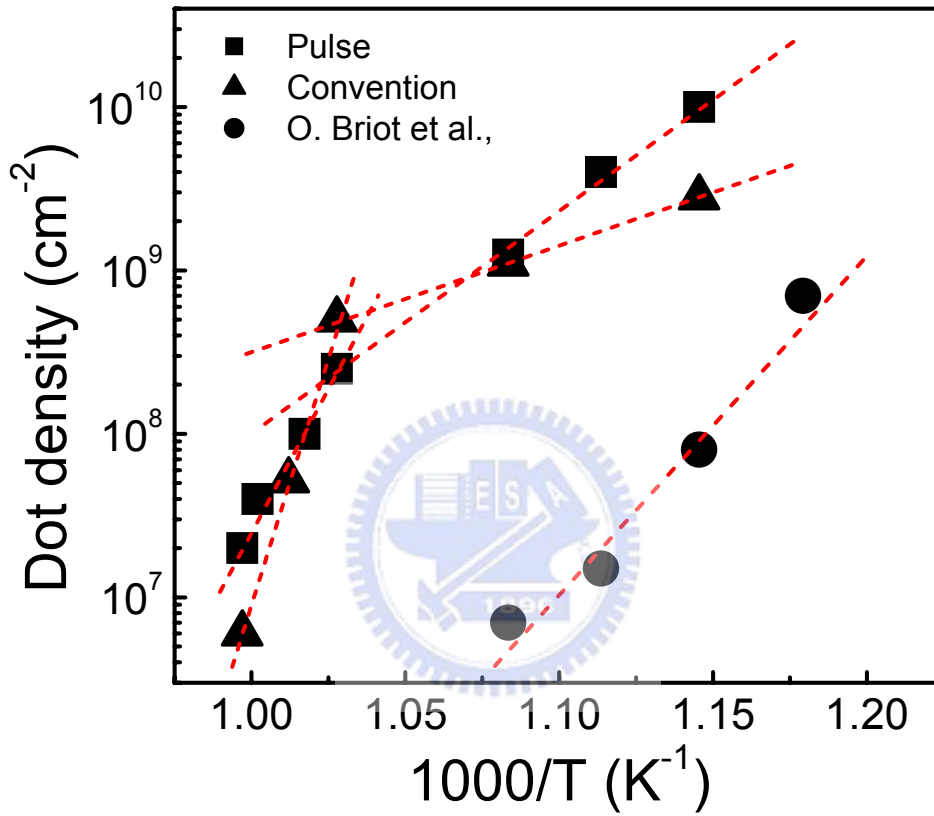


FIG. 6-3 The QDs density depicted as a function of reciprocal temperature.

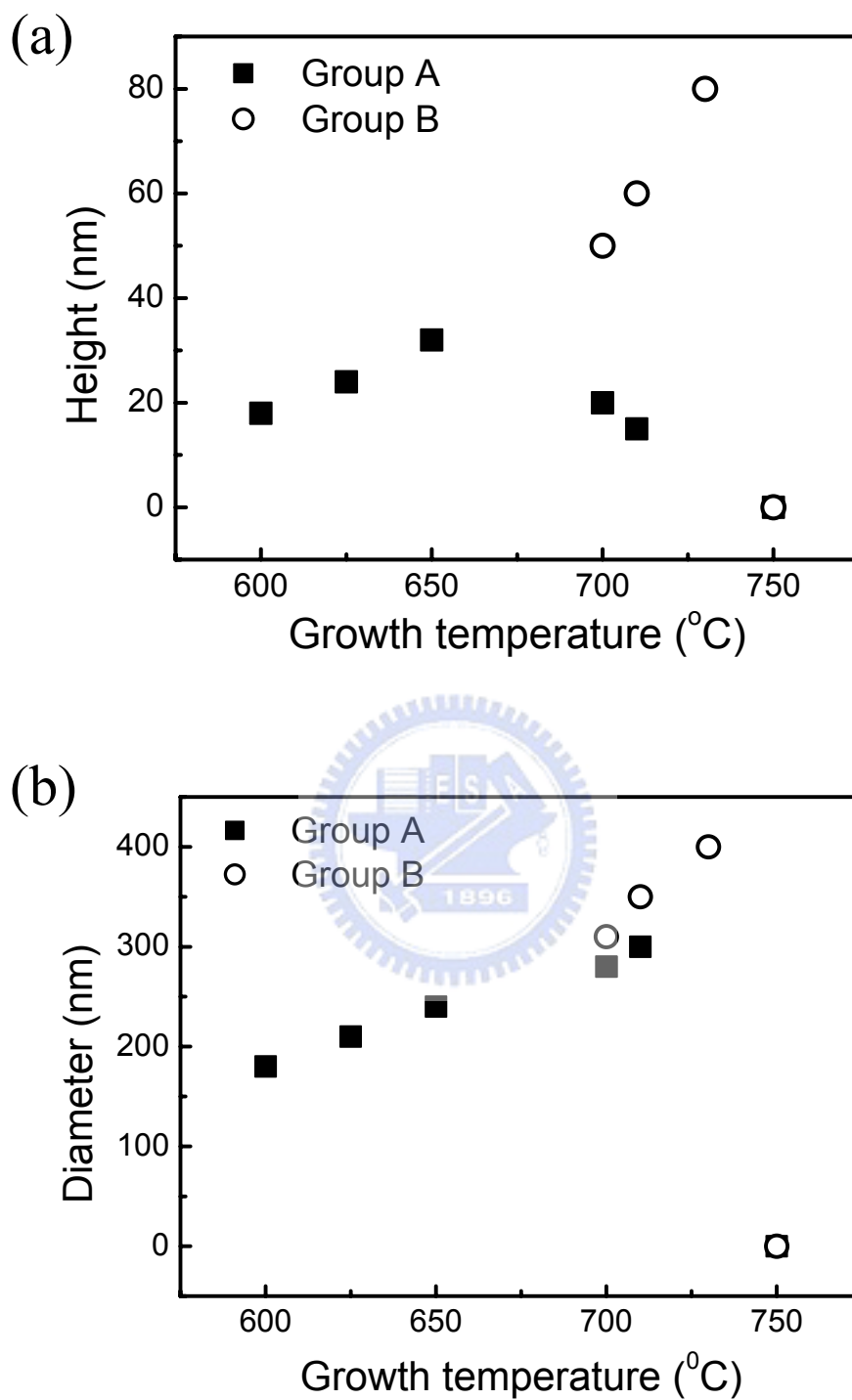


Fig. 6-4 Dependence of (a) average height and (b) average diameter of InN dots on growth temperature (by pulsed growth mode).

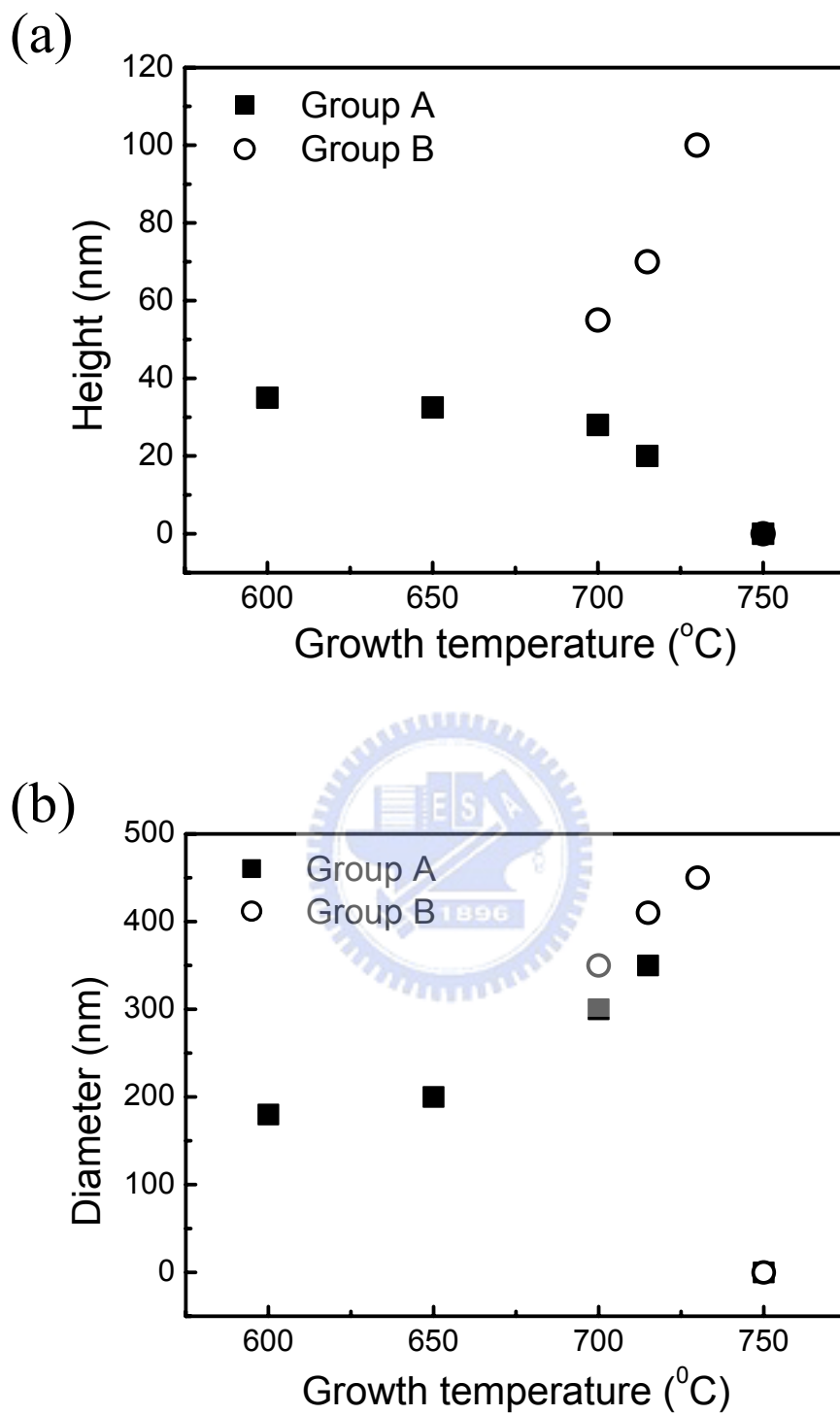


Fig. 6-5 Dependence of (a) average height and (b) average diameter of InN dots on growth temperature (by conventional MOCVD).

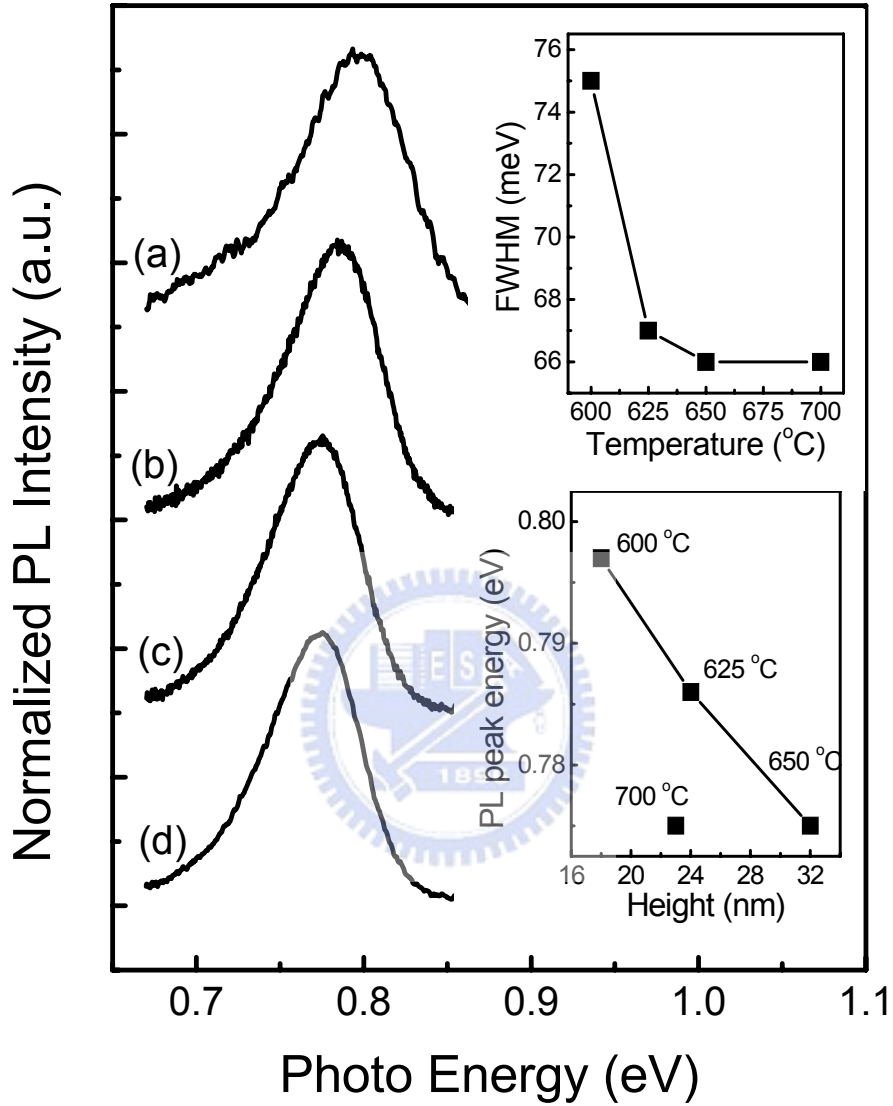


Fig. 6-6 The 17 K PL spectra of 600, 625, 650 and 700 °C growth temperature of InN QDs. Top insert shows the relation between FWHM and growth temperature, and down insert shows the relation between PL peak energy and dots height.

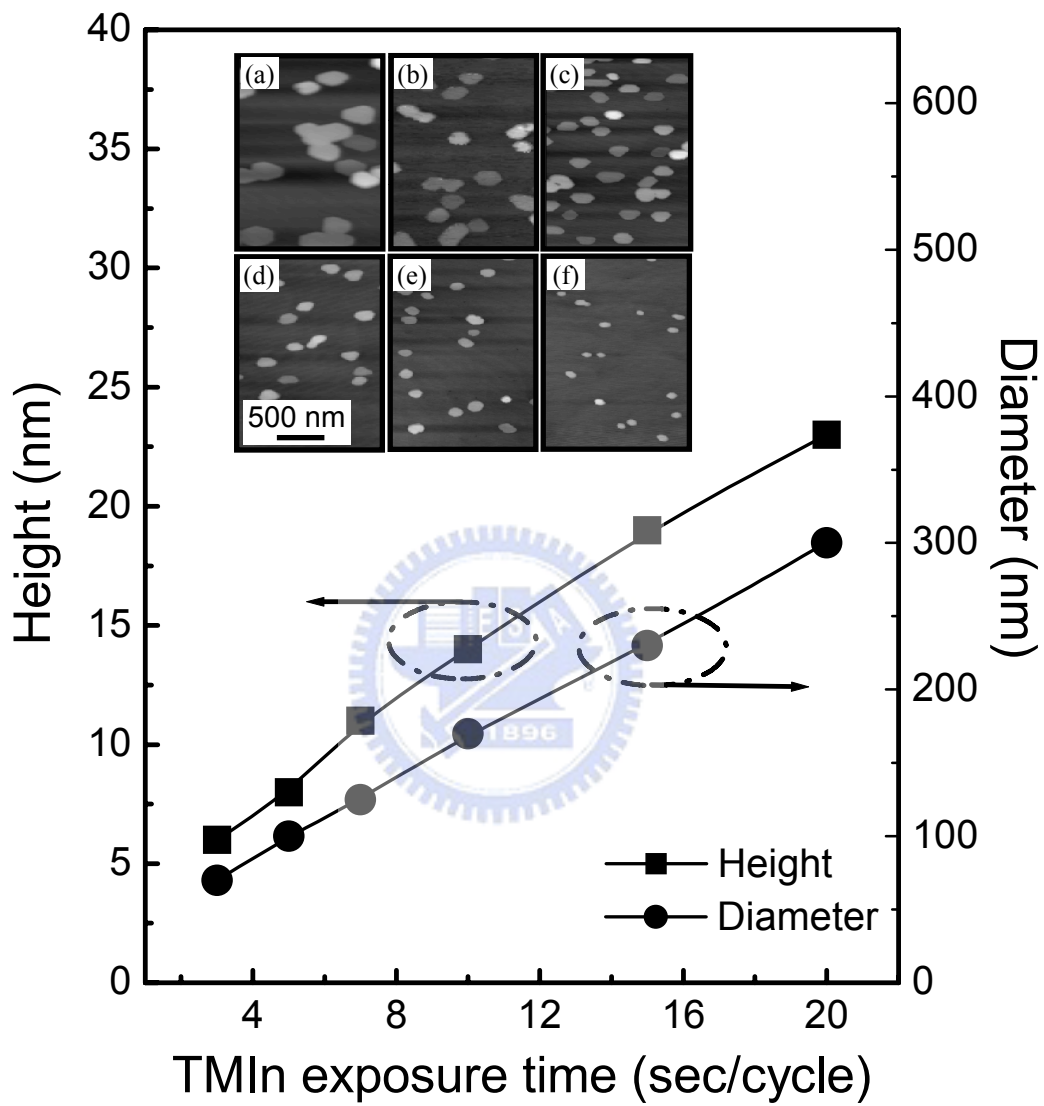


Fig. 6-7 Dependence of average diameter and height of InN dots on exposure time of TMIn.

Table 6-2: The quantitative structural properties and emission energies of InN QDs and bulk samples.

Sample	Average height (nm)	Average diameter (nm)	PL emission energy (eV)
InN bulk			
A	32.4±4.4	255	0.775
B	24.2±2.5	210	0.785
C	18.5±1.8	180	0.797
D	12.4±1.2	130	0.82
E	6.5±0.8	70	1.07

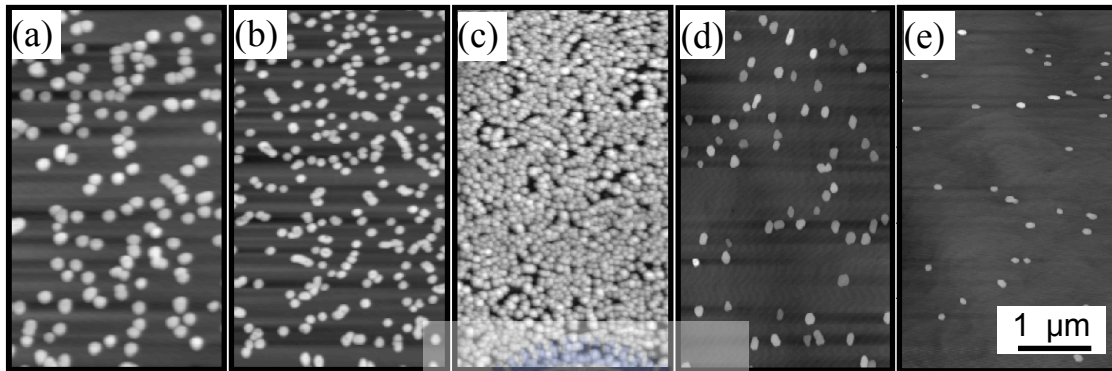


FIG. 6-8 AFM images of InN dots with height of (a) 32.4 nm (b) 24.2 nm (c) 18.5 nm (d) 12.4 nm (e) 6.5 nm.

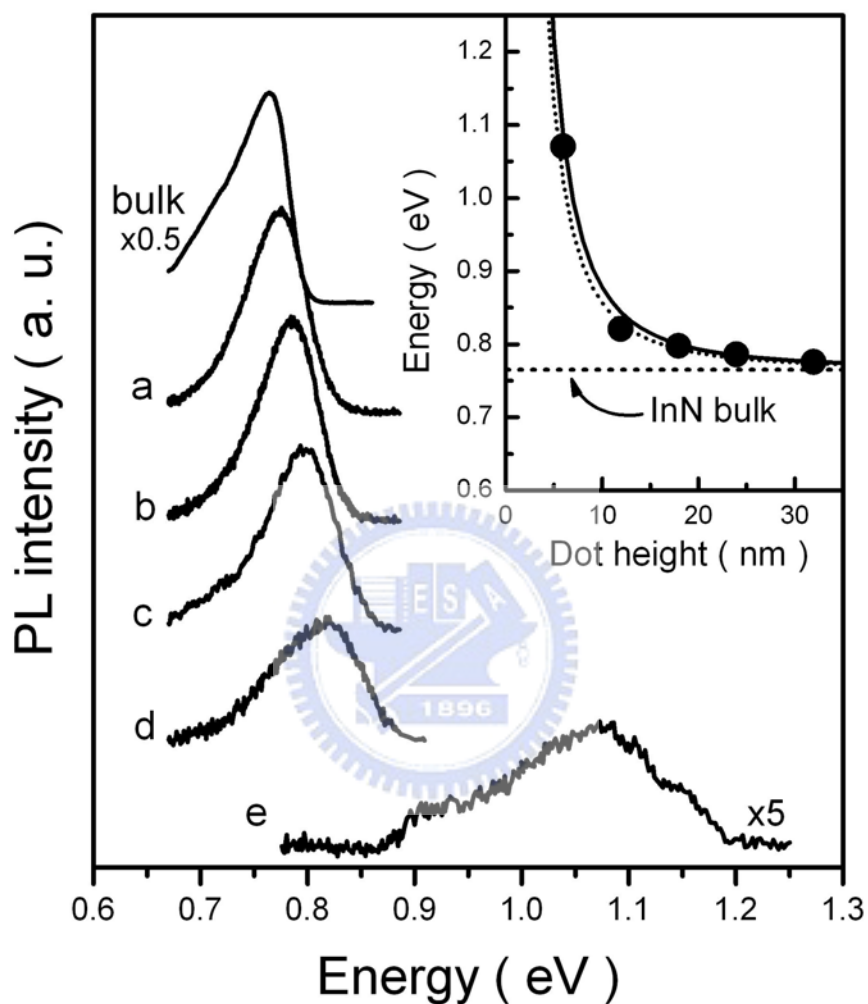


FIG. 6-9 17 K PL spectra of InN bulk and InN dots with height of (a) 32.4 nm (b) 24.2 nm (c) 18.5 nm (d) 12.4 nm (e) 6.5 nm. The insert shows the relation of peak energy and dots height. The electron effective mass of $0.042m_0$ (solid line) and $0.07m_0$ (dotted line) were assumed in this calculation.

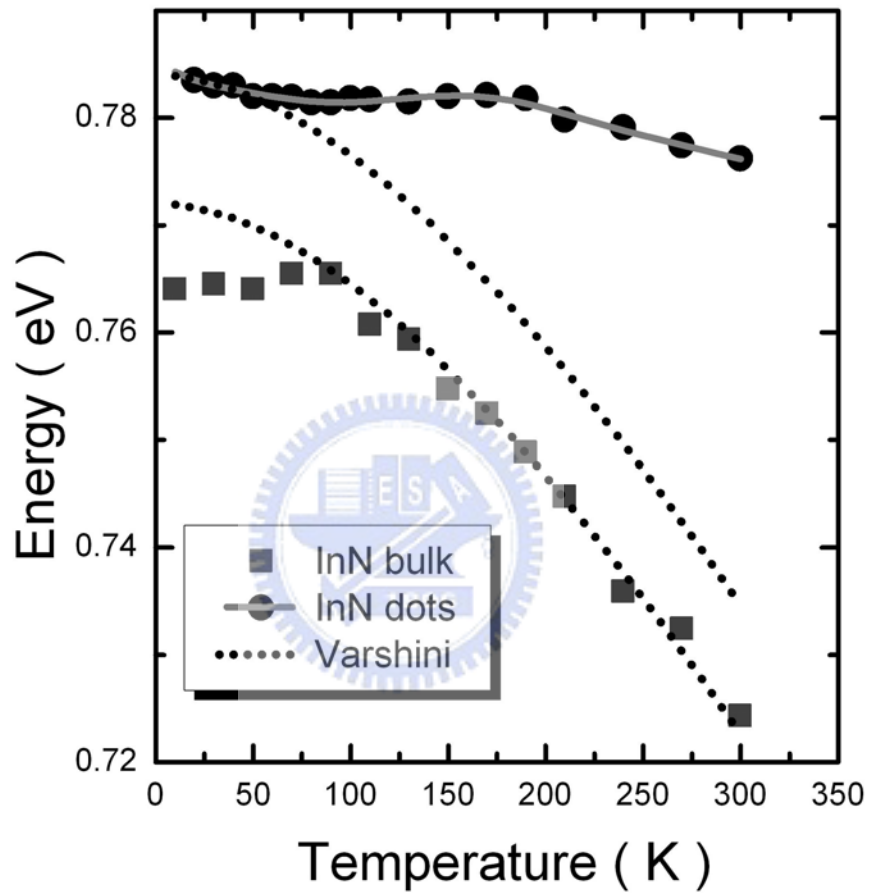


FIG. 6-10 Temperature dependence of the PL peak energy of InN dots and bulk samples.

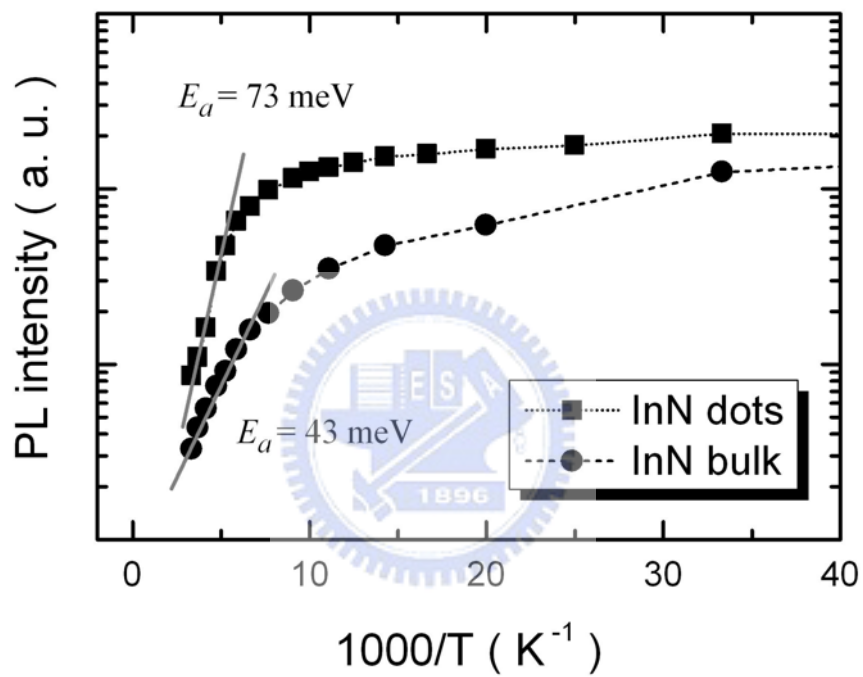


FIG. 6-11 Temperature dependence of the PL integrated intensity of InN dots and bulk samples.

Chapter 7 Enhanced photoluminescence of InN dots by FME

Recently, a great deal of work has been devoted to elaboration of InN studies, because of its unique properties such as high theoretical maximum mobility, high peak drift velocity and low energy bandgap (~ 0.69 eV) [1-3]. Consequently, the use of InN and its alloys with GaN and AlN can extend the bandgap of nitride-based LEDs from approximately 6.2 to 0.69 eV, making it very suitable for fabrication of light emitting devices covering wide range of emission wavelengths from ultraviolet to near infrared region. Additionally, rather interesting PL result is observed in InN film. Our early study shows that the PL peak energy of InN dots exhibits almost no shift as the measured temperature changed from 10 to 300 K [4]. Such a characteristic would benefit to fabricating 1.3-1.55 μm laser diodes with high wavelength-stability, advantages for optical communications. Despite numerous literatures have been published on discussing its bandgap and relevant physical properties, few attentions have been paid on InN dot growth. Up to now, the InN dot growth is mainly conducted by way of conventional growth manners using either molecular beam epitaxy (MBE) [5-8] or metalorganic chemical vapor deposition (MOCVD) techniques [9,10]. Nevertheless, to our knowledge, no photoluminescence result has been reported yet for MBE-grown InN dot samples, due to possibly the rather low growth temperature associated with such type of dot growth feature. As for MOCVD, the InN dot prepared by conventional method has been reported firstly by Ruffenach et al. [11] They observed a strong blue shift in emission energy from encapsulated nano-scale InN dots, originating fundamentally from the carrier confinement in their quantum size structure. In our previous paper [4], we have demonstrated that the InN dots with good optical quality can be also prepared successfully by a so-called flow-rate modulation epitaxy (FME), modified from MOCVD growth technique, in

which the In and N gas sources were alternately introduced into the growth chamber. In this study, we further investigate the dependence of optical properties, together with dot density and relevant surface morphology and structure as functions of growth temperature and amount of NH_3 background flow which introduced in In source step for our InN dots grown by FME, profound effects were found in this study.



7-1 Experimental details

The InN dots used here were grown on 1 μm -thick GaN buffer layer/sapphire (0001) substrates by FME with six growth cycles. The gas flow sequence for one growth cycle basically consists of four steps: 20-sec TMIn step, 20-sec NH_3 step, intervened with 10-sec nitrogen carrier gas purge in between (Fig. 7-1). The TMIn and NH_3 flow-rate use here were 150 and 18000 sccm for In and N steps, respectively. It is worth to notice that in the TMIn step, a small amount of NH_3 of 1000 sccm flow rate, if not mentioned elsewhere, was also intentionally provided so as to suppress the reevaporation of In atom during the step. The TMIn step here is also referred as growth step, because of the deterministic nature of group III elements in III-V compound growth, and whereas the NH_3 step as annealing step where abundant NH_3 was supply to convert the left unreacted adsorbed In atoms in growth step and reorganize them into InN form. The other growth conditions of InN dots were described in Table 7-1. In this study, several runs of the InN dots grown by conventional MOCVD method were also performed as references. In these cases, the TMIn and NH_3 flow rates during the dot preparations were kept at 150 and 10000 sccm, respectively, with a dot growth time of 2 min., exactly the same TMIn flow rate and the total growth duration of six-cycle TMIn growth steps that employed in our FME dot growth. The PL measurements were performed by using the 488-nm line of an argon-ion laser as an excitation source. The PL signals were analyzed by a 0.5-m monochomator and detected by an InGaAs photodiode with a cut-off wavelength at 2.05 μm . The surface structures were examined by a NT-MDT atomic force microscopy (AFM) system. Imaging was performed in air using noncontact tapping mode with the silicon cantilever.

Table 7-1: *The detail growth conditions of InN dots grown by FME technique.*

	Time (min)	Temperature (°C)	Pressure (mbar)	NH ₃ (mol/min)	TMGa (mol/min)	TMIn (mol/min)
Desorption	10	1120	200	-	-	-
Nucleation	4	520	800	1.79×10^{-1}	2.21×10^{-5}	-
Annealing	3	1120	200	8.93×10^{-2}	-	-
GaN	60	1120	200	1.79×10^{-1}	8.84×10^{-5}	-
InN dots (In step)	20 (sec)	600	200	$0-4.41 \times 10^{-1}$	-	1.53×10^{-5}
Purge	10 (sec)	600	200	$(0-4.41 \times 10^{-1})$ $- 8.04 \times 10^{-1}$	-	-
InN dots (NH ₃ step)	20 (sec)	600	200	8.04×10^{-1}	-	-
Purge	10 (sec)	600	200	8.04×10^{-1} - 4.41×10^{-1}	-	-

7-2 Growth temperature

It is no doubt that the growth temperature is one of the most important parameters in determining the epitaxial growth of film, including the dot growth, we thus perform numbers of FME and MOCVD InN dot growths at different growth temperatures from 550 to 730°C. Figure 7-2 shows the resulted Arrhenius plot of InN dots density as a function of reciprocal temperature. As anticipated, the density of InN dots is very sensitive to the substrate temperature. Despite of different growth

methods, two regions with about the same dividing temperature $\sim 700^\circ\text{C}$ were clearly observed. In the temperature range of $550\text{-}700^\circ\text{C}$, the corresponding dot density tends to decrease gradually from 1.5×10^9 to $3.2 \times 10^8 \text{ cm}^{-2}$ for FME and 7.5×10^9 to $5 \times 10^8 \text{ cm}^{-2}$ for MOCVD with the increasing temperature. Afterwards, both of them decline drastically and eventually become zero, i.e. no dots growth, for temperature beyond 730°C . The obtained average dot height and diameter are listed in Table 1.

By referring to the island nucleation mechanism proposed by Robison et al., [12] we learn that the dot density at low growth temperatures is governed mainly by the diffusion capability of adatom, while that at high temperatures is determined by the adsorption energy of adatom to the adsorbed site. The respective characteristic equations are

$$N_s = N_{0L} \exp(E_d / 3kT) \text{ for low temperatures, and} \quad (1)$$

$$N_s = N_{0H} \exp(E_a / 2kT) \text{ for high temperatures,} \quad (2)$$

where N_s is dot density, N_{0L} and N_{0H} are pre-factors, and E_d and E_a present diffusing activation energy of surface adatoms and adsorption energy needed for them to adsorb the dot islands.

The derived values of adatom diffusion energy E_d and adsorption energy E_a from the dot density curves are 0.7 and 16.4 eV for FME and 1.3 and 12.3 eV for MOCVD, respectively. Comparing to MOCVD, the InN dot growth by FME appears to possess much lower diffusion activation energy, almost half of its opponent, and higher adatom adsorption energy. The low diffusion activation energy in FME suggests that the species of random-walk adatoms on the growing surface due to the feature of alternate injection scheme differ largely from conventional MOCVD. For MOCVD

InN growth, it is commonly accepted that the adatoms that migrate on the growing surface are most likely the In-N molecules or its complexes, formed favorably via heterogeneous reaction in continuous growth manner, which diffuse a short distance before their incorporation into the solid. On the other hand, for FME InN growth, if the growth conducted in In growth step is totally absent from reactive nitrogen species, highly mobile In adatoms are easily formed on the surface to control the deposition. Since in this series of experiments, one tenth of NH_3 flux that used in MOCVD was selected as the background flow in FME during TMIn growth step, it is believed that the surface migration adatoms are combination of the individual In atoms and In-N molecules or its complexes. Such a compound effect will certainly make the surface adatoms to migrate a longer distance before they meet each other to form new islands or be caught by existing islands. This explains for the sparser dot density observed in FME-grown InN dot film than that by MOCVD at low temperatures.

In regard to the high temperature regime, as mentioned earlier there appears to have steeper functions of dot density on temperature. Two likely mechanisms may account for this. One is InN dissociation corresponding to a fast N escape from InN, the other involves fast In evaporation from the growing surface [13]. Although under vacuum environment the dissociation of InN ($\sim 600^\circ\text{C}$) [14,15] occurs much earlier than that of In evaporation on InN surface ($\sim 670^\circ\text{C}$), the onset of dissociation temperature in reality is dependent to a great extent on the given growth conditions, such as chamber pressure, surface plane of substrate, growth rate, and incoming TMIn and NH_3 source fluxes employed during sample preparation. If the dissociation does govern the growth at high temperatures, starting from 700°C the surface would be covered with lots of In droplets, caused by large quantities of N loss leaving exposed

In atoms on the surface to form droplets, which is expected to become less severe with increasing temperature because of the increasing active N supply simply due to the improved cracking efficiency of NH_3 . Since neither no In droplets at 700°C nor reduction of droplet density at higher growth temperatures were observed, we speculate the evaporation of excessive In adatoms is the most probable reason that responsible for sharp decline in dot density in our samples at high temperatures. Such an argument is also confirmed by the fact of steep slope in In growth efficiency in this temperature regime, as depicted in the inset in Fig. 1. One can see in the figure, the In growth efficiency drop quickly for growth temperatures above 700°C .

The resulted 10-K PL spectra of these uncapped InN dots grown by both FME and MOCVD from 550 to 730°C were displayed in Figs. 7-3(a) and (b), respectively, the peak energy and FWHM as functions of growth temperature were also presented in the figure. The data of InN dot sample grown by conventional MOCVD at 550°C is not shown here because no measurable signal can be attained. As can be seen in the figure, the peak energy for MOCVD sample decreases linearly from 0.79 to 0.75 eV with raising temperature (see the inset), whereas that for FME is generally lower than MOCVD-grown samples at low growth temperatures and approaches approximately the same peak energy as the MOCVD sample grown at 730°C . Nonetheless, they all deviate enormously from the reported 10-K InN bandgap, ~ 0.69 eV [16], reflecting strong Moss-Burstein effect [17], stemming primarily from high carrier concentration, existed in all of our samples. The character of lower PL energy associated with FME samples indicate better quality InN dot with lower background doping can be achieved by using FME, particularly at low growth temperatures. As far as FWHMs of PL spectra are concerned, as anticipated a too high or too low growth temperature

in the study would lead to a broader linewidth in the emission spectrum. The FWHM values lie in the range of 63 – 90 meV, with minimum values, 63 meV for FME and 71 meV for MOCVD, occurred at 600 and 700°C, respectively. Knowing that the PL linewidth is one of the key parameters in gauging the material qualities, the optimal growth temperature for InN dot growth by FME here is determined to be ~600°C, considerably lower than that, 700°C, in conventional growth method.



7-3 NH_3 flow rate in TMIn flow period

To verify the influences of NH_3 background flow in TMIn step on InN dot growth by FME, we subsequently conducted another series of experiments at a temperature of 600°C . Figs. 7-4 shows the dot density and their AFM images prepared at different NH_3 background flows varied from 0, 500, 1000, 5000 and 10000 sccm, respectively. It is observed that the FME-grown InN dots density increases gradually from $6 \times 10^8 \text{ cm}^{-2}$ to $1 \times 10^{10} \text{ cm}^{-2}$, nearly sixteen-fold in value with increasing NH_3 background flow during the growth step. The increasing dot density with NH_3 background flow reflects clearly that the migration length of surface adatoms is decreased about by a factor of four, assuming migration length $\lambda_c = N_s^{-1/2}$ is valid [17], where N_s is the dot density of the islands and $N_s^{-1/2}$ represents the mean distance between nearest-neighbor islands. We would like to point out here, when $\text{NH}_3=10,000$ sccm background is used, which is exactly the same value utilized in our conventional InN dot growth, the FME deposition in this case is more like the conventional method except chopped by nitrogen purged step. Consequently, by tuning the NH_3 background flow in FME InN dot depositions the growth here basically undergo growth conditions from a case that is totally free from active nitrogen ambient to strong N-rich growth conditions. Under N-rich conditions, the adsorbate-surface interactions are predominantly realized by In-N bonds. The diffusion barriers on these surfaces are thus mainly characterized by breaking the strong cation-anion bonds. As a consequence, high diffusion barriers and hence low adatom diffusion mobilities are resulted. On the contrary, under entirely NH_3 -free indium growth step in FME, the surface exhibits a metal-like character, because of weak binding energy of the In-In bond, the In adatoms move more freely on the

In-terminated surface, giving rise to a marked decrease in dot density in its InN dot film.

Not only the dot density is affected, the change of NH₃ background flow in TMIn growth step also affects greatly the appearance of InN islands. Figures 7-5 show the dot height, diameter and aspect ratio, which defined as ratio of base diameter to height, as functions of the NH₃ background flux. The typical line profiles and AFM images of single individual dots are presented as well in the inset. Except lens-like shape for sample grown at 10,000 sccm NH₃ background, all the other FME-grown InN dots exhibit a disk-like shape, or more accurately, a truncated pyramid with a hexagonal base, with base diameter a few times larger than the height. Regardless of the viewpoint of aspect ratio, dot diameter or height, their curves all show two distinct regions in the figure, divided by a NH₃ background flow of ~1,000 sccm, which are assigned as N-rich and In-rich regions, respectively. Under N-rich growth environments, the aspect ratios are low, ranged from 3.4 to 5.1, close to a value of 2.8 for non-truncated hexagonal InN pyramid ($\alpha=65^\circ$) [18]. In this regime, a slow increase in aspect ratio is observed with decreasing NH₃ background; the same growth tendency is also observed in dot height and diameter. In contrast, under In-rich conditions an abrupt increase feature is observed for all of the aforementioned dot geometry parameters. The aspect ratio jumps to 7.0 when NH₃ background drops completely to zero, indicating faster rising in lateral growth rate with respect to vertical growth rate for InN dots growth in this area.

Based on above observations, it can be concluded that the FME depositions under In-excess conditions here are thermodynamically controlled, where the surface adatoms are mainly the In adatoms that move on metallic surfaces. Higher adatom

mobility under more In-rich regime will make the surface adatoms traveling longer distances, hopping over the step edge barriers of islands to find their energetically most stable sites, which resulting in higher aspect ratios of the deposited InN nanodots in the films. On the other hand, the depositions under N-rich conditions here are limited mainly by kinetics, where N-terminated surfaces are built and are kinetically stable. These surfaces exhibit higher diffusion barriers and hence significantly reduce In diffusion lengths which drive the In atoms to compile uphill to form low aspect-ratio nanodots. Since faceting is energetically more favorable under more N-rich conditions, hexagonal InN pyramids with a clear facet angle $\alpha=48^\circ$ do occur at a NH_3 background flow of 10,000 sccm in present work.

The 10-K PL spectra of the above InN dots grown by FME and by MOCVD are illustrated in Fig. 7-6. The corresponding PL FWHM and peak energy against background flow are also drawn in the figure. The PL results seem coincide well with the results of dot structure parameters in Fig. 7-5, where N-rich and In-rich regions are allocated previously in accord with their growth behaviors. Not surprisingly, the PL linewidth decreases significantly from 152 to 64 meV as background NH_3 flow is decreased from 10,000 to 1,000 sccm in N-rich growth region, and seems almost unchanged in the so-called In-rich region. The narrowest linewidth, $\sim 63\text{meV}$, occurred at 500 sccm NH_3 background flow, is the best value ever reported for InN nanodots. Beside the variation of PL linewidth, the improvement of PL intensity in In-rich growth region is also astonishing. The PL intensities of InN dot samples grown here are generally higher than in N-rich region. The maximum PL intensity occurred at NH_3 background flow of 500 sccm has a magnitude almost 50 times higher than dots prepared at 10,000 sccm background flow and 15 times higher than MOCVD-grown InN dot sample. Such an improvement in optical quality can be attributed at least

partially to the auto-surfactant effects of In adlayer under In-rich growth conditions, which enhance adatom mobilities, planarize the top surfaces of truncated pyramid islands, and might also lead to reductions of point defects, such as indium vacancies (V_{In}) and indium interstitials (In_i), and stacking defaults in the dots.



7-4 Conclusions of InN Nanodots growth by FME

In summary, comparisons between InN dots grown by FME and by MOCVD have been comprehensively performed in terms of the optical and morphological structure properties. In comparison with MOCVD, the FME InN dots growth in the temperature range of 550-700°C appears to have lower adatom diffusion activation energy (0.7 vs. 1.3 eV) and lower dot density, which gives rise to better optical quality InN dot samples in this region, owing to the enhanced adatom migration mobility in such type of deposition scheme. More interesting results were observed for FME InN dot samples grown with different NH₃ background flows. The samples prepared under low NH₃ backgrounds (<1,000 sccm), hence In-rich growth conditions, generally exhibit narrower and more intense photoluminescence signals than ones prepared under N-rich conditions (>1,000 sccm). For instance, the PL intensity of InN dots grown under a NH₃ background flow of 500 sccm is increased by nearly a factor of 50 as compared to that under a NH₃ background flow of 10,000 sccm, where the growth is conducted in the regime of N-rich condition.

References

- [1] V. W. L. Chin, T. L. Tansley, and T. Osotchan, *J. Appl. Phys.* 75, 7365 (1994).
- [2] B. E. Foutz, S. K. O'Leary, M. S. Shur, L. F. Eastman, *J. Appl. Phys.* 85, 7727 (1999).
- [3] Ashraful Ghani Bhuiyan, Akihiro Hashimoto, and Akio Yamamoto, *J. Appl. Phys.* 94, 2779 (2003).
- [4] W. C. Ke, C. P. Fu, C. Y. Chen, L. Lee, C. S. Ku, W. C. Chou, W.-H. Chang, M. C. Lee, W. K. Chen, W. J. Lin and Y. C. Cheng, *Appl. Phys. Lett.* 88, 191913 (2006).
- [5] A. Yoshikawa, N. Hashimoto, N. Kikukawa, S. B. Che, and Y. Ishitani, *Appl. Phys. Lett.* 86, 153115 (2005).
- [6] Lin Zhou, Tao Xu, David J. Smith, and T. D. Moustakas, *Appl. Phys. Lett.* 88, 231906 (2006).
- [7] Y. F. Ng, Y. G. Cao, M. H. Xie, X. L. Wang, and S. Y. Tong, *Appl. Phys. Lett.* 81, 3960 (2002).
- [8] Y. G. Cao, M. H. Xie, Y. Liu, Y. F. Ng, H. S. Wu, and S. Y. Tong, *Appl. Phys. Lett.* 83, 5157 (2003).
- [9] O. Briot, B. Maleyre, and S. Ruffenach, *Appl. Phys. Lett.* 83, 2919 (2003).
- [10] J. G. Lozano, A. M. Sánchez, R. García, D. González, D. Araújo, S. Ruffenach and O. Briot, *Appl. Phys. Lett.* 87, 263104 (2005).
- [11] S. Ruffenach, B. Maleyre, O. Briot, and B. Gil, *Phys. Stat. Sol.(c)* 2, 826 (2005).
- [12] V. N. E. Robinson and J. L. Robins: *Thin Solid Films* **20** (1974) 155.
- [13] Pierre Ruterana, Martin Albrecht, Jörg Neugebauer, in *Nitride Semiconductors Handbook on Materials and Devices*, edited by WILEY-VCH Verlag GmbH (Germany, 2003), p. 247.
- [14] Ming-Chih Lee, Heng-Ching Lin, Yung-Chung Pan, Chen-Ke Shu, Jehn Ou, Wen-Hsiung Chen, and Wei-Kuouka Chen, *Appl. Phys. Lett.* 73, 2606 (1998).
- [15] W. L. Chen, R. L. Gunshor, J. Han, K. Higashimine, and N. Otsuka, *MRS Internet J. Nitride semicond. Res.* 551, W3.30 (2000).
- [16] J. Wu, W. Walukiewicz, W. Shan, K. M. Yu, J. W. Ager III, S. X. Li, E. E. Haller, Hai Lu, and William J. Schaff, *J. Appl. Phys.* 94, 4457 (2003).
- [17] Walukiewicz, W.; Li, S.X.; Wu, J.; Yu, K.M.; Ager III, J.W.; Haller, E.E.; Lu, Hai; Schaff, William, *J. Cryst. Growth* **269**, 119 (2004).
- [18] Ken-ichi Shiramine, Tomohiko Itoh, Shunichi Muto, Tamotsu Kozaki, Seichi

- Sato, J. Cryst. Growth **242**, 332 (2002).
- [19] E. Dimakis, E. Iliopoulos, K. Tsagaraki, Th. Kehagias, Ph. Komninou, and A. Georgakilas, J. Appl. Phys. 97, 113520 (2005).



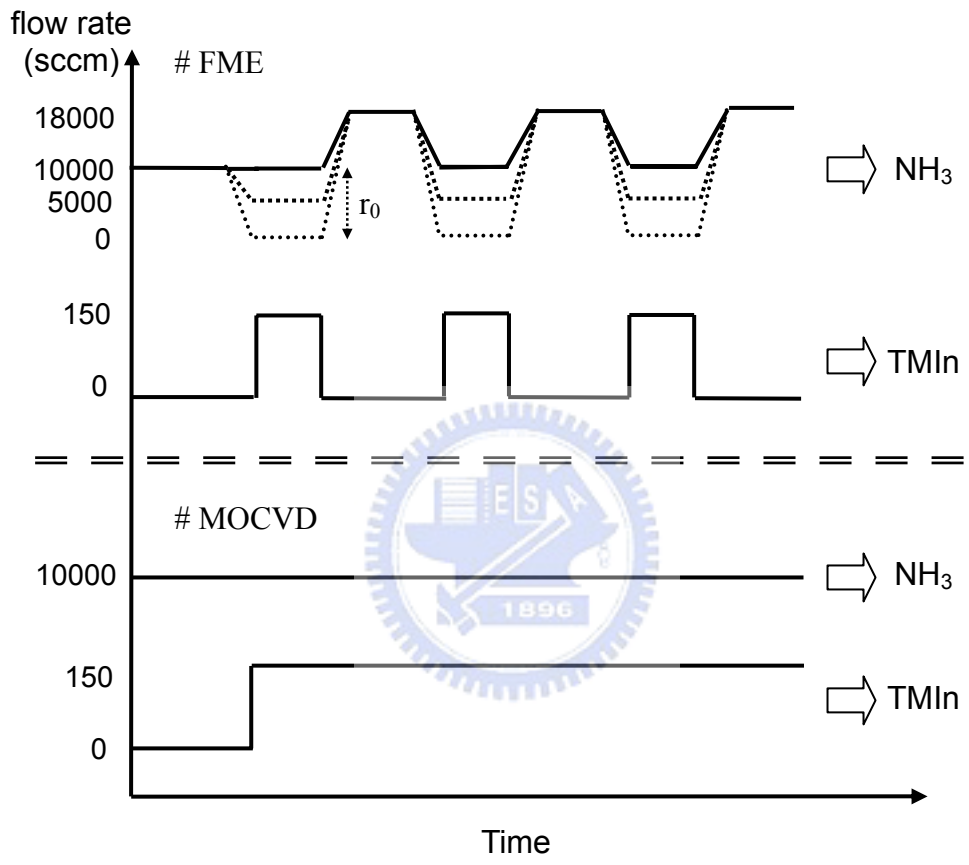


Fig. 7-1 The typical gas flow sequence of the formation of InN dots for FME and conventional MOCVD.

Table 7-2: *The average height and diameter of InN dots grown at different growth temperatures from 550 to 730 °C.*

Method \ H/D	Temperature					
	550 °C	600 °C	650 °C	700 °C	715 °C	730 °C
MOCVD (nm)	13/102	30/154	33/207	36/281	71/413	80/457
FME (nm)	16/151	39/202	35/258	52/226	62/203	84/191

*H/D = Height/Diameter

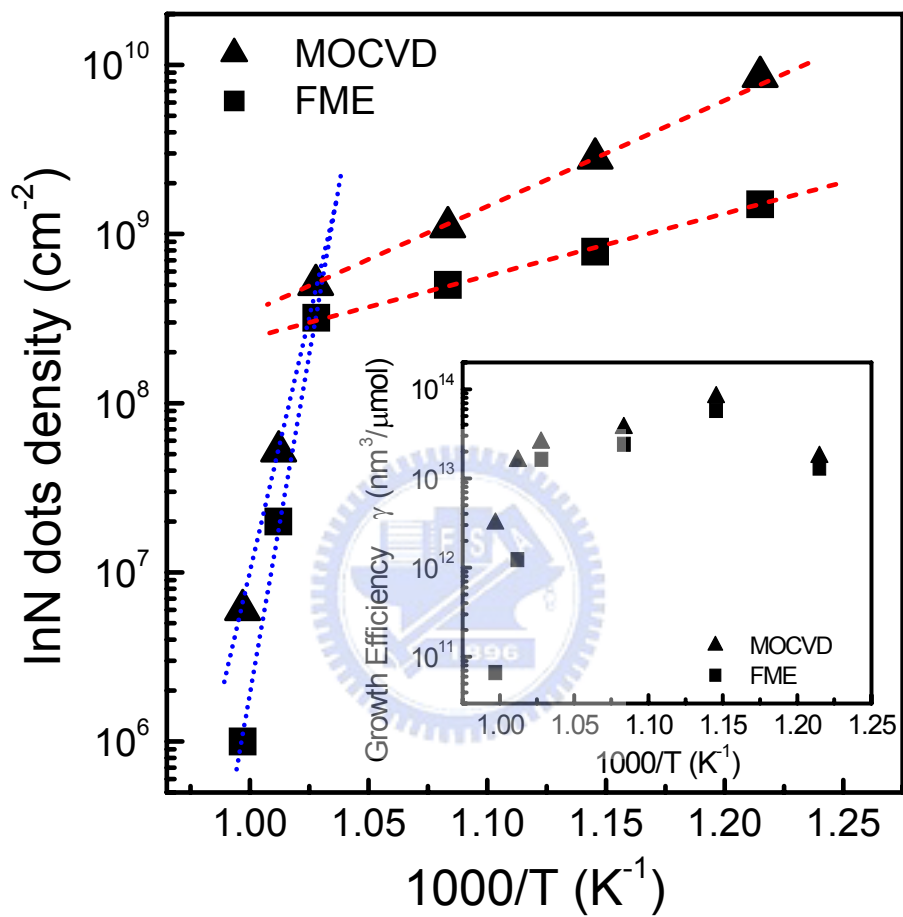


Fig. 7-2 The resulted Arrhenius plot of InN dots density as a function of reciprocal temperature. Insert shows the TMIn growth efficiency as a function of reciprocal temperature.

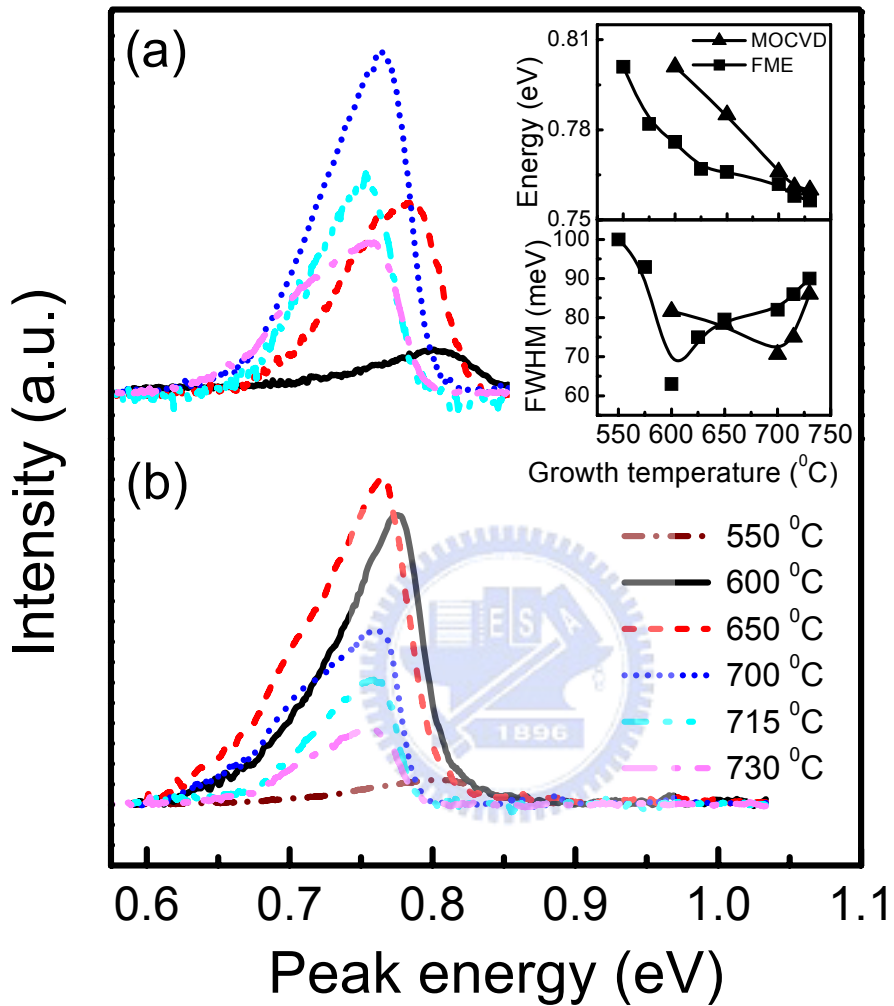


Fig. 7-3 The resulted 10-K PL spectra of InN dots grown by (a) MOCVD and (b) FME from 550 to 730°C, respectively, the peak energy and FWHM as functions of growth temperature were also presented in the insert.

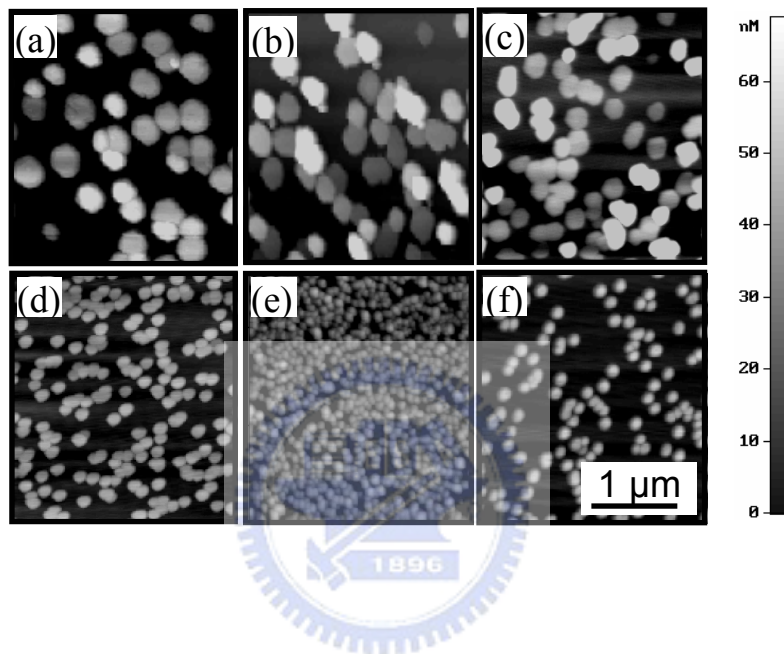


Fig. 7-4 The AFM images of InN dots at different NH₃ background flows varied from (a)0, (b)500, (c)1000, (d)5000 and (e)10000 sccm, respectively and (e) shows the AFM image of InN dots grown by MOCVD.

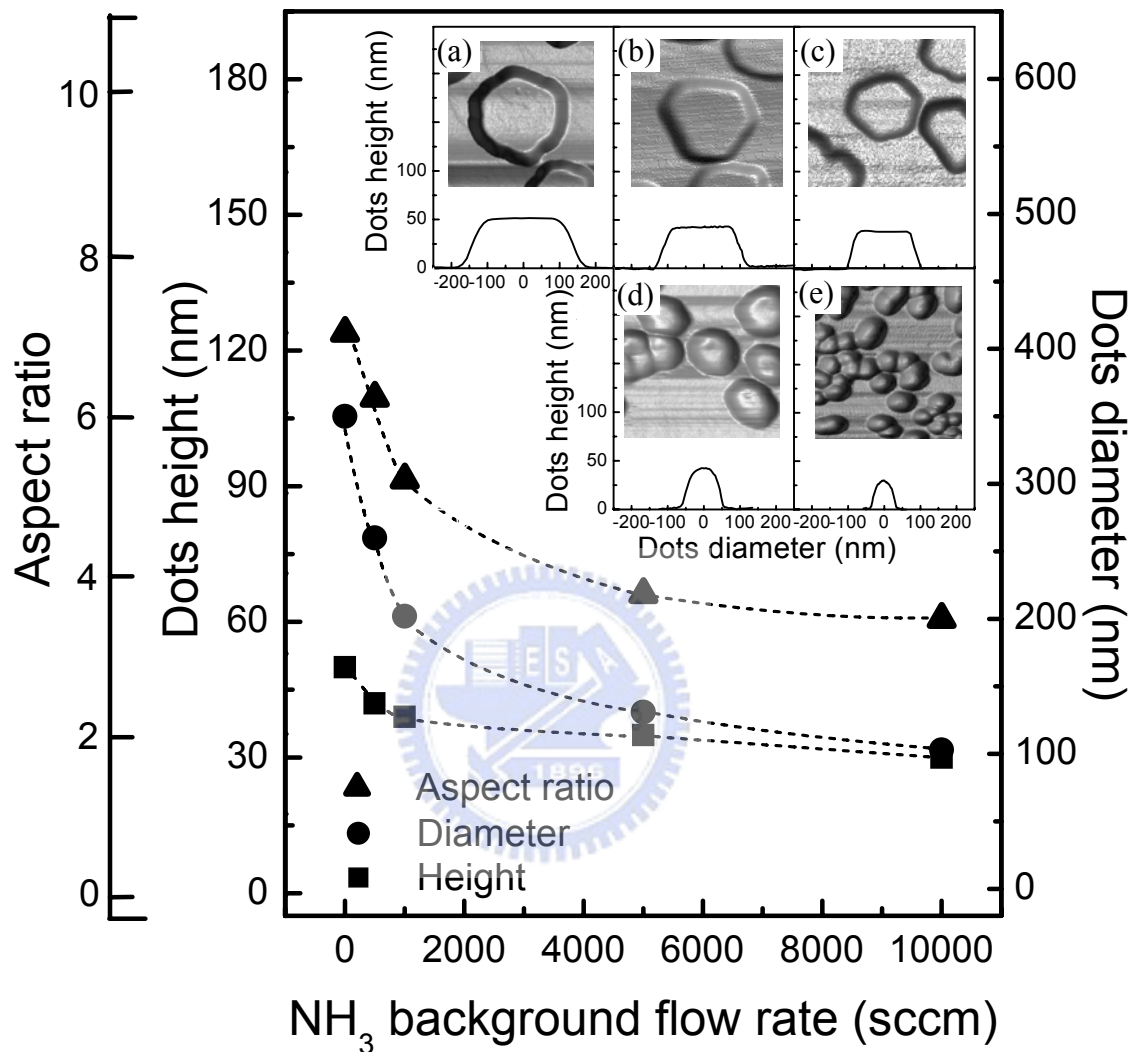


Fig. 7-5 The average dot height, diameter and aspect ratio as functions of the NH₃ background flux. The typical line profiles and AFM images of single individual InN dots grown at (a)0, (b)500, (c)1000, (d)5000 and (e)10000 sccm, respectively are presented in the inset.

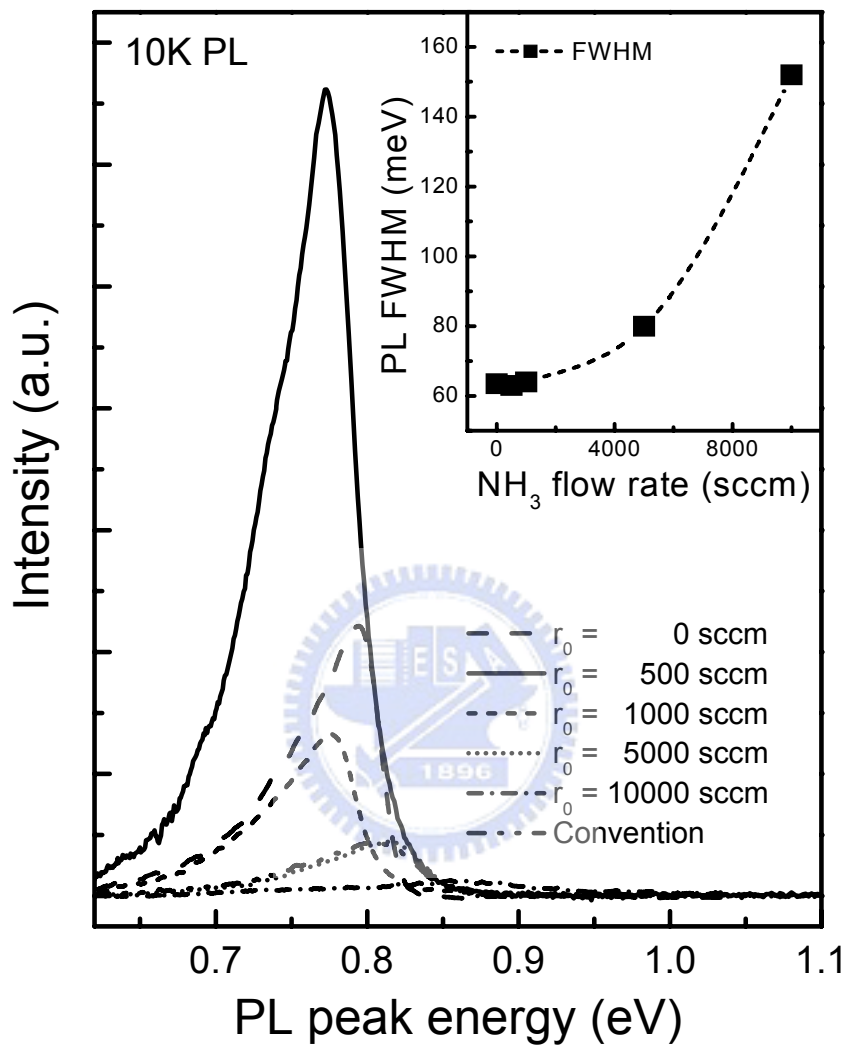


Fig. 7-6 The 10-K PL spectra of the InN dots grown by FME under different NH₃ background flux and by MOCVD.

Chapter 8 Conclusions

We have measured the optical properties of hillocks in $\text{Al}_{0.11}\text{Ga}_{0.89}\text{N}$ film by using the μ -PL microscopy. The large intensity and narrow FWHM of I_{H} in the hillock structure indicated that it is a strong emission center. The temperature dependent μ -PL spectra showed that the I_{H} has the S-shape behavior with a transition temperature of 120 K reflecting the strong localization in the hillock. The lower transition temperature and smaller red-shift of I_{H} than that of I_{matrix} suggest that the Al composition is lower in hillock than in other parts of AlGaN film. Moreover, by increasing the hillock diameter from 6 μm to 11 μm , the red shift is from 88 meV to 116 meV. It was indicated that the Al composition decreases progressively while the hillock size increase. The Al composition variation is about $\sim 2\%$.

For the GaN nanodots, we have demonstrated that the GaN dots can be grown on a slightly lattice-mismatched $\text{Al}_{0.11}\text{Ga}_{0.89}\text{N}$ epilayer using flow-rate modulated epitaxy. The dot growth in this method is found to be controlled primarily by surface diffusion of adatoms at substrate temperatures below $\sim 915^\circ\text{C}$ and by desorption at higher temperatures. Because of the alternating gas supply nature in FME, we consider that the dot growth studied here is mainly via the Volmer-Weber growth mode, not through the Stranski-Kranstanow growth mode. Our results indicate that the FME growth technique is a very promising tool for preparing self-organized quantum dot structures for most practical devices due to the release of requirement of large lattice mismatch between the grown dot structure and substrate.

Otherwise, we have shown that GaN QDs can be self-assembled on smooth surface of $\text{Al}_{0.11}\text{Ga}_{0.89}\text{N}$ films by FME. The AFM measurements showed the SK growth mode with a WL thickness of 7.2 MLs.

The localization energy was found to increase with the increasing dot size. The localization energies for the 8.5 nm, 7 nm, and 6.5 nm GaN dots are 28, 19, and 6 meV, respectively. Moreover, the thermal activation energies (E_a) are 43 ± 4 , 70 ± 13 , and 106 ± 13 meV for the 6.5/190, 7.0/200, and 8.5/220 nm dots, respectively. The activation energy increases with the increasing dot size. We believed that the charge carriers likely escape from the confined QD state to the nitrogen vacancy (V_N) state of $Al_{0.11}Ga_{0.89}N$ barrier for $T > 100K$. The nitrogen vacancy (V_N) state of $Al_{0.11}Ga_{0.89}N$ provides a carrier escape channel for quenching the PL intensity.

The self-assembly InN nano-dots were firstly successful grown on GaN films by pulsed growth mode technique. The derived values of adatom diffusion energy E_d and adsorption energy E_a from the dot density curves are 2.65 and 6.84 eV for pulsed mode technique and 1.25 and 12.3 eV for MOCVD, respectively. Comparing to MOCVD, the InN dot growth by pulsed mode technique appears to possess much higher diffusion activation energy, almost half of its opponent, and lower adatom adsorption energy. We have investigated the PL properties of InN dots embedded in GaN. Size-tunable emission energy was observed and was explained by the quantization effect in our InN dot samples. Temperature-dependent PL measurements showed that the PL peak energies of the dots are less sensitive to temperature, as comparing with that of bulk film, indicating the localization of carriers in the dots. A reduced quenching of the PL from the dots was also observed, implying superior emission properties for our embedded InN dots.

Finally, comparisons between InN dots grown by flow-rate modulation epitaxy (FME) and by MOCVD have been comprehensively performed in terms of the optical and morphological structure properties. In comparison with MOCVD, the FME InN dots growth in the temperature range of 550-700°C appears to have lower adatom

diffusion activation energy (0.7 vs. 1.3 eV) and lower dot density, which gives rise to better optical quality InN dot samples in this region, owing to the enhanced adatom migration mobility in such type of deposition scheme. More interesting results were observed for FME InN dot samples grown with different NH_3 background flows. The samples prepared under low NH_3 backgrounds (<1,000 sccm), hence In-rich growth conditions, generally exhibit narrower and more intense photoluminescence signals than ones prepared under N-rich conditions (>1,000 sccm). For instance, the PL intensity of InN dots grown under a NH_3 background flow of 500 sccm is increased by nearly a factor of 50 as compared to that under a NH_3 background flow of 10,000 sccm, where the growth is conducted in the regime of N-rich condition.



發表著作 (Publications)

(A) 期刊論文 (Referred papers):

- [1] W. C. Ke, C. P. Fu, C. Y. Chen, L. Lee, C. S. Ku, W. C. Chou, W.-H. Chang, M. C. Lee, W. K. Chen, W. J. Lin and Y. C. Cheng, 2006, '*Photoluminescence properties of self-assembled InN dots embedded in GaN grown by metal organic vapor phase epitaxy*', Appl. Phys. Lett. 88, 191913. [May 29, 2006 issue of Virtual Journal of Nanoscale Science & Technology]
- [2] W. C. Ke, C. P. Fu, C. C. Huang, C. S. Ku, L. Lee, C. Y. Chen, W. C. Tsai, W. K. Chen, M. C. Lee, W. C. Chou, W. J. Lin and Y. C. Cheng, 2006, '*Optical properties and carrier dynamics of self-assembled GaN/Al_{0.11}Ga_{0.89}N quantum dots*', Nanotechnology 17, 2609.
- [3] W. C. Ke, C. S. Ku, H. Y. Huang, W. C. Chen, L. Lee, W. K. Chen, W. C. Chou, W. H. Chen, M. C. Lee, W. J. Lin and Y. C. Cheng, 2004, '*Microphotoluminescence spectra of hillocks in Al_{0.11}Ga_{0.89}N films*', Appl. Phys. Lett. 85, 3047.
- [4] C. S. Ku, J. M. Peng, W. C. Ke, H. Y. Huang, N. E. Tang, W. K. Chen, W. H. Chen, and M. C. Lee, 2004, 'Near-field optical microscopy and scanning of V-defects on AlGaN/GaN films', Appl. Phys. Lett. 85, 2818.
- [5] W. C. Ke, H. Y. Huang, C. S. Ku, K. H. Yen, L. Lee, W. K. Chen, W. C. Chou, M. C. Lee, W. H. Chen, W. J. Lin, Y. C. Cheng and Y. T. Cherng, 2004, '*Formation of Self-organized GaN Dots on AlGaN by Alternating Supply of Source Precursors*', Jpn. J. Appl. Phys. 43, L 780.
- [6] H. Y. Huang, C. S. Ku, W. C. Ke, N. E. Tang, J. M. Peng, W. K. Chen, W. H. Chen, and M. C. Lee. 2004, '*Spatially-resolved photoluminescence studies of V-shaped pits on Al_{0.16}Ga_{0.84}N*', J. Appl. Phys. 95, 2172.
- [7] B. R. Huang, W. C. Ke, W. K. Chen, 2001, '*Electrical properties of the free-standing diamond films at high voltages*', Jpn. J. Appl. Phys. 40, 3240.

(B) 研討會論文 (Conference paper):

- [1] W. C. Ke, I. C. Chen, L. Lee, M. C. Lee, W. H. Chen, and W. K. Chen, '*Electrical characterization of strained-layer superlattices effects in AlGa_xN films grown by metalorganic vapor phase epitaxy*', Annual Meeting of the Optics and Photonics of R. O. C. Dec. 13-14 2001, Kaohsiung.
- [2] W. C. Ke, C. Lo, B. -R. Huang, I. C. Chen, W. J. Lin, W. H. Lan, Y. T. Cherng, M. C. Lee, W. H. Chen, and W. K. Chen, '*The characterization of epitaxial Al_xGa_{1-x}N alloys grown by metalorganic vapor phase epitaxy*', Annual Meeting of the Physics Society of R. O. C. Feb. 4-6, 2002, Taichung.
- [3] W. C. Ke, I. C. Chen, M. C. Lee, W. H. Chen, W. K. Chen, W. J. Lin, W. H. Lan, Y. T. Cheng, and B. R. Huang, '*Effects of ALM interlayers growth temperature on the properties of Al_xGa_{1-x}N films*', Annual Meeting of the Optics and Photonics of R. O. C. Dec. 12-13 2002, Taipei.
- [4] W. C. Ke, I. C. Chen, M. C. Lee, W. H. Chen, W. K. Chen, B. R. Huang, W. J. Lin, Y. C. Cheng, Y. T. Cheng, '*Study of AlN interlayer growth temperature on the characteristics of AlGa_xN films*', Annual Meeting of the Physics Society of R. O. C. Feb. 12-14, 2003, Hualien.
- [5] W. C. Ke, C. S. Ku, N. Lee, H. Y. Huang, W. K. Chen, W. C. Chou, M. C. Lee, W. H. Chen, W. J. Lin, Y. C. Cheng and Y. T. Cherng, '*Self-assembling GaN dots on Al_{0.11}Ga_{0.89}N by alternating supply of source precursors*', ICMOVPE-XII, May 30-June 4, 2004, Lahaina, Maui, Hawaii

(C) 專利 (Patterns):

- [1] 製作自行聚合奈米粒之方法 / PROCESS FOR MANUFACTURING SELF-ASSEMBLED NANOPARTICLES, 中華民國專利(I237391)及美國專利申請中。
- [2] 多波長發光元件之奈米粒結構及其製法 / Nanoparticle structure and manufacturing process of multi-wavelength light emitting devices, 中華民國專利及美國專利申請中。